eXPRESS Polymer Letters Vol.8, No.8 (2014) 543
Available online at www.expresspolymlett.com
DOI: 10.3144/expresspolymlett.2014.57

Editorial corner – a personal view
Biomimetic materials: A challenge for nano-scale self-assembly

*R. A. Shanks**

School of Applied Sciences, RMIT University, GPO Box 2476V, Melbourne, 3001, Australia

Structural and performance efficiency is evident throughout nature. Natural materials are a basis for materials design; because they have evolved creating properties that suit particular or diverse environments. Replicating natural materials is a strategy for designing optimally performing materials. There are several routes to biomimicry: 1) use biomaterials: minerals, wood and natural fibres directly in composites, 2) adapt natural processes: layer-by-layer formation, orientation and self-assembly to synthetic materials, 3) form synthetic or semi-synthetic structures that replicate natural morphologies. A further dimension is scale. Preparation of biomimetic materials has trended towards nano-scale where components, morphology and techniques are combined. Nano-dimensions provide large interfaces and structural perfection. Articles in eXPRESS Polymer Letters present developments in biomimetic polymer materials that attract much interest.

Material design, processing and component selection are requirements of characterisation techniques, with sensitivity and resolution at the nano-scale. X-ray scattering and transmission electron microscopy are theoretically suited. Surface force microscopy is a collection of techniques with growing specificity. The diffraction limitation of optical microscopy is circumvented with fluorescent nano-imaging adaptions. Infrared and Raman microscopy are emerging with nano-scale variants. Computation and interpretation of data form standard structure–property techniques provide indirect or inferred information about nano-materials.

Most natural structural materials are composites, since component properties are retained, not averaged, and incongruous properties: hardness, toughness and strength are achieved simultaneously. Nacre is tough, hard and strong, yet it contains mainly calcium carbonate with minimal organic binder. Multiphase composites that contain platelets or fibrous inclusions focus anisotropic performance, with orientation imposed by processing or self-association. Natural materials are often not space-filling; they contain voids interspersed with structural regularity, commonly hexagonal features. Some voids are channels to convey nutrients to the living system. Synthetic analogies are foams and membranes. Foams decrease density more than mechanical properties, while membranes are functional materials. Foam, honeycomb and cantilevered structures are prepared, though they present most challenge at the nano-scale. Finite element modelling predicts that uniform strength is unnecessary; stress must be effectively transferred from regions of stress concentration.

Biomimetic concepts have expanded to self-repair, typically containing reagent microcapsules or reversible reaction functionality. A living system with channels to convey repairing substances is an analogy, though in a renewable material a complexity is removal of damaged materials from repair sites to allow continued renewal. Can micro or nano bricks and mortar structures be prepared and controlled though self-assembly, including self-repair?

Prof. Dr. Robert A. Shanks
Member of International Advisory Board

*Corresponding author, e-mail: robert.shanks@rmit.edu.au

eXPRESS Polymer Letters Vol.8, No.8 (2014) 544–553
Available online at www.expresspolymlett.com
DOI: 10.3144/expresspolymlett.2014.58

Chemical recycling of poly(ethylene terephthalate). Application to the synthesis of mutiblock copolyesters

A. El Mejjatti[1], T. Harit[1], A. Riahi[2], R. Khiari[3], I. Bouabdallah[1], F. Malek[1]*

[1]Laboratoire de Chimie Organique, Macromoléculaire et Produits Naturels – URAC 25 Faculté des Sciences – Université Mohamed Premier. Bd Mohamed VI, BP : 717 – 60 000 Oujda – Maroc
[2]Université de Reims Champagne-Ardenne, Institut de Chimie Moléculaire de Reims (ICMR)- Groupe Méthodologie en Synthèse Organique, CNRS UMR 6229, Bat. Europol'Agro-Moulin de la Housse, BP 1039, 51687 Reims Cedex 2, France
[3]Laboratoire de Chimie Appliquée et Environnement, Faculté des Sciences – Université de Monastir, 5000 Tunisie

Received 29 January 2014; accepted in revised form 2 April 2014

Abstract. The chemical recycling of the poly(ethylene terephthalate), (PET), has been successfully carried out by glycolysis in the presence of bis (2-hydroxyethyl) terephthalate (BHET) resulting in the formation of hydroxytelechelic oligomers. These oligomers were then treated with carboxytelechelic poly(ε-caprolactone) oligomers of $\overline{M}_n$ = 2300 and $\overline{M}_n$ = 730 g·mol^{-1} molecular weight, in the absence or presence of the titanium tetrabutyloxide ($Ti(OBu)_4$) as a catalyst to get multiblock copolyesters. The chemical structure of the synthesized copolyesters was investigated by size exclusion chromatography (SEC) and proton Nuclear Magnetic Resonance (^{1}H NMR) spectroscopy. Moreover the differential scanning calorimetry (DSC) was used to explore their thermal properties. The ester-ester interchange reaction was observed between the two oligopolyesters, was studied and discussed in detail.

Keywords: *recycling, poly(ethylene terephthalate), polyesterification, thermal analysis*

1. Introduction

Poly(ethylene terephthalate), (PET), is a thermoplastic semi-crystalline polyester with excellent tensile and impact strength, chemical resistance, clarity, process ability, transparency, and appropriate thermal stability [1]. It is mainly used in the textile industry, to manufacture of video and audio tapes, X-ray films, food packaging, water and soft-drink bottles. The global consumption of PET packaging was almost 15.5 Mt in 2009, while it is expected to reach 19.1 Mt by 2017, a 5.2% increase per annum [2, 3]. The increased consumption of PET is creating serious environmental problems as vast waste stream reaches every year due to short life duration of PET etc. Disposing of the waste to the landfill is becoming undesirable due to legislation pressures, rising costs and the poor biodegradability of such polymers. Therefore, other ways of PET waste treatment, such as recycling is highly desired.

Polymer wastes can be recycled in many ways for example, the energetic valorization which consists of using energy emanating from PET burning. Another method called mechanical recycling where the polymers are transformed into other objects after a step in the molten state. The recycled PET is used in different applications which do not require very high quality standards [4, 5]. Among all polymer recycling methods, chemical method has attracted more attention due to sustainable development principles. This method is very useful for the condensation of polymers, such as polyamides, polyurethanes and polyesters, which are vulnerable to solvolytic chain

*Corresponding author, e-mail: fouad_malek@yahoo.fr

cleavage. The key advantage of this method includes the huge availability of the different chemical products which can be obtained with different reagents [6–9].

Recently, several processes such as alcoholysis, aminolysis, hydrolysis, and glycolysis have been used for PET chemical recycling. Glycolysis reaction is more interesting, and can be described as a molecular depolymerisation by transesterification between PET ester groups and a diol. The ester linkages are therefore broken and replaced with hydroxyl terminals. The monomers or higher oligomers obtained can be used as building blocks to synthesize other polymers with higher economical values. For example, saturated and unsaturated polyesters [10–12], polyurethanes [13–15], coating materials [16–19] and additives [20–22] have been synthesized from such building blocks in recent years.

A large number of reagents have been used for glycolysis of PET such as ethylene glycol [23–26], diethylene glycol [27, 28], propylene glycol [29], neopentyl glycol [14], 1,4-butanediol [30, 31], and some synthetic oligoesters [32, 33]. To the best of our knowledge, no one has ever been used BHET as diol for the PET glycolysis. Similarly, several studies have been carried out on the reaction of PET and ethylene glycol for the synthesis of hydroxytelechelic oligomers of PET [34–36] which were mainly used for producing unsatured polyester resins [34, 35] and very few polycondensations have been carried out by using hydroxytelechelic oligomers of PET with ε-caprolactone [37]. Copolyesters with PET and ε-caprolactone units are mainly synthesized by polycondensation of dimethyl terephthalate, ethylene glycol and ε-caprolactone [38], or by transesterification in copolyester blend [39, 40].

In this context, in order to explore a new method for PET recycling herein, the glycolysis of the PET performed with its structural units BHET was reported. This paper presents a continuous reactive extrusion process and evaluates the potentiality of the polyesterification of hydroxytelechelic oligomers resulting from the glycolysis of PET with the carboxytelechelic PCL oligomers as a new method for valorization of PET wastes. All the obtained products are investigated by proton nuclear magnetic resonance spectroscopy (^{1}H NMR), size exclusion chromatography (SEC) and differential scanning calorimetry (DSC).

2. Experimental part

2.1. Reagents

Poly(ethylene terephtalate) (PET) ($\overline{M}_n$ = 26 000 g·mol^{-1}), bis(2-hydroxyethyl) terephthalate (BHET), poly(ε-caprolactone) diol (PCL) ($\overline{M}_n$ = 530 and 2000 g·mol^{-1}), zinc acetate (Ac_2Zn), and titanium tetrabutyl oxide (Ti(OBu)4), are obtained from Sigma-Aldrich (St Quentin Fallavier, France). All other chemicals (solvents and reagents) were used of analytical grade and were obtained from Somaprol (Casablanca, Morocco).

2.2. Glycolysis of PET by BHET

PET pellets (20.03 g; 0.104 mol (PET monomer unit)), BHET (26.50 g; 0.208 mol of hydroxyl equivalent), and 0.20 g of zinc acetate (Ac_2Zn) were put into a 500 mL reactor equipped with a mechanic stirrer, a nitrogen inlet and a vacuum outlet. The reactor was heated under nitrogen at 250°C for 2 h. After the die, the modified PET crystallized in bulk and it is grinded into powder, and the residual BHET is removed by precipitation in hot water. The white product was dried under a vacuum at 80°C for 48 h. The powder was obtained in an 85% yield and characterized by ^{1}H NMR spectroscopy with trifluoroacetic acid (TFA) and Deuterated chloroform ($CDCl_3$) as the solvent.

^{1}H NMR: δ (ppm): 8.10 (aromatic protons) 4.70 ($C\underline{H}_2$ between two esters functions); 4.55 ($C\underline{H}_2CH_2OH$); 4,15 ($C\underline{H}_2OH$).

2.3. Synthesis of carboxytelechelic poly(ε-caprolactone) oligomers

The carboxytelechelic poly(ε-caprolactone) oligomers of molecular weight $\overline{M}_n$ = 2300 g·mol^{-1} and $\overline{M}_n$ = 730 g·mol^{-1} are prepared from hydroxytelechelic oligomers of molecular weight 2000 and 530 g·mol^{-1} respectively, according to the procedure described in the literature [41].

In a 500 mL two-necked flask equipped with a condenser, a nitrogen inlet and a magnetic stirrer, 20 g (0.01 mol) of PCL, 2.2 g (0.022 mol) of succinic anhydride and 1 mol % of DMAP with 200 mL of 1,4-dioxan solvent were introduced. The reaction has occurred at 50°C. After 10 hours of reaction, the solvent was removed by evaporation under vacuum at 100°C and the residual product was solubilized in chloroform. The reaction mixture was washed with acidic water (pH = 1) in order to remove residual suc-

cinic acid. After drying on Na_2SO_4, the solvent was removed by evaporation and under vacuum at 60°C. The mass yield of the reaction was 80%. The products are characterized by pH titration of carboxylic functions, ^{1}H NMR spectroscopy and SEC.

The titration of carboxylic functions of the products (of the addition of succinic acid onto hydroxyl function) is carried out by following a classic method: a known mass of the product is titrated by a solution of KOH in methanol (MeOH) solvent with tetrahydrofuran (THF) as solvent and phenolphthalein as color indicator. The carboxyl ratio is given by the Equation (1):

$$I_{COOH} = \frac{C_{KOH} \cdot V_{KOH}}{m} \quad (1)$$

where C_{KOH} represents the concentration of KOH solution, V_{KOH} is the equivalent volume and m is the mass of oligomer titrated. These tests were performed at least in duplicate, and the difference between the various obtained values was within the experimental error of 5%.

^{1}H NMR: δ (ppm): 8.4 (acid proton); 4.1 (CH_2 between two ester functions, one linked to caprolactone unit (in α) and one linked to succinic unit (in β)); 4.0 (CH_2 of caprolactone unit in α of ester function); 3.6 (CH_2 between two ester functions, one linked to caprolactone unit (in β) and another linked to succinic unit (in α)); 2.6 (CH_2 between an ester and a carboxylic function); 2.3 (CH_2 in α of a carboxyl group and methylenic carbon); 1.1–1.7 (Internal CH_2 of caprolactone unit).

2.4. Copolyesterification of hydroxytelechelic PET oligomers and carboxytelechelic poly(ε-caprolactone) oligomers

The reaction of copolyesterification of carboxytelechelic oligomers with hydroxytelechelic oligomers of PET is performed in a bulk, in a four-necked flask, with a condenser, a nitrogen inlet, a mechanical stirrer and a high vacuum inlet.

The hydroxytelechelic PET oligomers, the carboxytelechelic poly(ε-caprolactone) oligomers ($\overline{M}_n$ = 730 or 2300 g·mol^{-1}) and 1 wt% of catalyst ($Ti(OBu)_4$) (or without catalyst) are introduced and the reaction mixer is heated at 240°C under nitrogen until the complete fusion of oligomers of PET. After, the pressure is led to 10^{-1} mbar in the reactor and the reaction temperature is kept constant at 240°C. The copolyesters are obtained with yield ranging from 85 to 90%. Subsequently the products are characterized by SEC, ^{1}H NMR as well by DSC.

^{1}H NMR: δ (ppm) 8.1 (aromatic protons); 4.2 (CH_2 between two ester functions, one linked to caprolactone unit (in α) and another linked to succinic unit (in β)); 4.0 (CH_2 of caprolactone unit in α of ester function); 3.6 (CH_2 between two ester functions, one linked to caprolactone unit (in β) and one linked to succinic unit (in α)); 2.65 (CH_2 between an ester and a carboxylic function); 2.3 (CH_2 in α of a carboxyl group and methylenic carbon) ; 1.0–1.7 (internal CH_2 of caprolactone unit).

2.5. Apparatus

2.5.1. Nuclear magnetic resonance (NMR)

The ^{1}H NMR spectra are recorded on a Bruker spectrometer 250 MHz at room temperature. The solvent used for oligomers of PET is $CDCl_3$/TFA (20:1). The solvent for the other products is $CDCl_3$. Chemical shifts are given in ppm relative to Tetramethylsilane as an internal reference.

2.5.2. Size exclusion chromatography (SEC)

The size exclusion chromatograms are recorded on an IOTA2 apparatus supplied by JASCO with a PU-980 Intelligent HPLC pump. The columns employed were PLgel 5 μm Mixed-D 300×7.5 mm, VARIAN INC. The molecular weights of poly(ε-caprolactone) oligomers and of copolyesters are measured respectively with THF or chloroform/ hexafluoropropan-2-ol ($CHCl_3$/HFIP) (98/2 wt) as solvent at a flow rate of 1 mL·min^{-1}. Samples are injected using an injector of the Agilent 100 Series. The calibration curves are obtained from polystyrene (PS) standards. These tests were performed at least in duplicate, and the difference between the various obtained values was within the experimental error of 5%.

2.5.3. Differential scanning calorimetry (DSC)

DSC analyses were performed with a 204 F1 NETZSCH. Experiments are carried out under nitrogen with samples ranging from 7 to 15 mg. The temperature was calibrated with ultra-pure indium, octane and dodecyloctane. The temperature range of the first heating scan was between –80 to 280°C, with a heating rate of 10 K·min^{-1}, followed by a cooling at 20 K·min^{-1}. A second scan was immediately performed with a heating rate of 10 K·min^{-1}. Glass tran-

sition temperature was taken at the midpoint of change in heat capacity. These measurements were performed at least in duplicate.

3. Results and discussion

3.1. Synthesis of PET oligomers

The synthesis of hydroxytelechelic oligomers of PET was performed by glycolysis of PET with its monomer BHET using zinc acetate (Ac_2Zn) as the catalyst. This reaction of depolymerization is described in Figure 1.

As described in several previous studies [32, 35, 36] the PET glycolysis products are α, ω-hydroxyl oligomers. Indeed, different SEC analysis, ^{1}H NMR spectroscopy, and matrix-assisted laser desorption ionization time-of-flight mass spectrometry was established; these studies show a good correlation in the determination of hydroxyl end groups and molecular weights below 4000 g·mol^{-1}.

The four peaks of the ^{1}H NMR spectrum as reported in Figure 2, correspond to the signals of PET oligomer protons. The average molecular weight of the oligomers is calculated from ^{1}H NMR spectroscopy using the integrations of the aromatic protons and the methylene protons adjacent to the hydroxyl end functions. The integration ratio of these signals allowed the calculation of the number of terephthalic base units in the oligomers through Equation (2):

$$m = \frac{I_{8.10\ \mathrm{ppm}}}{I_{4.15\ \mathrm{ppm}}} \tag{2}$$

where $I_{x\ \mathrm{ppm}}$ represents the integral value of the peak centered at x ppm.

So it is easy to determine the average molecular weight of the oligomers. The m value is about 100/14.7 = 6.8. The PET oligomer has an average molecular mass of 1360 g·mol^{-1}, with an average polymerization number ($\overline{DP_n}$) of 13.6.

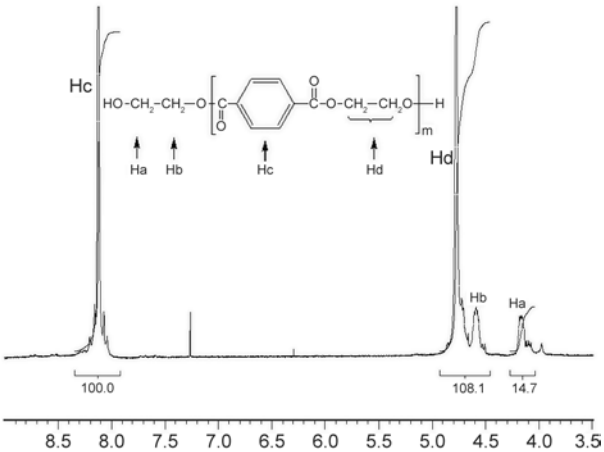

Figure 2. ^{1}H NMR spectrum of hydroxytelechelic oligomers of PET

In these conditions, the molar weight of the obtained glycosilation products were lower than the products reported in the literature (about 1450 g·mol^{-1} [35] and 1800 g·mol^{-1} [36]), these values were obtained during the PET glycolysis with the ethylene glycol, using dibutyl tin oxide as the catalyst.

The PET oligomer is soluble only in few solvents, for this reason, it is used in the molten state for further polyaddition. The differential scanning calorimetry (DSC) analysis gives the glass transition temperature (T_g = 78°C), melting point (T_m = 235°C) and crystallization temperature (T_c = 175°C) of the glycolysed PET oligomers.

The product has a melting temperature close to that of PET, but slightly lower. This is in good agreement with the literature data [5, 35], which shows that the melting temperature depends on and varies from 110 up to 220°C when $\overline{DP_n}$ varies from one to five. For $\overline{DP_n}$ above five, the melting temperature is very close to that of PET.

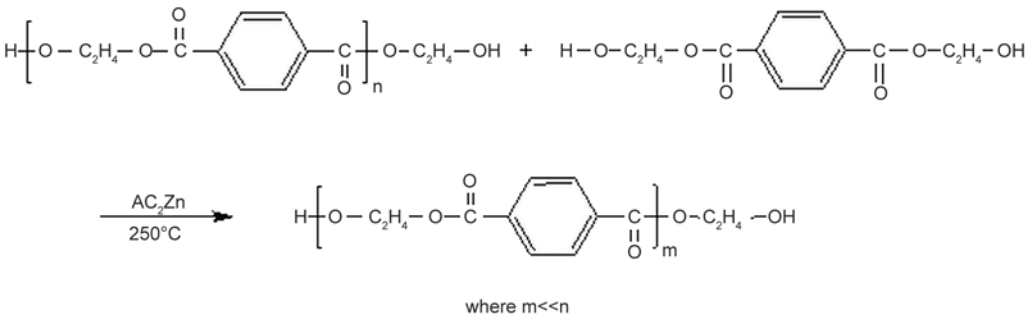

Figure 1. Depolymerization of PET by BHET

3.2. Synthesis of carboxytelechelic of poly(ε-caprolactone) oligomers

The carboxytelechelic PCL oligomers are not commercially available.Their synthesis was performed by reacting succinic anhydride with the hydroxyl functions of the commercial PCL oligomers using dimethylaminopyridine (DMAP) as a catalyst, as shown in Figure 3.

The synthesis and characterization of the carboxytelechelic poly(ε-caprolactone) oligomers of molecular weight $\overline{M}_n$ = 2300 g·mol^{-1} and $\overline{M}_n$ = 730 g·mol^{-1} from hydroxytelechelic oligomers of molecular weight 2000 and 530 g·mol^{-1} respectively [41] has been described. The structure of these oligomers is confirmed by ^{1}H NMR, pH titration of carboxylic functions and size exclusion chromatography. In their ^{1}H NMR spectra, it can be noticed that the presence of a broad signal at 8.4 ppm corresponding to the acid proton. The α- and β-protons of the acid function appears as a multiplet centred at 2.6 ppm. Other peaks correspond to the protons of the aliphatic chain of PCL. The peak integration ratios of different signals confirmed clearly the esterification reaction between the succinic anhydride and the PCL diol. The titration of the carboxyl functions allowed us the calculation of the carboxylic functionality of PCL, which has been determined to be 1.98 in both cases, as described in the experimental part.

3.3. Synthesis and characterization of copolyesters

The copolyesterification of hydroxytelechelic PET oligomers and carboxytelechelic PCL oligomers was performed in the molten state, under vacuum (10^{-1} mbar) and high temperature so as to get rid of water formed, to shift the esterification equilibrium. The reaction is performed at 240°C because of the high melting point of PET oligomers, using $Ti(OBu)_4$ as a catalyst, as shown in Figure 4.

As reported in the literature, the $Ti(OBu)_4$ is more reactive when being used at a reaction temperature of 240°C and enhances somewhat the $\overline{M}_n$ obtained [42]. For titanium catalytic system, studied by Fradet and Marechal [43], the acid function coordinates with Ti, and some experiments of Fradet and Marechal show that the system follows thermodynamic laws. Indeed, the rate constant of the reaction increases with increasing of the temperature. Other works enlighten the same phenomenon and give further explanations onto titanium alkoxide activity for esterification or transesterification reactions [42, 44].

To study the influence of the molecular weight of PCL carboxytelechelic on the properties of co-polyesters, the polyesterification reactions were established with the PCL oligomers of $\overline{M}_n$ = 2300 g·mol^{-1} and $\overline{M}_n$ = 730 g·mol^{-1}. In the same way, in order to evaluate the influence of the catalyst on these prop-

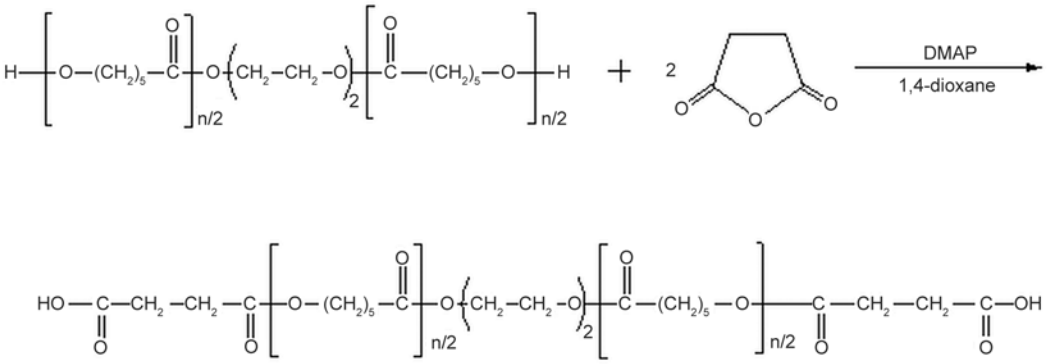

Figure 3. Synthesis of carboxytelechelic PCL oligomers

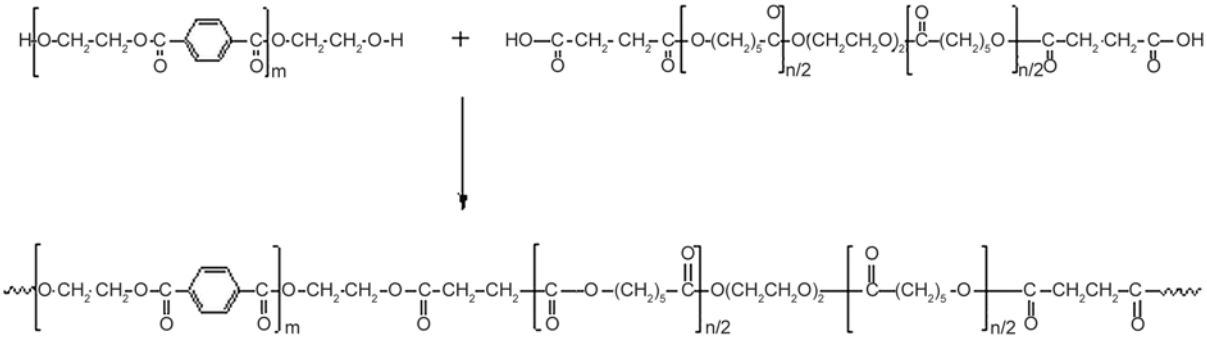

Figure 4. Copolyesterification of hydroxytelechelic PET oligomers and carboxytelechelic PCL oligomers

Table 1. Properties of products of copolyesterification

Copolyester	PET [g]	PCL [g]	$Ti(OBu)_4$ [wt%]	$\overline{M}_n$ [g·mol^{-1}][c]	$\overline{M}_w$ [g·mol^{-1}][c]	I_p[c]	T_g[d] [°C]	T_m[d] [°C]	Ester-ester reaction [%][e]
1	25	40[a]	1	21 000	38 800	1.85	–20	–	35
2	25	13[b]	1	22 500	38 200	1.70	–10	200	15
3	25	13[b]	0	19 500	37 000	1.90	–6	208	8

[a]Experiments led by using carboxytelechelic poly(ε-caprolactone) oligomers with molecular weight of 2300 g·mol^{-1}.
[b] Experiments led by using carboxytelechelic poly(ε-caprolactone) oligomers of molecular weight of 730 g·mol^{-1}.
[c]Determined by size exclusion chromatography in $CHCl_3$/HFIP (98/2 wt) with monodisperse PS standards
[d]Determined by DSC at 20°C·min^{-1}.
[e]Determined by ^{1}H NMR spectroscopy.

erties, an uncatalyzed reaction with the oligomers of $\overline{M}_n$ = 730 g·mol^{-1} was accomplished. All the characterization results of the obtained copolyesters are reported in Table 1.

The molecular weights of the obtained copolyesters are comprised between 19 500 and 22 500 g·mol^{-1} and the polydispersity index is close to 2. This value is characteristic for the polycondensation reactions. The molecular weight of the copolyester **1** is lower than the copolyester **2**. This can be easily explained by the lower reactivity of terminal carboxylic functions of the high molecular weights oligomers as well as by the steric environment, which prevents hydroxyl functions of PET oligomers to reacting with the carboxylic functions. It can be also noticed that the uncatalyzed reaction gives molar mass polyester (copolyester **3**) slightly lower. The obtained result is in good agreement with the literature [42, 43].

The ^{1}H NMR spectrum of polyesterification products (Figure 5) showed the main conventional spectroscopic fingerprints of PET and PCL blocks, respectively, and the chemical linkage between the different blocks.

From the spectra, some signals coming from ester–ester interchange reaction between base monomers units are represented in Table 2. The ester-ester exchange reaction is a well-known phenomenon that occurs in a polyester chain [45–47]. This reaction comes from internal trans-esterification reactions, leading to inversion of monomers base units into the polyester chain. Their study focused on the

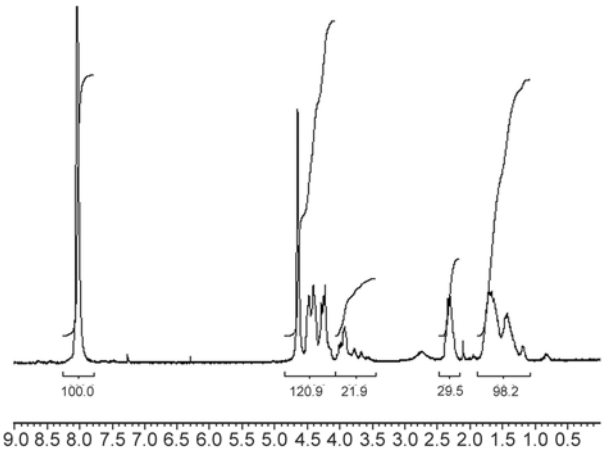

Figure 5. ^{1}H NMR spectroscopy of copolyesters

polymers blends, but not on a chemical reaction between PET oligomers and the PCL.

The ^{1}H NMR spectroscopy allows then the calculation of the percentage of ester–ester interchange reaction. This side reaction rate can be determined by using the value of the integration of the peaks at 4.6 and 8.0 ppm (named respectively, $I_{4.6}$ and $I_{8.0}$). If the trans-esterification reaction had not occurred, the ratio I4.6/I8 would not have been modified between the spectrum of oligomers of PET and the copolyesters. The percentage of transesterification phenomenon can be easily determined when comparing the ratio of the integration of the signals at 8 and 4.6 ppm of the PET precursor oligomers and the one of the copolyester. As a result the percentage of transesterification is given by the Equation (3):

$$\%\,\text{transesterification} = \left[1 - \frac{\left(\frac{I_{4.6\ \text{ppm}}}{I_{8.0\ \text{ppm}}}\right)\text{in copolyester}}{\left(\frac{I_{4.6\ \text{ppm}}}{I_{8.0\ \text{ppm}}}\right)\text{in PET oligomer}}\right] \tag{3}$$

Table 2. ^{1}H NMR study of transesterification products

Chemical shift [ppm]	Coming from	Chemical structure
4.50	Esterification	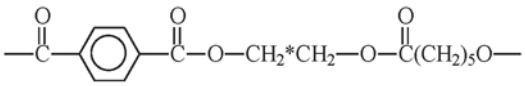
4.40	Esterification	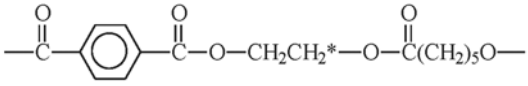
4.25	Transesterification	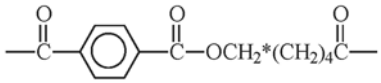
4.20	Transesterification	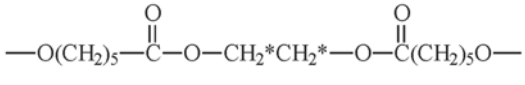

This percentage has been calculated for each experiment (Table 1) and a correlation between the ester–ester interchange reaction and the thermal behaviour of the copolyesters has been investigated.

When the copolyesters are synthesized from PCL of $\overline{M}_n$ = 730 g·mol^{-1}, the non-catalyzed reaction gave polyester with about 8% of transesterification reaction, and the ester-ester interchange reaction with titanium-catalyzed copolyester is quantified at about 15%. The results show a link between titanium and ester-ester interchange reaction. It can be a remark also, that the exchange percentage of ester-ester is higher for the copolyester **1** (35%). This is probably due to the low reactivity of PCL used with higher molecular weight. Therefore, the low amount of ester–ester interchange reaction in the copolyester **2** is clear and it can be attributed to the utilization of PCL with low molecular weight.

The DSC thermogram shows that the copolyester **1** does not present a crystalline phase and has only one glass transition temperature (T_g), comprised between the T_g of the PET oligomers and the PCL. The intermediate T_g shows that this copolyester does not present phase segregation phenomenon. It can be explained by the ester-ester interchange reaction. This reaction prevents the copolyester from having thermoplastic elastomer behaviour because length of soft and hard segments decreases and phase segregation is then defavorized.

The immiscibility of PET and PCL was shown by Ma and Prud'homme [46]. However, in our case, the obtained DSC analysis showed that this polyester is constituted by only one phase. This can be linked to the secondary reaction, occurring during polyesterification, which leads to a homogenous mixture.

The use of the Fox-Flory law for blends of miscible polymers could be interesting in order to verify the miscibility of the two phases present in the copolyester **1**. If the glass transition temperature of the copolyester, determined by DSC analysis, is close to the calculated one, the hypothesis of non-phase segregation is confirmed. The Fox-Flory equation (Equation (4)) gives the theoretical value of glass transition temperature of –24°C for this copolyester:

$$\frac{1}{T_g} = \sum \frac{\omega_i}{T_{gi}} \tag{4}$$

where ω_i is the fraction weight of polymer i in the blend and T_{gi} the glass transition temperature of the polymer i.

The comparison between this value and the experimental value obtained by DSC analysis (Table 1) shows that this co-polyester approaches a mono phase compound behaviour. It can be linked with the ester-ester exchange reaction that produces random co-polyester in which phase segregation phenomenon cannot occur.

The co-polyesters **2** and **3** present only one glass transition temperature (about –6°C with non-catalyzed reaction and –10°C with titanium catalyzed reaction) and only one melting point (T_m) ranging between 200 and 208°C (Table 1). However no crystallization temperature (T_c) can be observed. These obtained co-polyesters are phase segregated. They present amorphous and crystalline phases. The T_g of each co-polyester was different if compared to the theoretical one, calculated using the Fox-Flory law, and which confirms the coexistence of crystalline and amorphous phases in these co-poly-

esters. Thus, it proves the immiscibility of the two phases. Therefore, it seems that when the ester-ester exchange reaction ratio is not high, the trans-esterification reactions do not prevent the co-polyester from being a segregated product.

The decreasing of the co-polyesters T_m shows also an evolution in the phase segregation. This phenomenon could be explained by the coexistence of a crystalline phase with a high content of PET and a low content of PCL, and an amorphous phase with a high content of PCL and a low amount of PET. The decreasing of PET amount in the crystalline phase can be explained by the loss of the crystallizing point. However T_m and T_c of the PCL have not been detected in the crystalline phase. This hypothesis is in accordance with the work of Ma and Prud'homme [46] which showed the immiscibility of PET and PCL.

4. Conclusions

In the present work, PET is depolymerized by its BHET monomer. Hydroxytelechelic oligomers were obtained in good yield with a molecular weight of $\overline{M}_n$ = 1360 g·mol^{-1}. The thermal properties of the obtained oligomers were found comparable to the properties of the starting PET.

Further, the synthesis of co-polyesters was achieved by polyesterification of the reactive α–ω, hydroxy oligomers of the PET and α–ω, carboxy PCL. The chemical structure of the synthesized co-polyesters was established by SEC and ^{1}H NMR spectroscopy. The comparison of the molecular weights of the obtained co-polyesters showed that the catalyst enhances the molecular weight of the obtained co-polyesters, and the use of carboxytelechelic PCL oligomers with high molecular weight ($\overline{M}_n$ = 2300 g·mol^{-1}) gives a co-polyester with a lower molecular weight. This may be due to the low reactivity of the terminal carboxylic functions.

Furthermore, the presence of the titanium catalyst improves both the polyesterification and the ester–ester exchange reaction. This phenomenon also affects the thermoplastic properties of the obtained co-polyesters. The phase segregation is limited at high ester-ester exchange reaction ratio. However, when the ester-ester exchange reaction ratio is not high, the trans-esterification reactions do not prevent the co-polyester from being a segregated product. The phase segregation permits, in this case, to obtain a thermoplastic elastomer compound. This may be achieved using oligomers carboxytelechelic PCL with a lower $\overline{M}_n$ (e.g. $\overline{M}_n$ = 730 g.mol-1).

Acknowledgements

The authors gratefully thank the CNRST (Morocco) and the program Morocco-Tunisian (project code: 13/MT/24) for their financial support of this work.

References

[1] Karayannidis G. P., Nikolaidis A. K., Sideridou I. D., Bikiaris D. N., Achilias D. S.: Chemical recycling of PET by glycolysis: Polymerization and characterization of the dimethacrylated glycolysate. Macromolecular Materials and Engineering, **291**, 1338–1347 (2006). DOI: 10.1002/mame.200600243

[2] Smithers Pira organization. The Future of Global PET Packaging to 2017. Pira International Market Report Organization (2012).

[3] Siddiqui M. N., Redhwi H. H., Achilias D. S.: Recycling of poly(ethylene terephthalate) waste through methanolic pyrolysis in a microwave reactor. Journal of Analytical and Applied Pyrolysis, **98**, 214–220 (2012). DOI: 10.1016/j.jaap.2012.09.007

[4] Navarro R., Ferràndiz S., López J, Seguí V. J.: The influence of polyethylene in the mechanical recycling of polyethylene terephtalate. Journal of Materials Processing Technology, **195**, 110–116 (2008). DOI: 10.1016/j.jmatprotec.2007.04.126

[5] Awaja F., Pavel D.: Recycling of PET. European Polymer Journal, **41**, 1453–1477 (2005). DOI: 10.1016/j.eurpolymj.2005.02.005

[6] Beneš H., Slabá J., Walterová Z., Rais D.: Recycling of waste poly(ethylene terephthalate) with castor oil using microwave heating. Polymer Degradation and Stability, **98**, 2232–2243 (2013). DOI: 10.1016/j.polymdegradstab.2013.08.019

[7] Tawfik M. E., Eskander S. B.: Chemical recycling of poly(ethylene terephthalate) waste using ethanolamine. Sorting of the end products. Polymer Degradation and Stability, **95**, 187–194 (2010). DOI: 10.1016/j.polymdegradstab.2009.11.026

[8] Güçlü G., Yalçınyuva T., Özgümüş S., Orbay M.: Simultaneous glycolysis and hydrolysis of polyethylene terephthalate and characterization of products by differential scanning calorimetry. Polymer, **44**, 7609–7616 (2003). DOI: 10.1016/j.polymer.2003.09.062

[9] Karayannidis G. P., Achilias D. S.: Chemical recycling of poly(ethylene terephthalate). Macromolecular Materials and Engineering, **292**, 128–146 (2007). DOI: 10.1002/mame.200600341

[10] Shukla S. R., Harad A. M., Jawale L. S.: Chemical recycling of PET waste into hydrophobic textile dyestuffs. Polymer Degradation and Stability, **94**, 604–609 (2009). DOI: 10.1016/j.polymdegradstab.2009.01.007

[11] Nikles D. E., Farahat M. S.: New motivation for the depolymerization products derived from poly(ethylene terephthalate) (PET) waste: A review. Macromolecular Materials and Engineering, **290**, 13–30 (2005). DOI: 10.1002/mame.200400186

[12] Ghaemy M., Behzadi F.: Unsaturated polyester from glycolized PET recycled from post-consumer soft-drink bottles. Iranian Polymer Journal, **11**, 77–83 (2002).

[13] Roy P. K., Mathur R., Kumar D., Rajagopal C.: Tertiary recycling of poly(ethylene terephthalate) wastes for production of polyurethane–polyisocyanurate foams. Journal of Environmental Chemical Engineering, **1**, 1062–1069 (2013). DOI: 10.1016/j.jece.2013.08.019

[14] Kathalewar M., Dhopatkar N., Pacharane B., Sabnis A., Raut P., Bhave V.: Chemical recycling of PET using neopentyl glycol: Reaction kinetics and preparation of polyurethane coatings. Progress in Organic Coatings, **76**, 147–156 (2013). DOI: 10.1016/j.porgcoat.2012.08.023

[15] Patel M. R., Patel J. V., Sinha V. K.: Polymeric precursors from PET waste and their application in polyurethane coatings. Polymer Degradation and Stability, **90**, 111–115 (2005). DOI: 10.1016/j.polymdegradstab.2005.02.017

[16] Auvergne R., Saint-Loup R., Joly-Duhamel C., Robin J. J., Boutevin B.: UV curing of a novel resin derived from poly(ethylene terephthalate). Journal of Polymer Science Part A: Polymer Chemistry, **45**, 1324–1335 (2007). DOI: 10.1002/pola.21904

[17] Patel M. R., Patel J. V., Sinha V. K.: Glycolyzed PET waste and castor oil-based polyols for two-pack coating systems. Polymer International, **55**, 1315–1322 (2006). DOI: 10.1002/pi.2086

[18] Atta A. M., Elnagdy S. I., Manar E. A-R., Elsaeed S. M., Abdel-Azim A-A. A.: Compressive properties and curing behaviour of unsaturated polyester resins in the presence of vinyl ester resins derived from recycled poly (ethylene terephthalate). Journal of Polymer Research, **12**, 373–383 (2005). DOI: 10.1007/s10965-005-1638-3

[19] Karayannidis G. P., Achilias D. S., Sideridou I. D., Bikiaris D. N.: Alkyd resins derived from glycolized waste poly(ethylene terephthalate). European Polymer Journal, **41**, 201–210 (2005). DOI: 10.1016/j.eurpolymj.2004.10.001

[20] Al-Salem S. M., Lettieri P., Baeyens J.: Recycling and recovery routes of plastic solid waste (PSW): A review. Waste Management, **29**, 2625–2643 (2009). DOI: 10.1016/j.wasman.2009.06.004

[21] Dehghani A., Ardekani S. M., Al-Maadeed M. A., Hassan A., Wahit M. U.: Mechanical and thermal properties of date palm leaf fiber reinforced recycled poly (ethylene terephthalate) composites. Materials and Design, **5**, 841–848 (2013). DOI: 10.1016/j.matdes.2013.06.022

[22] Shukla S. R., Harad A. M., Jawale L. S.: Recycling of waste PET into useful textile auxiliaries. Waste Management, **28**, 51–56 (2008). DOI: 10.1016/J.WASMAN.2006.11.002

[23] Viana M. E., Riul A., Carvalho G. M., Rubira A. F., Muniz E. C.: Chemical recycling of PET by catalyzed glycolysis: Kinetics of the heterogeneous reaction. Chemical Engineering Journal, **173**, 210–219 (2011). DOI: 10.1016/j.cej.2011.07.031

[24] Imran M., Kim D. H., Al-Masry W. A., Mahmood A., Hassan A., Haider S., Ramay S. M.: Manganese-, cobalt-, and zinc-based mixed-oxide spinels as novel catalysts for the chemical recycling of poly(ethylene terephthalate) via glycolysis. Polymer Degradation and Stability, **98**, 904–915 (2013). DOI: 10.1016/j.polymdegradstab.2013.01.007

[25] López-Fonseca R., Duque-Ingunza I., De Rivas B., Arnaiz S., Gutiérrez-Ortiz J. I.: Chemical recycling of post-consumer PET wastes by glycolysis in the presence of metal salts. Polymer Degradation and Stability, **95**, 1022–1028 (2010). DOI: 10.1016/j.polymdegradstab.2010.03.007

[26] Wang H., Liu Y., Li Z., Zhang X., Zhang S., Zhang Y.: Glycolysis of poly(ethylene terephthalate) catalyzed by ionic liquids. European Polymer Journal, **45**, 1535–1544 (2009). DOI: 10.1016/j.eurpolymj.2009.01.025

[27] Pardal F., Tersac G.: Kinetics of poly(ethylene terephthalate) glycolysis by diethylene glycol. I. Evolution of liquid and solid phases. Polymer Degradation and Stability, **91**, 2840–2847 (2006). DOI: 10.1016/j.polymdegradstab.2006.09.009

[28] Baliga S., Wong W. T.: Depolymerization of poly(ethylene terephthalate) recycled from post-consumer soft-drink bottles. Journal of Polymer Science Part A: Polymer Chemistry, **27**, 2071–2082 (1989). DOI: 10.1002/pola.1989.080270625

[29] Ikladious N. E.: Recycling of poly(ethylene terephthalate): Identification of glycolysis products. Journal of Elastomers and Plastics, **32**, 140–151 (2000). DOI: 10.1177/009524430003200203

[30] Mansour S. H., Ikladious N. E.: Depolymerization of poly(ethylene terephthalate) wastes using 1,4-butanediol and triethylene glycol. Polymer Testing, **21**, 497–505 (2002). DOI: 10.1016/S0142-9418(01)00115-5

[31] Mansour S. H., Abd-El-Messieh S. L., Ikladious N. E.: Utilization of some oligomers based on poly(ethylene terephthalate) wastes as modifiers for polyvinyl chloride. Journal of Applied Polymer Science, **85**, 2501–2509 (2002). DOI: 10.1002/app.10608

[32] Colomines G., Robin J-J., Tersac G.: Study of the glycolysis of PET by oligoesters. Polymer, **46**, 3230–3247 (2005). DOI: 10.1016/j.polymer.2005.02.047

[33] Colomines G., Rivas F., Lacoste M-L., Robin J-J.: Study of polyurethane formulations containing diols obtained via glycolysis of poly(ethylene terephthalate) (PET) by oligoesters diols through a reactive extrusion process. Macromolecular Materials and Engineering, **290**, 710–720 (2005).
DOI: 10.1002/mame.200400391

[34] Zahedi A. R., Rafizadeh M., Ghafarian S. R.: Unsaturated polyester resin via chemical recycling of off-grade poly(ethylene terephthalate). Polymer International, **58**, 1084–1091 (2009).
DOI: 10.1002/pi.2637

[35] Saint-Loup R., Robin J-J., Boutevin B.: Synthesis of poly(ethylene terephthalate)-*block*-poly(tetramethylene oxide) copolymer by direct polyesterification of reactive oligomers. Macromolecular Chemistry and Physics, **204**, 970–982 (2003).
DOI: 10.1002/macp.200390072

[36] Michel A., Cassagnau P., Argalon D. M., Robin J. J.: Synthesis of diols by the alcoholysis of molten polyesters with a diol or ether-diol in the presence of a catalyst, useful for the chemical vaporization of thermoplastic waste material particularly terephthalates. Fr Patent 2825701-A1, France (2001).

[37] Lusinchi J. M., Pietrasanta Y., Robin J. J., Boutevin B.: Recycling of PET and PVC wastes. Journal of Applied Polymer Science, **69**, 657–665 (1998).
DOI: 10.1002/(SICI)1097-4628(19980725)69:4<657::AID-APP4>3.0.CO;2-I

[38] Ma D., Zhang G., Huang Z., Luo X.: Synthesis and chain structure of ethylene terephthalate–ε-caprolactone copolyesters. Journal of Polymer Science Part A: Polymer Chemistry, **36**, 2961–2969 (1998).
DOI: 10.1002/(SICI)1099-0518(19981130)36:16<2961::AID-POLA14>3.0.CO;2-T

[39] Laurienzo P., Immirzi B., Malinconico M.: A preliminary investigation on the use of poly[(ethylene terephthalate)-*co*-(ε-caprolactone)] copolymer as compatibiliser of HDPE/PET blends. Macromolecular Materials and Engineering, **286**, 248–253 (2001).
DOI: 10.1002/1439-2054(20010401)286:4<248::AID-MAME248>3.0.CO;2-9

[40] Pesneau I., Grégoire M., Michel A.: Catalytic aspect of chemical modifications of polymers by transesterification: NMR study with model compounds. Journal of Applied Polymer Science, **79**, 1556–1562 (2000).
DOI: 10.1002/1097-4628(20010228)79:9<1556::AID-APP30>3.0.CO;2-F

[41] Maafi E. M., Malek F., Tighzert L., Laoutid F., Dubois P.: Synthesis and thermal properties of new copolyesters based on polycaprolactone. e-Polymers, no.027 (2012).
DOI: 10.1515/epoly.2012.12.1.304

[42] Siling M. I., Laricheva T. N.: Titanium compounds as catalysts for esterification and transesterification. Russian Chemical Reviews, **65**, 279–286 (1996).
DOI: 10.1070/RC1996v065n03ABEH000210

[43] Fradet A., Marechal E.: Models for polyesterification kinetics. II. Esterification kinetics in nonpolar medium. Journal of Macromolecular Science Part A: Chemistry, **17**, 859–879 (1982).
DOI: 10.1080/00222338208063277

[44] Seebach D., Hungerbühler E., Naef R., Schnurrenberger P., Weidmann B., Züger M.: Titanate-mediated transesterifications with functionalized substrates. Synthesis, **1982**, 138–141 (1982).
DOI: 10.1055/s-1982-29718

[45] Park S. S., Chae S. H., Im S. S.: Transesterification and crystallization behavior of poly(butylene succinate)/poly(butylene terephthalate) block copolymers. Journal of Polymer Science Part A: Polymer Chemistry, **36**, 147–156 (1998).
DOI: 10.1002/(SICI)1099-0518(19980115)36:1<147::AID-POLA19>3.0.CO;2-J

[46] Ma D-Z, Prud'homme R. E.: Miscibility of caprolactone/ethylene terephthalate copolymers with chlorinated polymers: A differential scanning calorimetry and Fourier transform infra-red study. Polymer, **31**, 917–923 (1990).
DOI: 10.1016/0032-3861(90)90056-5

[47] Wei K-H., Ho J-C.: The role of transesterification on the miscibility in blends of polycarbonate and liquid crystalline copolyester. Macromolecules, **30**, 1587–1593 (1997).
DOI: 10.1021/ma9615260

eXPRESS Polymer Letters Vol.8, No.8 (2014) 554–564
Available online at www.expresspolymlett.com
DOI: 10.3144/expresspolymlett.2014.59

Study of polycaprolactone wet electrospinning process

E. Kostakova[1*], *M. Seps*[2], *P. Pokorny*[1], *D. Lukas*[1]

[1]Department of Nonwovens and Nanofibrous Materials, Faculty of Textile Engineering, Technical University of Liberec, Studentska 2, 46117 Liberec 1, Czech Republic
[2]Institute of Novel Technologies and Applied Informatics, Faculty of Mechatronics, Informatics and Interdisciplinary Studies, Technical University of Liberec, Studentska 2, 46117 Liberec, Czech Republic

Received 6 February 2014; accepted in revised form 12 April 2014

Abstract. Wet electrospinning is a useful method for 3-dimensional structure control of nanofibrous materials. This innovative technology uses a liquid collector instead of the metal one commonly used for standard electrospinning. The article compares the internal structural features of polycaprolactone (PCL) nanofibrous materials prepared by both technologies. We analyze the influence of different water/ethanol compositions used as a liquid collector on the morphology of the resultant polycaprolactone nanofibrous materials. Scanning electron micro-photographs have revealed a bimodal structure in the wet electrospun materials composed of micro and nanofibers uniformly distributed across the sample bulk. We have shown that the full-faced, twofold fiber distribution is due to the solvent composition and is induced and enhanced by increasing the ethanol weight ratio. Moreover, the comparison of fibrous layers morphology obtained by wet and dry spinning have revealed that beads that frequently appeared in dry spun materials are created by Plateau-Rayleigh instability of the fraction of thicker fibers. Theoretical conditions for spontaneous and complete immersion of cylindrical fibers into a liquid collector are also derived here.

Keywords: *nanomaterials, wet electrospinning, biodegradable polymers, polycaprolactone, liquid collector*

1. Introduction

Wet electrospinning is a variant of the well-known electrospinning technology. The modification is based on the usage of a liquid collector instead of a solid, mostly metallic one. Wet electrospinning was first introduced in [1, 2] as a method for the lab-scale production of nanofibrous scaffolds for tissue engineering. To produce bulky and fluffy material using the common electrospinning method is a tricky matter. This task could be achieved either using special collectors [3] or by the usage of porogen particles, that is, chemical blowing agents, imbedded in between the nanofibers [4]. Wet electrospinning is a relatively simple and effective method to produce three dimensional (sponge-like) materials without sophisticated devices and without special chemical additives. The main application of such bulky materials is predominant in tissue engineering. Materials produced by wet-electrospinning are poly(glycolic acid) [5], chitin [6], cellulose [7], poly(trimethylenecarbonate-co-ε-caprolactone)-block-poly-(p-dioxanone) [8], copolymer of poly(glycolic acid) and poly(lactic acid) and blend of polycaprolactone and collagen or polycaprolactone and elastine [9]. A detailed study devoted to the immersion precipitation process in the electrospinning of polyacrylonitrile (PAN) dissolved in N,N-dimethyl-formamide (DMF) was developed by Fang *et al.* [10]. The Fang group demonstrated that using a non-solvent as a coagulant, ethanol in this case, polymer solution jets of PAN-DMF can be solidified rapidly resulting in instantaneously 'frozen' solid structures that can then

*Corresponding author, e-mail: eva.kostakova@tul.cz

be observed using scanning electron microscopy (SEM). The research confirms the important effect of the liquid collector bath height, the collecting distance, the electric field intensity and the concentration of the original polymer solution on the final morphology. We have used the Fang group method to study the evolution of PCL fiber morphology during wet electrospinning.

The immersion precipitation is a widely used method of classic fiber spinning technologies. In this respect, the wet electrospinning is a variant of the classic wet fiber spinning method. In this process the spinneret is submerged in a chemical bath that is a non-solvent for the polymer but which is compatible with the used solvent of the polymer [11]. Compared to the classic wet spinning process, wherein the nozzles are directly immersed into a coagulation bath, a small air gap (usually about 10 mm) is between the nozzle and the coagulation bath in the dry-jet-wet spinning process [12]. The air gap prevents polymer precipitation inside the spinnerets. The formation of a 'skin' of coagulated polymer occurs on first contact between a polymer jet filament and the coagulation bath [13]. The 'skin' clearly prevents the fiber from breaking up into spherical drops due to Plateau-Rayleigh instability [14]. This instability usually appears in the electrospinning of extremely dilute polymer solutions, where the resultant droplet formations are described as a 'pearl effect' on the fibers, 'beads-on-a-string', or simply as 'polymer beads' [15].

This study focuses on PCL (dissolved in chloroform/ethanol) wet electrospinning with water/ethanol mixtures employed as the liquid collector. The influence of the liquid collector composition on the final electrospun fibrous structure is studied here. The experiments are accompanied by theoretical analysis to suggest the general conditions needed for the production of bulky fibrous materials by wet electrospinning technology. The bulky, biodegradable, fibrous materials are of great interest for use as scaffolds for tissue engineering and this article provides a detailed study of the wet electrospinning process leading to their laboratory manufacture.

2. Materials and methods

Poly-ε-caprolactone (PCL), having an average molecular weight of 42 500 [M_n], density 1.145 g·cm^{-3}, melting point 60°C from Sigma Aldrich Inc. and dissolved in a chloroform/ethanol mixture (9:1 by weight), is mixed for 24 hours by a magnetic stirrer. The polymer concentration in the solution is 15 wt%. The solution of PCL in pure chloroform is used to evaluate the influence of the ethanol in the three component PCL solution. The dish of the liquid collector used for wet electrospinning is filled with a mixture of distilled water and ethanol at various volume fractions (10:0; 9:1; 8:2; 7:3; 6:4; 5:5; 4:6; 3:7; 2:8; 1:9; 0:10).

The electrospinning apparatus used for wet electrospinning experiments (Figure 1) consists of a syringe equipped with a metal hypodermic needle of inter-

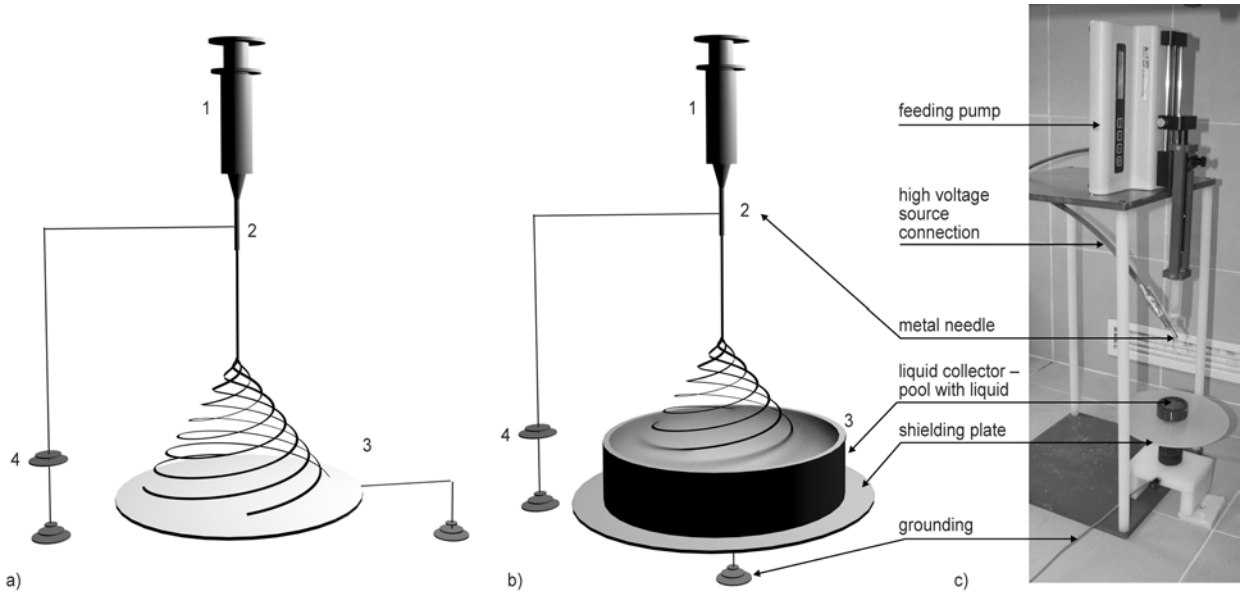

Figure 1. A schematic diagram and a photo of the standard dry needle electrospinning apparatus (a), wet electrospinning (b) and a photo of the device used in the experiments (c). The diagram shows the syringe connected to the feeding pump (1); metal hypodermic needle (2); metallic or liquid collector (3) and grounded high voltage source (4).

nal diameter 0.9 mm and length 33 mm. The needle is connected to the positive pole of a high voltage source (Spellman SL 150) and placed in the feeding device (KDScientific KDS-100). A grounded metallic plate is placed inside the dish/pool filled with the collector liquid. A shielding plate made of polyvinyl chloride (PVC) was used to focus a jet into the liquid collector. The process parameters are: positive voltage of 20 kV at the needle; the distance between needle end and the liquid collector surface is adjusted to 100 mm; pool depth 10 mm; pool inner diameter 40 mm; feeding velocity 7 mL·h^{-1}. Each sample was prepared from 0.5 mL of PCL solution, thus the final average area mass density of the electrospun material is about 68 g·m^{-2}. The wet electrospun samples were dried at a laboratory temperature of 20°C and a relative air humidity of 60±5 %RH.

The surface tension (bubble tension meter Krüss PocketDyne) and the conductivity (WTW Inolab GnInd 720) of the collector liquid were measured. Samples structures were analyzed using scanning electron microscopy (FEI Company – Phenom) and image analyzer software (Lucia G 4.82, LIM). Cross-sectional micro-photographs were obtained from samples broken at low temperature in liquid Nitrogen.

3. Results and discussion

The results presented here are divided into two main parts. The first part describes the fiber morphologies obtained using various conditions for the PCL wet electrospinning process. The last part focuses on the influence of the liquid collector on the electrospinning process and the material structure, that is, the creation of nanofibers, microfibers and beads in various combinations. These morphological transmutations are closely related with the varying conditions under which the wet electrospinning processes were run. Explanations of the causes of the transmutations are discussed thereafter.

3.1. Fiber morphology

The wet electrospun samples had a similar total surface density, about 60 g·m^{-2}, and dry thickness of 500±20 μm. The surface mass density was smaller than expected bulk one, because some fibers were able to stay at the edges of the pool or did not fly directly onto the liquid collector surface. The scanning electron microscope images reveal an inner structure composed of fibers belonging to two groups of distinct diameters. Figure 2a shows representative sample morphology produced using the liquid collector consisting of 90 wt% of ethanol. In this case, the diameters of the nanofibers group range from 95 up to 1000 nm, while the diameters of the microfiber fraction range between 2700–5000 nm as can be seen in Figure 3. The average diameter of the nanofibers group is 239±94 nm, while the average diameter of the microfiber fraction is 3664±731 nm, see Figure 2a, 2b and Figure 3. Diameters of fibers electrospun onto the metal plate collector was measured for comparison. Their average diameter is 162±62 nm. This dry electrospun material consists of nanofibers that only interconnect the spherical particles/beads having an average equivalent diameter of 14.6±4.2 μm, see Figure 2c. A microfiber fraction without any nanofibrous element is generated when pure chloroform is used as a solvent and wet electrospinning is performed into the water/ethanol (1:9) liquid collector. The fiber diameter of this wet electropun PCL material is 2.0±0.6 μm, as shown in Figure 2d. Thanks to the wet electrospinning method, microfibers are solidified in the liquid of the collector (see Figure 2a and 2b). Therefore the Plateau-Rayleigh instability does not develop in this case unlike in the sample created from the same PCL solution by classic electrospinning that uses the metal plate collector. In the latter, originally created microfibers are detached from the spherical polymer bodies interconnected by nanofibers only (see Figure 2c). When electrospinning onto the water surface took longer than in the previously described experiments, that is, more than 0.5 mL of solution is delivered, then special structures consisting of a 'frozen' microfibers and drops developed from them were found (Figure 4).

The twofold structure of the fibers, as depicted in Figure 2a and 2b, is clearly caused by the two-component solvent (chloroform/ethanol). Chloroform is a good solvent for PCL, but ethanol is not. The solvent composition influences the final fiber structure. This statement results from the fact that the wet electrospun PCL material from chloroform solution only, see Figure 2d, does not generate the dual structure, that is, it is composed of fibers of nearly uniform diameters. The structure of the wet electrospun PCL from the chloroform/ethanol solution into the mixture of water/ethanol results in a dual structured material composed of micro and nanofibers. Conversely, classically electrospun chloroform/ethanol solution

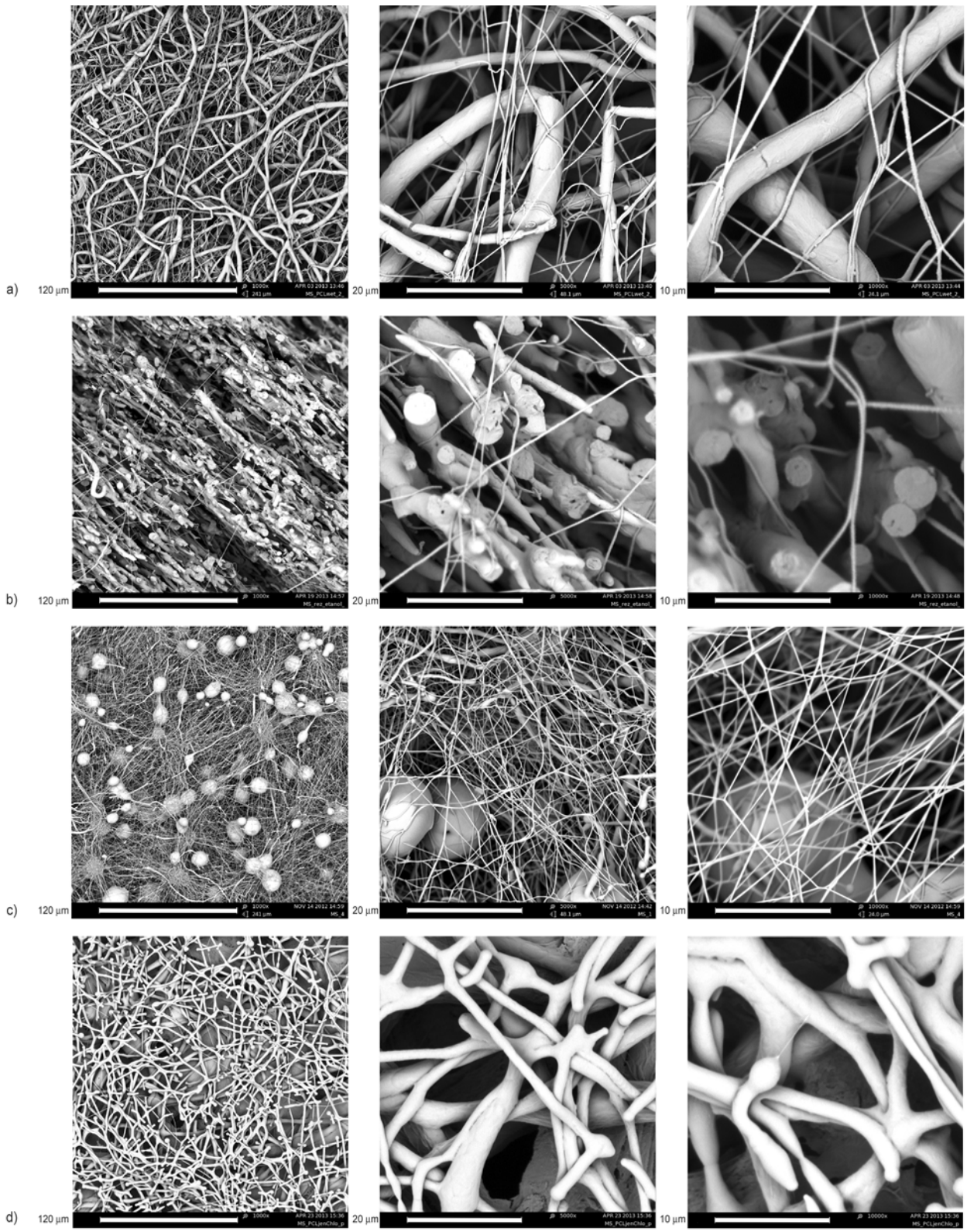

Figure 2. Scanning electron images of electrospun materials – three images in line with different magnification for each of these materials: (a) PCL fibers (from chloroform/ethanol 9:1 solution) wet electrospun into water/ethanol (1:9) liquid collector; (b) cross-sectional view of the same sample – PCL fibers (from chloroform/ethanol 9:1 solution) wet electrospun into water/ethanol (1:9) liquid collector; (c) PCL material electrospun from chloroform/ethanol 9:1 solution onto the metal plate collector; (d) PCL nanofibrous layer electrospun from pure chloroform solution into water/ethanol (1:9) liquid collector. The scale is 120 µm on the left, 20 µm in the middle and 10 µm on the right side.

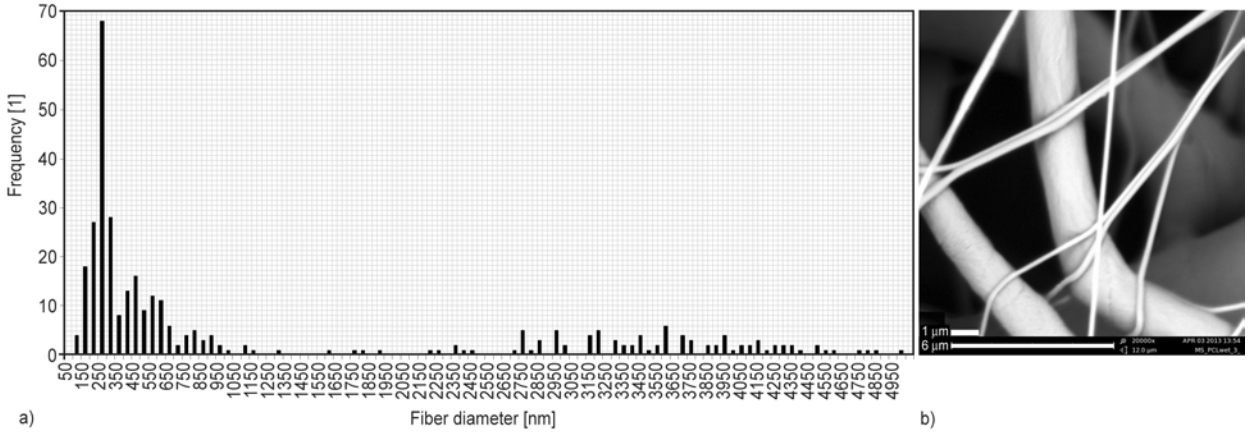

Figure 3. Histogram of fiber diameters in the PCL fibrous material electrospun into the liquid collector (water/ethanol weight ratio 1:9) (a), and SEM image representing dual structure of the wet electrospun material (scale bars represent 1 and 6 µm) is put in to proof the nanofibers presence in the sample (b).

Figure 4. Scanning electron images of electrospun material: PCL fibers (from chloroform/ethanol 9:1 solution) wet electrospun into distilled water only. 2.5 mL of PCL polymer solution were used, which is five times more than for the production of other samples described here. The scale is 240 µm.

of PCL provides beads on strings that are collected on a metallic collector. Thus one can conclude that the dual structure with micro and nanofibers is created in the spinning space between the spinning electrode and the collector, where whipping and branching of the polymer liquid jet occurs. Jet branching during the electrospinning process was described for various polymer solutions including PCL in the work [8]. The creation of beads in dry electrospun samples is the consequence of the Plateau-Rayleigh instability of a thicker fraction of fibers trapped on the collector. Probably, nanofibers do not undergo the Plateau-Rayleigh instability thanks to the higher degree of their cohesion compared with the much thicker microfibers that contain more solution. The characteristic hydrodynamic time for the fiber-bead transition is evidently longer than the flight time of a jet element inside the spinning space.

More detailed analysis shows (see Figure 5) that the fraction of nanofibers decreases with an increasing concentration of water in the liquid collector bath. These changes of the material's morphology are the consequence of increased surface tension of the liquid collector caused by the higher water ratio. The higher surface tension obstructs fibers from being immersed into the collector liquid and hence the collected fibers are not completely submerged. The fibers trapped on the liquid collector surface are in contact with other nascent fibers and it leads to a compact material structure with smaller pores and smaller fibers absorbed by bigger ones before their complete solidification. These changes are reflected in the transition from the three-dimensional structures with high porosity to a compact structure with lower porosity.

3.2. The effect of changing the liquid collector

Fibers were immersed fully into the water/ethanol bath only in the case of the high ethanol concentration that is, 2:8; 1:9 and 0:10 of weight ratios. In these cases a three-dimensional fibrous structure is created in the bulk of the liquid collector. Lower ethanol concentrations cause fibers to collect on the liquid surface as can be seen in Figure 6. The reason for this phenomenon is the increasing value of the col-

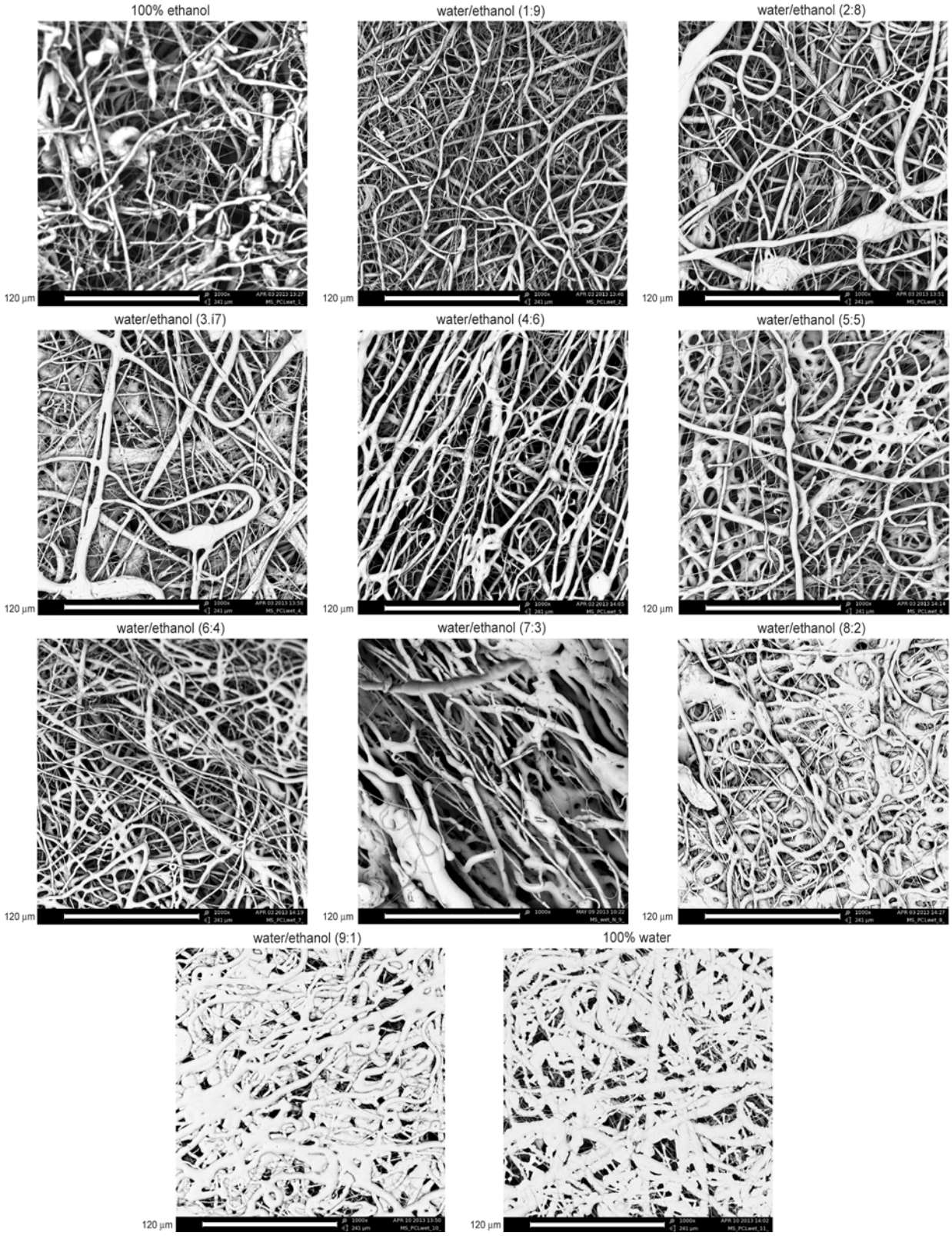

Figure 5. Scanning electron images of electrospun materials: PCL fibers (from chloroform/ethanol 9:1 solution) wet electrospun into different liquid collectors described above each image. Scale bar represents 120 µm.

lector liquid surface tension with the water ratio. Theoretical analysis of this phenomenon is introduced in paragraph 3.3.

The existence of the transition point when immersing PCL fibers into the collector liquid depicted in Figure 6 is supplemented by observing convention-

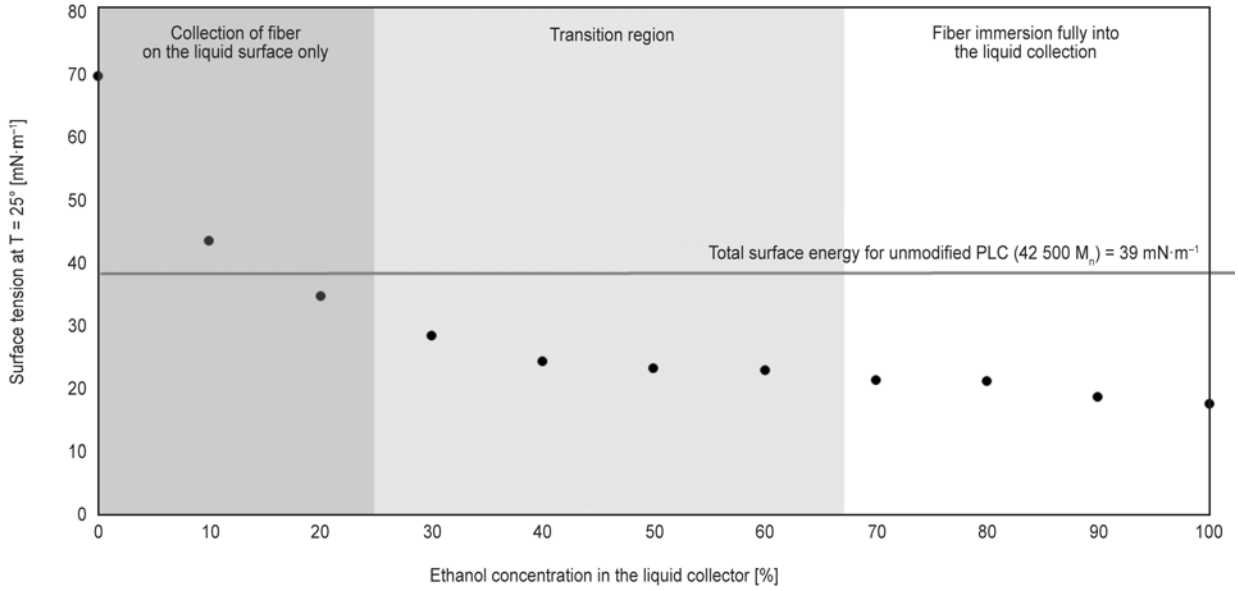

Figure 6. Graphical representation of the effect on fiber behavior of liquid collector composition: The horizontal line close to 40 mN·m^{-1} represents the transition region above which some fibers remain laying on the liquid collector level and only part of them are dipped in the liquid. Below this transition line all fibers are submerged in the liquid. Surface tension measurements of the liquid collector are carried out at temperature of 25°C. Standard deviations are below 0.2 mN·m^{-1}. Each measurement was repeated four times. The gray line in the graph represents the surface tension of PCL measured with the same PCL by Yildirim [16].

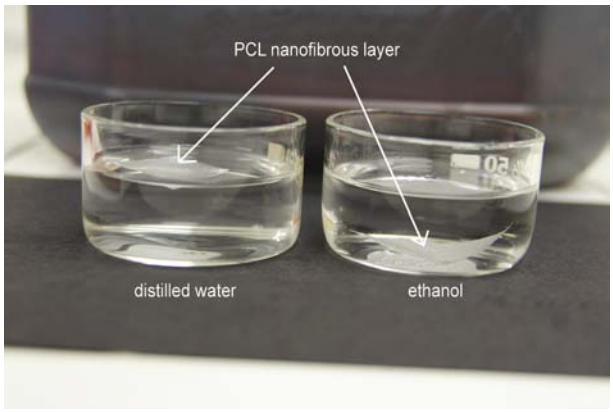

Figure 7. The photo of dry electrospun PCL layer having the surface density of 6 g·m^{-2} inserted into the distilled water (left side) and ethanol (right side)

ally electrospun PCL material after its being applied to distilled water and ethanol. The layer of nanofibers floats on the distilled water surface whereas it sinks into the ethanol bath as depicted in Figure 7.

The electrical conductivity of the liquids used as a collector slowly decreases with increasing ethanol concentration in the PCL solution as is visible in Figure 8. Both the electrical conductivity of the used collector liquid and the collecting distance are important in the process of wet electrospinning. The distance between the end of needle spinning electrode and the level of the liquid collector affect the electric field strength inside the spinning space as has been described in detail by Fang *et al*. [10].

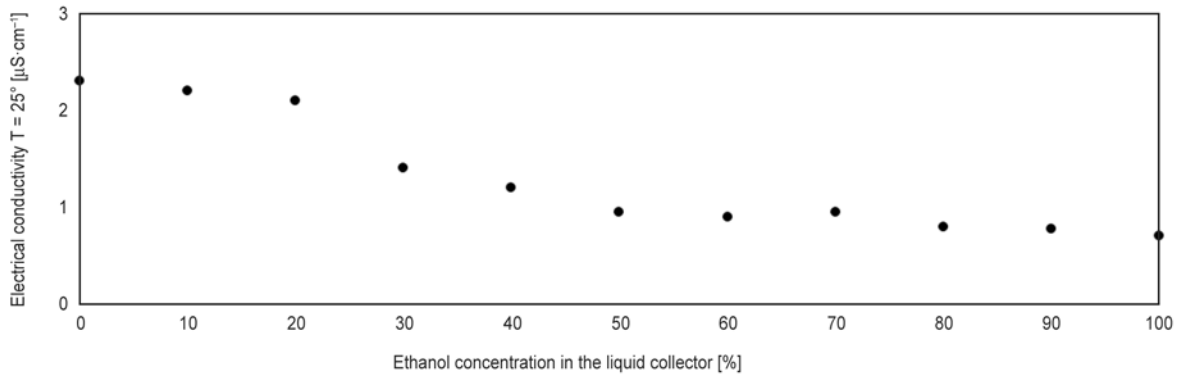

Figure 8. The collector liquid electrical conductivity depends on the ethanol concentration. The measurements were carried out at 25°C. Each measurement was repeated four times. Standard deviations are below 0.1 µS·cm^{-1}.

Based on the images from the scanning electron microscope (Figure 2a, 2b and Figure 5), the 9:1 water/ethanol mixture with a conductivity of 1.2 μS cm^{-1} and a surface tension of 26 $mN \cdot m^{-1}$ was chosen as the most appropriate liquid collector composition. Materials obtained using this kind of collector liquid have a fibrous three-dimensional structure with high porosity and almost no defects such as attached fibers or beads.

3.3. Lift force on a partly submerged cylinder

Efforts to clarify the problem of fiber mass immersion into a collector liquid during wet electrospinning led to the following theoretical explanation. The condition for spontaneous and complete immersion of a cylindrical fiber (cylinder) lying on a liquid surface are related to the study of water-spiders moving on the water's surface [17].

A lift force acting on a partly submerged cylinder in a liquid in rest is composed of two components. The first is the surface tension force f_T, while the second is called the pressure force f_P. Both these forces were introduced by Keller [18]. The nature of f_T and f_P is derived from the mechanical analysis of the cross-sectional geometry of the partly submerged cylinder depicted in Figure 9. The angle β that exists between a vertical line passing the cylinder axes and a line connecting the axis with a contact line is considered here in the interval $(0, \pi/2)$. The deformed liquid surface, due to the cylinder weight and the liquid surface tension γ, together with the immersed part of the cylinder forms a shape resembling a ship's hull below its waterline. The hull volume can be split into three departments subdivided by vertical walls. Two wing departments, denoted as 1 and 3, occupy a space equal to the liquid displaced by the meniscus up to the vertical walls containing the contact line of a liquid, gas and solid. The central department 2 is restricted by the same vertical walls, the immersed cylinder surface from the bottom and by the water line from above.

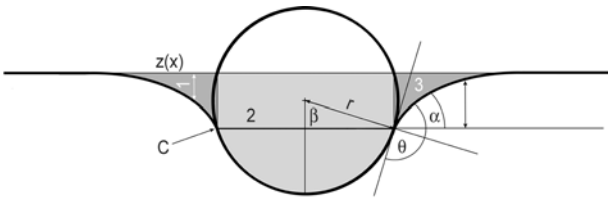

Figure 9. A liquid surface is deformed owing to a partly submerged cylinder. Solid, liquid and gas meet in a contact line *C*. Cylinder has the radius *r*. Contact angle is denoted by θ. The height of the curved liquid surface is described by the function $z(x)$.

Keller [18] showed that the surface tension force f_T is equal to the vertical component of the liquid surface tension multiplied by the total length of the two contact lines as well as being equal to the weight of the liquid displaced by the meniscus inside compartments 1 and 3.

The angle α contained by a horizontal line and the liquid surface at the contact line *C*, see Figure 9, can be expressed using $\tan\alpha_C = z'(x_C)$ where $z'(x_C)$ is the x derivative of the liquid-gas interface displacement $z(x)$ at the contact line. The interface $z(x)$ between a liquid and a gas at rest satisfies the Laplace-Young equation (Equation (1)):

$$\rho g z = \gamma \frac{z''}{(1 + z'^2)^{3/2}} \tag{1}$$

where ρ is the liquid density and g denotes the acceleration due to gravity. The differential operator identity $\frac{d}{dx} = \frac{dz}{dx}\frac{d}{dz}$ allows us to write a second x derivative of z as $z'' = z'\frac{dz'}{dz} = \frac{1}{2}\frac{d}{dz}z'^2$. Introducing the capillary constant, $a = \sqrt{2\gamma/(\rho g)}$, one obtains the first integral of the Relation (1) in the form (Equation (2)):

$$\int \frac{2z}{a^2} dz = \frac{1}{2}\int \frac{dz'^2}{(1 + z'^2)^{3/2}} \tag{2}$$

The relation $z' = \sqrt{\frac{a^4}{(Aa^2 - z^2)^2} - 1}$ between the tangent of the liquid meniscus slope $z'(x) = \tan\alpha$ and its displacement $z(x)$ is derived from the integration of Equation (2) as shown in [19]. Conditions at infinity, $z = z' = 0$ for $x \to \infty$, result in $A = 1$. Dimensionless displacement $Z = z/a$, introduced here for the sake of brevity, allows us to express the last relation in a comprehensive manner (Equation (3)):

$$\tan\alpha = z' = a\frac{dZ}{dx} = \pm Z\frac{\sqrt{2 - Z^2}}{1 - Z^2} \tag{3}$$

Integration of Equation (3) gives the liquid surface profile curve (Equation (4)):

$$\frac{x - x_0}{a} = \sqrt{2 - Z^2} + \frac{1}{\sqrt{2}}\ln\frac{Z}{2(\sqrt{2} + \sqrt{2 - Z^2})} \tag{4}$$

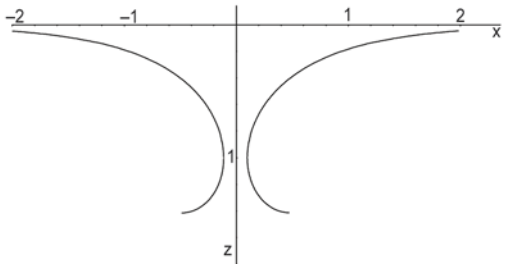

Figure 10. The shape of the liquid surface meniscus is plotted using inversion function $x(z)$ obtained from Equation (4)

where $x0$ is an integration constant. The shape of the liquid surface meniscus obtained from Relation (4) is shown in Figure 10.

Total lift force due to surface tension f_T is also given here, for the sake of brevity, in its dimensionless form F_T being normalized using the product of the liquid surface tension γ and the cylinder length l, that is, $F_T = f_T/(\gamma l)$. For F_T holds (Equation (5)):

$$F_T = 2\sin\alpha = \frac{2z'}{\sqrt{1+z'^2}} = 2Z\sqrt{2-Z^2} \qquad (5)$$

The pressure force f_P equals the weight of the liquid which would fill compartment 2. Similarly to the introduction of F_T, the dimensionless pressure force $F_P = f_P/(\gamma l)$ equals to ρg multiplied by the area of compartment 2, see Figure 9. The last compartment comprises a rectangle and a circular segment. The rectangle has an area $S_O = 2r\sin\beta \cdot z$, while the circular section area is $S_S = r^2(\beta - \cos\beta\sin\beta) = r^2\left[\beta - \frac{1}{2}\sin(2\beta)\right]$. For the angle β takes force $\beta = \pi - \theta + \arctan(z')$. Therefore the dimensionless pressure force F_P can be written in a comprehensive manner using the capillary length a and the dimensionless radius $R = r/a$ in the following manner (Equation (6)):

$$F_P = R^2\left[\beta - \frac{1}{2}\sin(2\beta)\right] + 2RZ\sin\beta \qquad (6)$$

For the total dimensionless lift force $F_L = F_T + F_P$ holds (Equation (7)):

$$F_L = 2Z\sqrt{2-Z^2} + R^2\left\{\pi - \theta + \arctan(z') - \frac{1}{2}\sin[2\pi - 2\theta + 2\arctan(z')]\right\} + 2RZ\sin[\pi - \theta + \arctan(z')] \qquad (7)$$

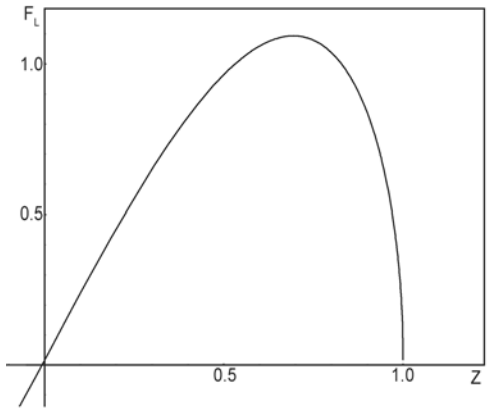

Figure 11. The relationship between F_L and Z for $R = 0.1$ and $\theta = 1.5$

where has to be substituted from (3). The relationship between F_L and Z for $R = 0.1$ and $\theta = 1.5$ is plotted in Figure 11.

Water surface tension against air at 25°C is $\gamma_{water} = 71.97$ mN/m and its density is $\rho = 997.0479$ kg/m^3. From that follows the water capillary length $a_{water} = 3.837$ mm. Ethanol at 20°C against air has the surface tension $\gamma_{ethanol} = 22.27$ mN/m, its density is 789.45 kg/m^3 and its capillary length is $a_{ethanol} = 2.399$ mm. Diameters of nanofibrous materials in this work are below $5\cdot10^{-6}$ m. Therefore their dimensionless radii, $R = r/a$, are small, $R \leq 6.515\cdot10^{-4}$ for water and $2.084\cdot10^{-3}$ for ethanol.

Assuming that a cylindrical fiber is long, its radius is around 1 μm and the contact angle θ is less than 90°, then the condition for the equilibrium between maximum lift force f_L and the cylinder weight w is (Equation (8)):

$$2\gamma L\sin\theta + \pi r^2\rho Lg = \pi r^2\rho_S Lg \qquad (8)$$

where ρ_S denotes the fiber mass density. From Relation (8) one derives the dimensionless relationship between the contact angle θ, the dimensionless fiber radius R and the ratio of densities ρ_S/ρ (Equation (9)).

$$\theta = \arcsin\left[\pi R^2\left(\frac{\rho_S}{\rho} - 1\right)\right] \qquad (9)$$

Substituting the following values: $r = 5 \cdot 10^{-6}$ m, $a = 3.837 \cdot 10^{-3}$ m, $\rho = 1000$ kg/m^3 and $\rho_S = 1145$ kg/m^3, one arrives at the contact angle θ value to immerse the cylindrical fiber that is negligibly small, that is. One concludes the analysis of the problem with a final statement, that complete submersion and fiber mass density greater than the mass density of liquid are two necessary conditions for immersion of a micro or nanofibers.

The contact angles of the solutions used as liquid collectors onto a PCL membrane were measured experimentally and found to support the above introduced theoretical condition for fiber immersion into a liquid (see Figure 12). The membrane made from four conventionally electrospun PCLs is produced by hot press at temperature 60°C and loading 3,5 kPa nanofibrous layers. The membrane's surface density is 24 g·m^{-2}.

The contact angle measurements proved that fibers immersing into the liquid collector have to have zero contact angle, which confirms the theoretical explanation written in this chapter. The results shown in Figure 12 showed the contact angle of a drop on the PCL membrane is zero for water/ethanol mixtures (6:4; 5:5; 4:6; 3:7; 2:8; 1:9; 0:10). PCL fibers were mainly found to collect during wet electrospinning on the liquid collector surface where there were higher contact angles (see Figure 6).

4. Conclusions

Wet electrospun material morphologies are compared with those obtained by common electrospinning that employs a metallic collector. The comparison of internal morphologies of dry and wet electrospun materials shows that PCL beads appearing in dry spun fibers are generated by a fraction of thicker fibers developed during electrospinning process. These thicker fibers were generated in the whipping zone of a jet that has been trapped using instantaneous solidification caused by immersion of the jet into the non-solvent of the liquid collector. A very important phenomenon which was found during these experiments was the relatively slow dynamics of the creation of big PCL droplets between nanofibers. These droplets are probably formed due to the 'slow' Plateau-Rayleigh instability that occurs after the not-completely-solidified fiber is captured on the solid collector. The theoretical explanation of

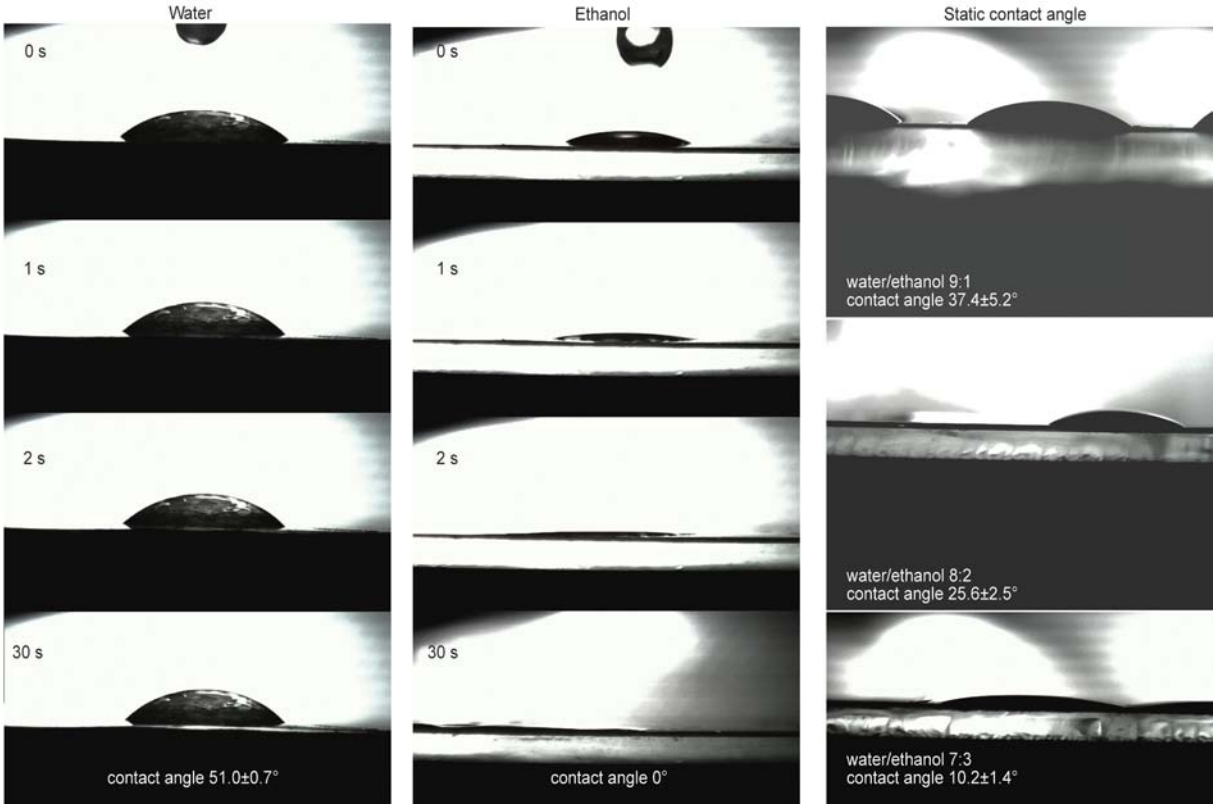

Figure 12. Photos of distilled water drops and water/ethanol mixture (9:1; 8:2; 7:3) drops placed onto a membrane made from PCL that are used for contact angle measurements. The static contact angles are measured 30 seconds after a drop impacts onto the membrane surface. For other water ethanol mixtures the resultant contact angles are the same as for pure ethanol drops. A drop falls down and disappears leaving a trace with zero contact angle.

spontaneous immersion of a cylindrical fiber into a liquid is also introduced here.

The main result of the study is the occurrence of the dual fibrous structures composed of microfibers and nanofibers distributed uniformly in all samples with a three-dimensional structure produced from PCL by wet electrospinning into ethanol/distilled water mixture. Such materials can be used as a scaffold for tissue engineering. The fibers of bigger diameter have better mechanical properties and a larger pore size is important for three-dimensional cell distribution. Fibers of smaller diameter ensure good cell adhesion inside the scaffold. The optimal material electrospun into the liquid reservoir water/ ethanol with weight ratio 1:9 for its three-dimensional structure and high porosity and with almost no structural defects was chosen as the best material for further in-vitro tests as a scaffold for tissue engineering.

Acknowledgements

The support for this research was provided by The Ministry of Interior of the Czech Republic, program BV II/2-VS, grant VG20102014049, 'Nanomaterials for personal protection against CBRN substances'. The paper was supported in part by the Project OP VaVpI Centre for Nanomaterials, Advanced Technologies and Innovation CZ.1.05/2.1.00/ 01.0005. D.L. acknowledges the support of GACR, Grant no. P208/12/0105. Authors thank to Jana Privratska for discussion about the mathematical derivations, Marcela Cudlinova for her help with Figure 4, Petr Mikes for his help with Figure 1; 10 and 11 and Jiri Militky for discussion about wet spinning technologies (all from Technical University of Liberec).

References

[1] Yokoyama Y., Hattori S., Yoshikawa C., Yasuda Y., Koyama H., Takato T., Kobayashi H.: Novel wet electrospinning system for fabrication of spongiform nanofiber 3-dimensional fabric. Materials Letters, **63**, 754–756 (2009).
DOI: 10.1016/j.matlet.2008.12.042

[2] Ali A. A., Al-Asmari A. Kh.: Wet-electrospun CuNP/carbon nanofibril composites: Potential application for micro surface-mounted components. Applied Nanoscience, **2**, 55–61 (2012).
DOI: 10.1007/s13204-011-0042-z

[3] Lukáš D., Sarkar A., Martinová L., Vodsed'álková K., Lubasová D., Chaloupek J., Pokorný P., Mikeš P., Chvojka J., Komárek M.: Physical principles of electrospinning (electrospinning as a nano-scale technology of the twenty-first century). Textile Progress, **41**, 59–140 (2009).
DOI: 10.1080/00405160902904641

[4] Zhong S., Zhang Y., Lim C. T.: Fabrication of large pores in electrospun nanofibrous scaffolds for cellular infiltration: A review. Tissue Engineering Part B: Reviews, **18**, 77–87 (2012).
DOI: 10.1089/ten.TEB.2011.0390

[5] Quan S-L., Kang S-G., Chin I-J.: Characterization of cellulose fibers electrospun using ionic liquid. Cellulose, **17**, 223–230 (2010).
DOI: 10.1007/s10570-009-9386-x

[6] Barber P. S., Griggs C. S., Bonner J. R., Rogers D.: Electrospinning of chitin nanofibers directly from an ionic liquid extract of shrimp shells. Green Chemistry, **15**, 601–607 (2013).
DOI: 10.1039/c2gc36582k

[7] Shin T. J., Park S. Y., Kim H. J., Lee H. J., Youk J. H.: Development of 3-D poly(trimethylenecarbonate-*co*-ε-caprolactone)-block-poly(*p*-dioxanone) scaffold for bone regeneration with high porosity using a wet electrospinning method. Biotechnology Letters, **32**, 877–882 (2010).
DOI: 10.1007/s10529-010-0235-7

[8] Eberli D.: Tissue engineering. InTech, Rijeka (2010).

[9] Reneker D. H., Yarin A. L.: Electrospinning jets and polymer nanofibers. Polymer, **49**, 2387–2425 (2008).
DOI: 10.1016/j.polymer.2008.02.002

[10] Fang J., Wang H., Niu H., Lin T., Wang X.: Evolution of fiber morphology during electrospinning. Journal of Applied Polymer Science, **118**, 2553–2561 (2010).
DOI: 10.1002/app.32569

[11] Gupta V. B., Kothari V. K.: Manufactured fiber technology. Chapman and Hall, London (1997).

[12] Takajima T.: Advanced fiber spinning technology. Woodhead Publishing Limited, Cambridge (1994).

[13] Walczak Z. K.: Processes of fiber formation. Elsevier, Amsterdam (2002).

[14] Sattler R., Gier S., Eggers J., Wagner C.: The final stages of capillary break-up of polymer solutions. Physics of Fluids, **24**, 023101/1–023101/21 (2012).
DOI: 10.1063/1.3684750

[15] Brown P. J., Stevens K.: Nanofibers and nanotechnology in textiles. Woodhead, Cambridge (2007).

[16] Yildirim E. D.: Plasma and protein surface functionalization for three-dimensional polycaprolactone tissue scaffolds. PhD Thesis, Drexler University, College of Engineering (2010).

[17] Vella D., Mahdevan L.: The 'Cheerios effect'. American Journal of Physics, **73**, 817–825 (2005).
DOI: 10.1119/1.1898523

[18] Keller J. B.: Surface tension force on a partly submerged body. Physics of Fluids, **10**, 3009–3010 (1998).
DOI: 10.1063/1.869820

[19] Landau L. D., Lifshitz E. M.: Course of theoretical physics, Volume 6: Fluid mechanics. Pergamon Press, Oxford (1959).

eXPRESS Polymer Letters Vol.8, No.8 (2014) 565–573
Available online at www.expresspolymlett.com
DOI: 10.3144/expresspolymlett.2014.60

Graphene modified electrospun poly(vinyl alcohol) nanofibrous membranes for glucose oxidase immobilization

C. M. Wu[1*], *S. A. Yu*[1], *S. L. Lin*[2]

[1]Department of Materials Science and Engineering, National Taiwan University of Science and Technology, 10607 Taipei, Taiwan, R.O.C.
[2]Department of Fiber and Composite Materials, Feng Chia University, 40724 Taichung, Taiwan, R.O.C

Received 10 February 2014 ; accepted in revised form 18 April 2014

Abstract. In this study, poly(vinyl alcohol) (PVA)/Glucose oxidase (GOx)/graphene biocomposite membranes were prepared using an electrospinning technique and used for enzyme immobilization. The PVA/GOx/graphene membrane's morphology was examined by scanning electron microscopy (SEM) and transmission electron microscopy (TEM), while its electrochemical sensitivity was studied by chronoamperometry. Kinetic parameters were determined to clarify the role of graphene in enzyme immobilization, while a spectrophotometric assay was used to quantify the active enzyme. The results indicated that the presence of graphene helps to stabilize the enzyme's conformation, facilitate the catalytic reaction, and increase the survivability of the enzyme.

Keywords: *polymer membranes, electrospun, glucose biosensor, immobilization, graphene*

1. Introduction

Diabetes is an increasingly important worldwide public health problem. The metabolic disorder results from either insulin deficiency, in type 1 diabetic patients, or from insulin resistance and its complications in type 2 patients. Both conditions can result in hyperglycemia leading to blood glucose concentrations higher than the normal range 80–120 mg/dL (4.4–6.6 mM) [1]. The diagnosis and management of diabetes requires the careful monitoring of blood glucose levels. The glucose biosensor has thus become one of the most important physiological monitoring devices, accounting for about 85% of the entire biosensor market [1].

A biosensor is a device which combines an immobilized bio-recognition element with a transducer. It can monitor chemical substances on the inside or outside of an organism by generating a signal representative of the analyte's concentration after coupling the biochemical and transducer reactions [2]. Glucose biosensors are based on electrochemical principles and frequently employ enzymes as the biological recognition element. The biosensor's performance and sensitivity often strongly depends on the influence imposed on the enzyme's structure by immobilization. Such influences result from the choice of host molecule and the immobilization method used. In attempts to retain enzymatic activity and stability various molecules have been used to immobilize enzymes on different substrates, e.g. poly(vinyl alcohol) (PVA) [3], poly(ethylene oxide) (PEO) [4], chitosan [5], polymethylmethacrylate (PMMA) [6], poly(vinyl pyrrolidone) (PVP) [7] and polyurethane (PU) [8]. PVA is often used as an immobilization matrix because of its inherent non-toxicity, high thermal stability, good biocompatibility and its desirable physical properties such as its elastic nature, good film forming properties, and its

*Corresponding author, e-mail: cmwu@mail.ntust.edu.tw

high degree of swelling in aqueous solutions – all of which contribute to making it a good matrix for enzyme immobilization [9]. Different methods, such as the cross-linking of PVA [10], freeze-thawed PVA [11], enzyme encapsulation in PVA/silicate hybrid materials [3], have been successfully employed to immobilize the enzyme molecules in various membranes. However, because of the compaction and low-conductivity of the PVA membrane, substrate infiltration and electron transfer between the enzyme membrane and the electrode remains problematic [12].

Electrospinning has proved to be an efficient method for generating nanofibrous membranes with large surface area to volume ratios and high porosities, because electrospun nanofibrous membranes can immobilize biological molecules with higher loadings [13–15], while enzyme activity can be enhanced by decreasing the diffusion resistance of the substrate. In addition, nanofibrous membranes can be easy prepared *in situ* by electrospinning; the enzyme-immobilized materials therefore show great potential for biosensor development [16, 17].

Electrochemical biosensors using nanomaterials have recently attracted much attention. Many nanomaterials, such as carbon nanotubes [5, 18], gold nanoparticles [19, 20], and metal oxides [21, 22] have been used in biosensors. More recently a new class of carbon material, graphene, which is a two-dimensional sheet of carbon atoms, has attracted increasing attention with respect to its potential applications in phtoelectronic devices, supercapacitors, sensors and nanocomposites applications [6, 23–32]. Due to their planar morphology and thus larger accessible surface area, graphene may perform better than any other carbon-based materials for an electrode sensor fabrication. Kang *et al*. [6], reported the direct electrochemistry of GOx on graphene. Their results demonstrated that graphene possesses both an excellent electrochemical catalytic activity and an electron transfer promoting ability making it extremely attractive for applications in enzyme-based biosensors.

Shan *et al*. [25] prepared graphene sheets protected by polyvinylpyrrolidone that, exhibited high electrocatalytic activity towards the reduction of O_2 and H_2O_2, which could be stably dispersed in water. Because of their favorable electronic properties and biocompatibility, graphene-based composites accomplished the direct electron transfer of redox enzyme while maintaining a good level of bioactivity. The authors claimed direct electron transfer from the GOx via the graphene sheets. Shan *et al*. [26] also constructed graphene/Au/chitosan nanocomposite electrodes and suggested that the synergistic effect of graphene and Au nanoparticles might promote electrocatalysis towards H_2O_2. The high sensitivity and good stability of such a modified electrode contributed to the construction of a practical glucose biosensor. Su *et al*. [27] reported the synergy mechanism of electrospun PVA/chitosan nanofibers and graphene nanosheets for efficient glucose biosensing. These results indicate graphene shows significant potential for fabricating an electrochemical sensing interface. The graphene based enzyme sensor exhibited excellent sensitivity and long-term stability for measuring glucose. Song *et al*. [28] showed that graphene possesses intrinsic peroxidase catalytic activity due to the presence of carboxylic groups at the edges of the graphene sheets, so there is no need for the GOx enzyme; additionally, such a biosensor exhibits a longer stable shelf-life, as it does not contain any biomolecule within the matrix.

In our previous study [33, 34], PVA/GOx electrospun membranes, with porous structures and large specific surface areas, were demonstrated to have promising enzyme immobilization capabilities compared to cast membranes. In this work we have attempted to understand the interactions between graphene and GOx: here the effects of adding graphene on sensitivity, enzyme kinetics and the activity of electrospun nanofibrous membranes are presented.

2. Materials and testing methods

2.1. Material

Poly(vinyl alcohol) (PVA) 98~99% hydrolyzed, molecular weight 146 000–186 000 was purchased from Sigma-Aldrich. Graphene oxide aqueous solution (50 wt%, N002-PS) was purchased from Angstron Material Inc., U.S.A. Glucose oxidase (153 100 units/G, G7141, Sigma-Aldrich) was used in the form of powder as received. Disodium phosphate dodecahydrate ($Na_2HPO_4{\cdot}12H_2O$, Showa Chemical Industry Co.) and sodium hydrogen phosphate dihydrate ($NaH_2PO_4{\cdot}2H_2O$, Showa Chemical Industry Co., Japan) were used for preparing the phosphate buffer solution (PBS, 0.1M and pH 6.8). Dextrose Anhydrous (D(+)-Glucose) was pur-

chased from Showa Chemical Industry Co., Japan. Glutaraldehyde (GA) solution with 25% concentration and 4-Aminoanipyrine (4-AA), peroxidase (POD) with 150 U/mg and N-Ethyl-N-(2-hydroxy-3-sulfopropyl)-m-toluidine (EHSPT) were purchased from Sigma-Aldrich. A Pt electrode with a length of 10 mm, width of 10 mm and thickness of 0.5 mm was purchased from Leesan Precious Metal CO., LTD, Taiwan.

2.2. Sample preparations

2.2.1. Preparation of the electrospinning solution

A 7% (w/v) PVA solution was prepared by adding 7 g of PVA powder into 93 mL of distilled water. Then, the solution was heated and stirred at ~ 80°C for 3 hours, after which, the solution was kept at room temperature. The 7% (w/v) PVA solution was mixed with 14 mg of GOx powder and graphene oxide solution, creating the electrospinning solution. Solutions were prepared to have final contents equivalent to 0, 5, 10, 20 and 40 ppm graphene.

2.2.2. Preparation of the PVA/GOx electrospun membranes

A self-assembled electrospinning device with an injection spinneret (0.008 mL/min) powered by a syringe pump (KDS 101 Series, Kd scientific, USA) was used for the PVA/GOx membrane preparation. The syringe pump was connected to a Teflon tube attached to a stainless steel needle (0.31 mm internal diameter) that acted as the spinneret. A copper grid covered by construction paper acted as the collector. An electrostatic controller (LGC-300 series, Taiwell, Taiwan) connected to the collector, and a ground wire connected to the spinneret acted as the collector charging system. The PVA/GOx electrospun nanofibrous membranes were directly electrospun and deposited onto the Pt electrode (area 10 mm^2) under the following electrospinning conditions: applied voltage 14 kV, spinning time 10 min, and working distance 18 cm at 40% relative humidity (RH). Based on the experimental results, the addition of graphene did not influence the electrospinning behavior.

Aqueous solutions of glutaraldehyde and sulfuric acid were prepared for PVA nanofibrous membrane cross-linking. The concentrations of glutaraldehyde and sulfuric acid were 5 and 2.5%, respectively. PVA nanofibrous membranes were treated with the vapor of the cross-linking solutions for 15 min. Then the sample was rinsed in a PBS solution 3 times (5 min/each time).

2.3. Electrochemical measurements

In this study, the glucose biosensor's electrochemical measurements were made using a three-electrode system with a potentiostat (CH Instruments Electrochemical Analyzer) [3]. The auxiliary electrode was a Pt wire, and an Ag/AgCl electrode was used as a reference. The working potential was 0.8 V. Amperometric measurements were carried out under stirring, and the response current was marked with the change value (Δi) between the steady-state current and background current. All experiments were performed at room temperature.

2.4. Evaluation of enzyme activity

To study the activity of the immobilized enzyme in the PVA/GOx electrospun nanofibrous membranes, a simple, spectrophotometric assay was used. The enzyme activity for GOx at 30°C was measured using a UV-Vis Spectroscopy spectrophotometer (Chrom Tech, Singapore).

First, we prepared a working solution (25 mL), containing 0.1 M phosphate buffer (pH 5.7), 15% glucose solution, 0.5% 4-aminoanipyrine, 40 mM EHSPT solution, and 5 U/mL GOD. The samples, each within the range of 0.5 to 1.7 mg, were immersed in a working solution and mixed by gentle inversion. Then, we recorded the increase in absorbance of the quinoneimine dye formed, as shown by Equations (1)–(4), at 555 nm against water for 30 sec (8 times) in a spectrophotometer, thermostatically controlled at 30°C. The absorbance (per minute) was calculated from the initial linear portion of the curve. The reaction in the working solution was as follows (Equations (1) and (2)):

$$\text{B –D – Glucose} + O_2 + H_2O \xrightarrow{\text{glucose oxidase}} \text{D – Glucono – } \delta \text{ – lactone} + H_2O_2 \quad (1)$$

$$2H_2O_2 + 4 - AA + EHSPT \xrightarrow{POD} \text{Quinomeimine dye} + 4H_2O \quad (2)$$

The specific activity, expressed in μmol oxidized substrate/min/mg enzyme preparation, was calculated by the use of the Beer-Lambert law (Equations (3)):

$$Abs. = \varepsilon \cdot b \cdot c \quad (3)$$

where *Abs*. is the measured absorbance per minute, *b* is the light path length (in this case 1 cm), and *c* is the concentration [μmol/mL] of the measured substance (quinoneimine dye) at the absorbance concerned. The Millimolar extinction coefficient ε for the quinoneimine dye under the assay conditions is 32.8 cm^2/μmol. Because 1 U (enzyme activity) results in the formation of one micromole of hydrogen peroxide (half a micromole of quinoneimine dye) per minute, the activity of the immobilized enzyme in solution (25 mL) is 2·25c. When analyzing solid and semi-solid samples, which are weighed out for sample preparation, the activity [U/mg] is calculated from the amount weighed as Equation (4):

$$\text{GOx axtivity (U/mg of preparation)} = \frac{\text{GOx activity (U/mL sample solution)}}{\text{Weight}_{\text{sample}}\text{ (mg/mL sample solution)}} \quad (4)$$

$\text{Weight}_{\text{sample}}$ ~ the weight of sample [mg].

3. Results and discussion

3.1. The morphology of PVA/GOx electrospun nanofibrous membranes

Figure 1 shows the deposited configuration of the PVA/GOx electrospun membrane on the Pt electrode. The electrospun membrane was well-distributed on the Pt electrode and had a semitransparent appearance. Figure 2 shows the SEM image of the electrospun nanofibrous membrane after cross-linking. A partially dissolved porous structure was found in the cross-linked PVA electrospun nanofibrous membrane proving the existence of a large reaction area between glucose and GOx. The dispersion of graphene within the electrospun PVA nanofibers was examined by TEM and is shown in Figure 3. The graphene layers were folded and randomly distributed within the electrospun PVA nanofibers. The successful loading of graphene in PVA nanofibers may play an important role in the immobilization of

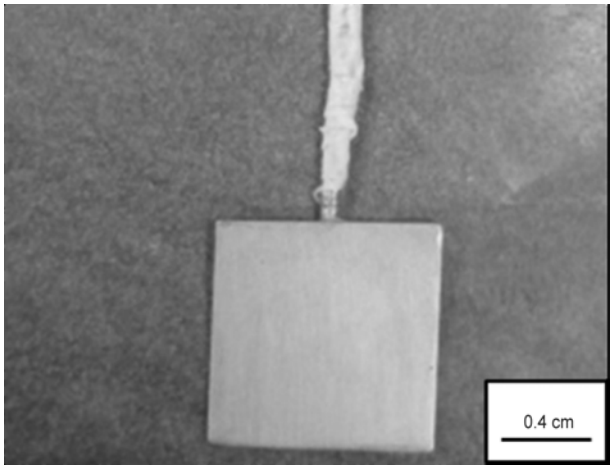

Figure 1. The deposited configuration of the electrospun membrane on the Pt electrode

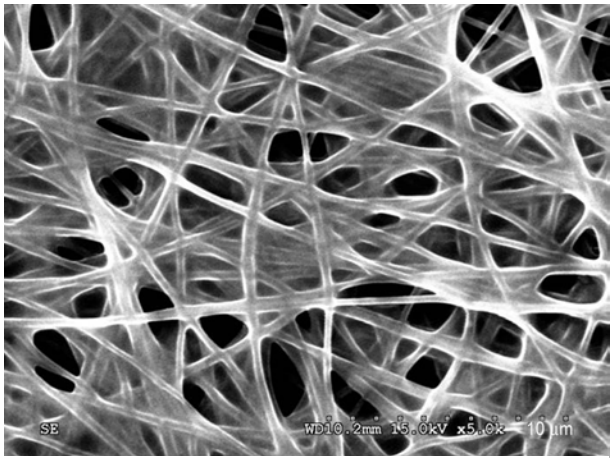

Figure 2. SEM image of the electrospun nanofibrous membrane after cross-linking

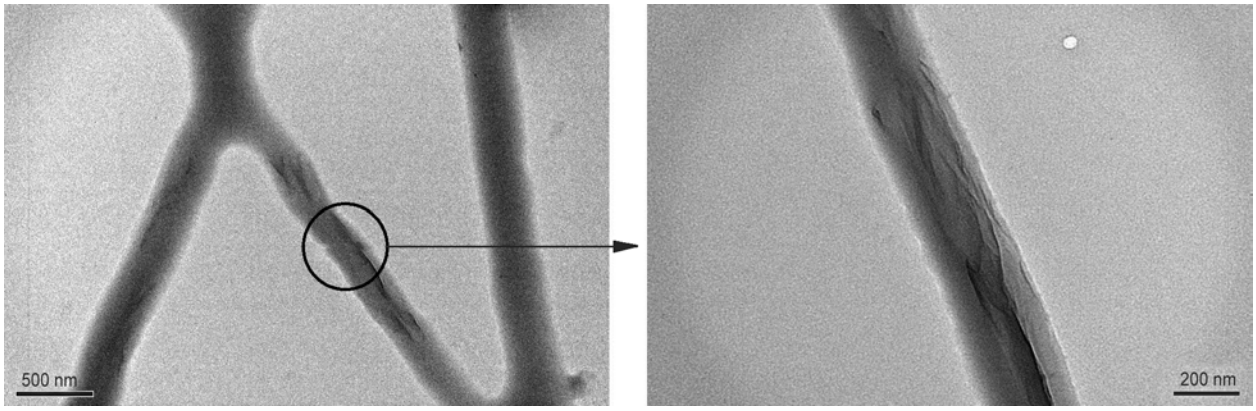

Figure 3. TEM image of the electrospun nanofibrous membrane modified by graphene using different magnifications

enzyme molecules and the access of enzymes to the substrate.

3.2. Electrochemical characterization

3.2.1. Sensitivity analysis

Figure 4 shows the current-time (*i-t*) curves of different PVA membrane samples containing various graphene contents obtained by the chronoamperometric method. The glucose concentration was successive increased, by adding the analyte, from 1 to 34 mM. The plot of current vs. glucose concentration in Figure 4 generated the calibration curves of PVA samples containing different content of graphene as shown in Figure 5. A linear response to current is apparent for glucose concentrations from 0 to 10 mM. The sensitivity of the PVA/GOx electrospun membrane was determined by the slope of the linear least-squares calibration plot over the range 0 to 10 mM, see Table 1. The sensitivity of the PVA/GOx electrospun membrane increased with increasing graphene concentrations up to 20 ppm, but decreased at 40 ppm. The highest sensitivity was 38.7 mA/mM, found for the PVA/GOx sample with 20 ppm graphene, representing a 109% increase compared to the PVA/GOx sample without graphene addition (sensitivity: 18.5 mA/mM). The sensitivity increase with increasing graphene additions is thought to result from enhanced enzyme conformational stabilization due to the presence of graphene, facilitating the electrocatalytic reaction while simultaneously increasing the enzyme's survivability. However, the sensitivity decrease at high graphene addition (40 ppm) may be attributed to the aggregation of graphene within the electrospun PVA nanofibers. A plateau in current response was observed for glucose concentrations beyond 10 mM, resulting from operation of Michaelis-Menten kinetics and will be discussed further in the next section.

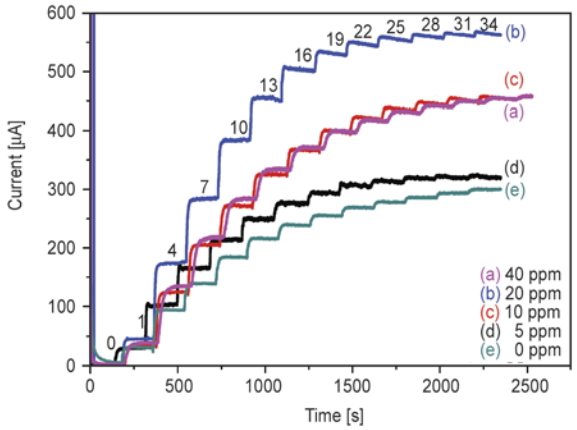

Figure 4. The current-time (*i-t*) curves of samples containing different graphene contents

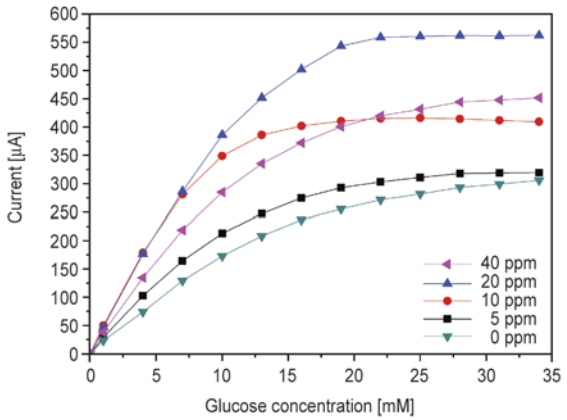

Figure 5. The resulting calibration curves of samples containing different content of grapheme

Figure 6 shows the amperometric response to successive additions of 1 and 4 mM glucose on the PVA/GOx samples with different graphene contents. It can be seen that the PVA/GOx membranes respond rapidly to the injection of glucose, and reach a steady-state current within 10–14 sec. after each injection. The fast response apparent with 20 ppm graphene is attributed to the fast electron transfer and good electrocatalytic properties provided by graphene and to the close contact between the GOx and the graphene layers. The close contact between the GOx and the graphene layers allows the glucose concentration change to be quickly monitored with the signal being transferred to the electrode through numerous electron transfer pathways provided by the graphene layer.

Compared to our previous study results [19] that showed the best performance of gold nanoparticles, added in PVA/GOx membranes, to have a sensitivity of 37.7 μA/mM and a response time of 5.7 sec;

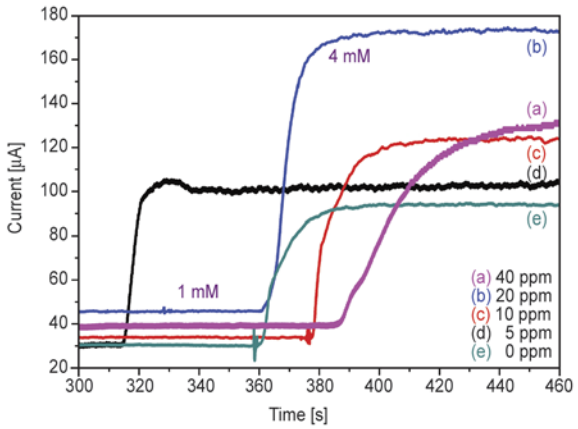

Figure 6. Amperometric response of PVA samples to successive additions of 1–4 mM glucose

Table 1. The amperometric response of PVA/GOx samples modified by graphene

Content [ppm]	0	5	10	20	40
Sensitivity [μA/mM]	18.50	21.40	35.30	38.70	28.50
Response time [s]	13.90	12.70	10.20	9.90	23.80
Reaction rate [μA/s]	3.52	7.92	8.22	9.76	2.43
K_m^{app} [mM]	13.20	4.20	3.20	1.10	13.80
I_{max} [μA]	434.80	357.10	476.20	588.20	454.50

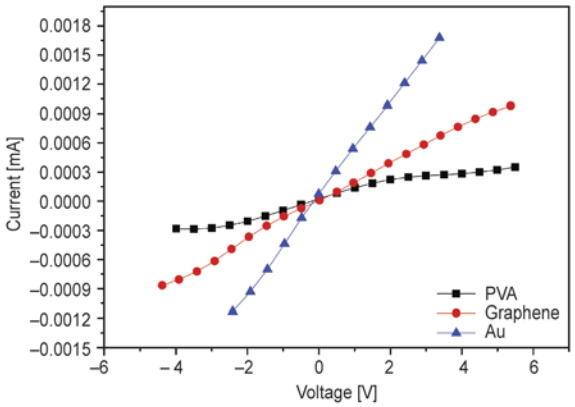

Figure 7. The current-to-voltage response for PVA and nanogold, graphene modified PVA electrospun membranes

membranes with added graphene showed a higher sensitivity, but a longer response time. We know that the layer structure of graphene nanoplates exhibits an electrical barrier leading to reduced conductivity. The current-to-voltage response for pure PVA and nanogold, graphene modified PVA membranes are shown in Figure 7. The determined values are $7.7 \cdot 10^{-5}$, $2.0 \cdot 10^{-4}$ and $4.9 \cdot 10^{-4}$ mhos for PVA, PVA/graphene and PVA/nanogold electrospun membrances respectively. Thus, the response time is influenced by electrical conductivity under similar sensitivity.

3.2.2. Enzyme kinetics

As shown in Figure 5, when the glucose concentration was high, the response current had a slow and non-linear increase. These results reveal a Michaelis-Menten dynamic characteristic. The apparent Michaelis-Menten constant (K_m^{app}) can be calculated from the Hanes-Woolf regression [3] as shown by Equations (5)–(7):

$$\frac{S}{I} = \frac{1}{I_{max}} S + \frac{K_m^{app}}{I_{max}} \quad (5)$$

$$I_{max} = \frac{1}{\text{Slope}} \quad (6)$$

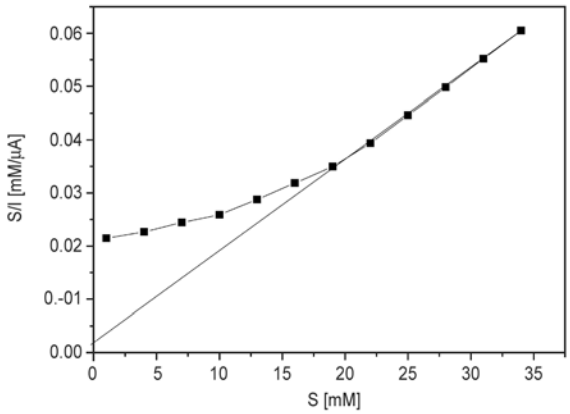

Figure 8. Hanes-Woolf curve for PVA/GOx electrospun membrane with 20 ppm graphene content

$$K_m^{app} = y - \text{intercept} \cdot I_{max} \quad (7)$$

where S is glucose concentration, I is the steady-state current, and I_{max} is the maximum current measured under saturated substrate conditions.

The K_m^{app}, which gives an indication of enzyme substrate kinetics for the biosensor, was estimated based on the data obtained from the S/I vs. S curve, shown in Figure 8. The K_m^{app} values for different PVA/GOx samples were determined and are listed in Table 1. The K_m^{app} value decreased with the increase in graphene concentration. The K_m^{app} value for the PVA/GOx sample without graphene was 13.2 mM, whereas a much smaller value: 1.1 mM was obtained for a sample with a 20 ppm graphene addition. The lower value of K_m^{app} proved that the addition of graphene could facilitate the electrocatalytic reaction between GOx and glucose while increasing the biological affinity of immobilized enzymes to glucose. The I_{max} value increased with increases in the graphene concentration. The results also support the notion of an electrocatalytic effect driving higher rates of enzyme reaction at high graphene loadings (20 ppm).

3.3. Enzyme activity

To study the activity of the immobilized enzymes in the PVA/GOx electrospun membranes a spectrophotometric assay was used. Figure 9 shows the linearity of the reaction curves of the PVA/GOx electrospun membranes modified by graphene. The specific enzyme activity was calculated by the Beer-Lambert law. The enzyme activity of the immobilized enzymes in the electrospun nanofibrous membrane without graphene addition was 0.56±0.12 U/mg, whereas for the PVA/GOx sample

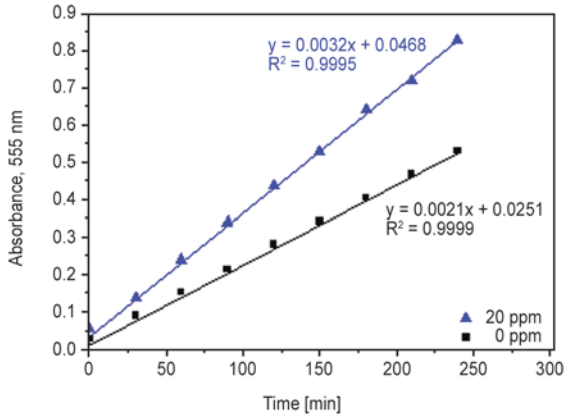

Figure 9. The linearity of the reaction curves of samples

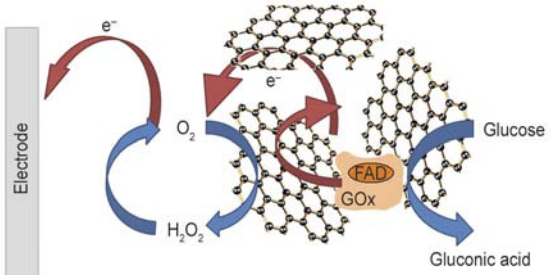

Figure 10. Schematic illustration reveals the interaction between graphene and enzyme

with 20 ppm of graphene it was 0.93±0.31 U/mg, i.e. a 66% increase compared to the sample without graphene. This result indicated graphene may stabilize the enzyme's conformation and hence increase its survivability. Graphene may also facilitate the catalytic reaction because of its high surface area and surface energy. Nanomaterials like graphene with good electrical properties display high affinity for immobilized enzymes, due to their ability to improve the transfer of electrons between the active redox center of the enzyme and O_2 in the bulk solution during the redox process. Moreover, graphene may supply direct-electron-transferring channels from the active center of GOx to O_2, such effects accelerate the regeneration of GOx and thus increase the relative activity of the enzymes. A schematic illustration (Figure 10) reveals the interaction between graphene and enzyme within PVA/GOx electrospun nanofibrous membranes.

5. Conclusions

In this study, graphene modified PVA/GOx electrospun membranes were prepared to examine the immobilization mechanism between graphene and GOx. TEM images revealed that graphene nanoplates were dispersed within the nanofibers. The electrochemical measurement results show that the sensitivities increased with increasing graphene concentrations up to 20 ppm. The highest sensitivity recorded 38.7 μA/mM was for a PVA/GOx membrane with 20 ppm graphene representing a 109% increase over a membrane made without graphene. The K_m^{app} for the 20 ppm graphene content membrane was 1.1 mM, which was much lower than the membrane without grapheme (13.2 mM). The lower K_m^{app} value was attributed to the facilitation of the catalytic reaction between GOx and glucose and the higher biological affinity between the immobilized enzyme and glucose. The activities of the immobilized enzyme in the PVA/GOx membrane with and without graphene added were 0.93 and 0.56 U/mg, respectively. These results indicate that the presence of graphene contributes to the maintenance of the enzyme's conformational stability which in turn facilitates the catalytic reaction while extending its working lifespan.

Acknowledgements

Part of this work is financially supported from the National Science Council of Taiwan, ROC, under contract numbers: NSC 101-2221-E-035-013 and NSC 102-2221-E-011 -160.

References

[1] Wang J.: Electrochemical glucose biosensors. Chemical Reviews, **108**, 814–825 (2008). DOI: 10.1021/cr068123a

[2] Kandimalla V. B., Tripathi V. S., Ju H.: Biosensors based on immobilization of biomolecules in sol-gel matrices. in 'Electrochemical sensors, biosensors and their biomedical applications'. Academic Press, San Diego, 503–529 (2008). DOI: 10.1016/B978-012373738-0.50018-0

[3] Wong F-L., Abdul-Aziz A.: Comparative study of poly(vinyl alcohol)-based support materials for the immobilization of glucose oxidase. Journal of Chemical Technology and Biotechnology, **83**, 41–46 (2008). DOI: 10.1002/jctb.1774

[4] Xie J., Hsieh Y-L.: Ultra-high surface fibrous membranes from electrospinning of natural proteins: Casein and lipase enzyme. Journal of Materials Science, **38**, 2125–2133 (2003). DOI: 10.1023/A:1023763727747

[5] Manesh K. M., Kim H. T., Santhosh P., Gopalan A. I., Lee K-P.: A novel glucose biosensor based on immobilization of glucose oxidase into multiwall carbon nanotubes–polyelectrolyte-loaded electrospun nanofibrous membrane. Biosensors and Bioelectronics, **23**, 771–779 (2008). DOI: 10.1016/j.bios.2007.08.016

[6] Kang X., Wang J., Wu H., Aksay I. A., Liu J., Lin Y.: Glucose oxidase–graphene–chitosan modified electrode for direct electrochemistry and glucose sensing. Biosensors and Bioelectronics, **25**, 901–905 (2009). DOI: 10.1016/j.bios.2009.09.004

[7] Xu Z., Chen X., Dong S.: Electrochemical biosensors based on advanced bioimmobilization matrices. Trends in Analytical Chemistry, **25**, 899–908 (2006). DOI: 10.1016/j.trac.2006.04.008

[8] Wang N., Burugapalli K., Song W., Halls J., Moussy F., Ray A., Zheng Y.: Electrospun fibro-porous polyurethane coatings for implantable glucose biosensors. Biomaterials, **34**, 888–901 (2013). DOI: 10.1016/j.biomaterials.2012.10.049

[9] Djennad M., Benachour D., Berger H., Schomäcker R.: Poly(vinyl alcohol) ultrafiltration membranes: Synthesis, characterization, the use for enzyme immobilization. Engineering in Life Sciences, **3**, 446–452 (2003). DOI: 10.1002/elsc.200301849

[10] Tang C., Saquing C. D., Harding J. R., Khan S. A.: *In situ* cross-linking of electrospun poly(vinyl alcohol) nanofibers. Macromolecules, **43**, 630–637 (2010). DOI: 10.1021/ma902269p

[11] Hassan C. M., Peppas N. A.: Structure and applications of poly(vinyl alcohol) hydrogels produced by conventional crosslinking or by freezing/thawing methods. Advances in Polymer Science, **153**, 37–65 (2000). DOI: 10.1007/3-540-46414-X_2

[12] Doretti L., Ferrara D., Gattolin P., Lora S., Schiavon F., Veronese F. M.: PEG-modified glucose oxidase immobilized on a PVA cryogel membrane for amperometric biosensor applications. Talanta, **45**, 89–-898 (1998). DOI: 10.1016/S0039-9140(97)00191-4

[13] Wang Z-G., Wan L-S., Liu Z-M., Huang X-J., Xu Z-K.: Enzyme immobilization on electrospun polymer nanofibers: An overview. Journal of Molecular Catalysis B: Enzymatic, **56**, 189–195 (2009). DOI: 10.1016/j.molcatb.2008.05.005

[14] Li Y., Quan J., Branford-White C., Williams G. R., Wu J-X., Zhu L-M.: Electrospun polyacrylonitrile-glycopolymer nanofibrous membranes for enzyme immobilization. Journal of Molecular Catalysis B: Enzymatic, **76**, 15–22 (2012). DOI: 10.1016/j.molcatb.2011.12.003

[15] Ge L., Zhao Y-S., Mo T., Li J-R., Li P.: Immobilization of glucose oxidase in electrospun nanofibrous membranes for food preservation. Food Control, **26**, 188–193 (2012). DOI: 10.1016/j.foodcont.2012.01.022

[16] Ren G., Xu X., Liu Q., Cheng J., Yuan X., Wu L., Wan Y.: Electrospun poly(vinyl alcohol)/glucose oxidase biocomposite membranes for biosensor applications. Reactive and Functional Polymers, **66**, 1559–1564 (2006). DOI: 10.1016/j.reactfunctpolym.2006.05.005

[17] Su X., Wei J., Ren X., Li L., Meng X., Ren J., Tang F.: A new amperometric glucose biosensor based on one-step electrospun poly(vinyl alcohol)/chitosan nanofibers. Journal of Biomedical Nanotechnology, **9**, 1776–1783 (2013). DOI: 10.1166/jbn.2013.1671

[18] Wan L-S., Ke B-B., Xu Z-K.: Electrospun nanofibrous membranes filled with carbon nanotubes for redox enzyme immobilization. Enzyme and Microbial Technology, **42**, 332–339 (2008). DOI: 10.1016/j.enzmictec.2007.10.014

[19] Lan D., Li B., Zhang Z.: Chemiluminescence flow biosensor for glucose based on gold nanoparticle-enhanced activities of glucose oxidase and horseradish peroxidase. Biosensors and Bioelectronics, **24**, 934–938 (2008). DOI: 10.1016/j.bios.2008.07.064

[20] Marx S., Jose M. V., Andersen J. D., Russell A. J.: Electrospun gold nanofiber electrodes for biosensors. Biosensors and Bioelectronics, **26**, 2981–2986 (2011). DOI: 10.1016/j.bios.2010.11.050

[21] Rahman Md. M., Ahammad A. J. S., Jin J-H., Ahn S. J., Lee J-J.: A comprehensive review of glucose biosensors based on nanostructured metal-oxides. Sensors, **10**, 4855–4886 (2010). DOI: 10.3390/s100504855

[22] Jang H. D., Kim S. K., Chang H., Roh K-M., Choi J-W., Huang J.: A glucose biosensor based on TiO_2–Graphene composite. Biosensors and Bioelectronics, **38**, 184–188 (2012). DOI: 10.1016/j.bios.2012.05.033

[23] Shao Y., Wang J., Wu H., Liu J., Aksay I. A., Lin Y.: Graphene based electrochemical sensors and biosensors: A review. Electroanalysis, **22**, 1027–1036 (2010). DOI: 10.1002/elan.200900571

[24] Kuila T., Bose S., Khanra P., Mishra A. K., Kim N. H., Lee J. H.: Recent advances in graphene-based biosensors. Biosensors and Bioelectronics, **26**, 4637–4648 (2011). DOI: 10.1016/j.bios.2011.05.039

[25] Shan C., Yang H., Song J., Han D., Ivaska A., Niu L.: Direct electrochemistry of glucose oxidase and biosensing for glucose based on graphene. Analytical Chemistry, **81**, 2378–2382 (2009). DOI: 10.1021/ac802193c

[26] Shan C., Yang H., Han D., Zhang Q., Ivaska A., Niu L.: Graphene/AuNPs/chitosan nanocomposites film for glucose biosensing. Biosensors and Bioelectronics, **25**, 1070–1074 (2010). DOI: 10.1016/j.bios.2009.09.024

[27] Su X., Ren J., Meng X., Ren X., Tang F.: A novel platform for enhanced biosensing based on the synergy effects of electrospun polymer nanofibers and graphene oxide. Analyst, **138**, 1459–1466 (2013). DOI: 10.1039/c2an36663k

[28] Song Y., Qu K., Zhao C., Ren J., Qu X.: Graphene oxide: Intrinsic peroxidase catalytic activity and its application to glucose detection. Advanced Materials, **22**, 2206–2210 (2010).
DOI: 10.1002/adma.200903783

[29] Razmi H., Mohammad-Rezaei R.: Graphene quantum dots as a new substrate for immobilization and direct electrochemistry of glucose oxidase: Application to sensitive glucose determination. Biosensors and Bioelectronics, **41**, 498–504 (2013).
DOI: 10.1016/j.bios.2012.09.009

[30] Unnikrishnan B., Palanisamy S., Chen S-M.: A simple electrochemical approach to fabricate a glucose biosensor based on graphene–glucose oxidase biocomposite. Biosensors and Bioelectronics, **39**, 70–75 (2013).
DOI: 10.1016/j.bios.2012.06.045

[31] Wang Z., Zhou X., Zhang J., Boey F., Zhang H.: Direct electrochemical reduction of single-layer graphene oxide and subsequent functionalization with glucose oxidase. Journal of Physical Chemistry C, **113**, 14071–14075 (2009).
DOI: 10.1021/jp906348x

[32] Hsu Y-W., Hsu T-K., Sun C-L., Nien Y-T., Pu N-W., Ger M-D.: Synthesis of CuO/graphene nanocomposites for nonenzymatic electrochemical glucose biosensor applications. Electrochimica Acta, **82**, 152–157 (2012).
DOI: 10.1016/j.electacta.2012.03.094

[33] Lin S-L., Wu C-M., Chiou H-G., Weng Y-C.: Electrospun PVA/GOx biocomposite membranes for biosensor applications. in 'The 2nd International Conference on Nanomechanics and Nanocomposites, Beijing, China Beijin, China' p5 (2010).

[34] Wu C. M., Lin S. L., Chiou H. G., Weng Y. C., Ho C. Y., Huang W. H.: Gold nanoparticle modified PVA/GOx biocomposite membranes via electrospun for biosensor applications. in '18th International Conference on Composite Materials, Jeju, Korea' p6 (2011).

eXPRESS Polymer Letters Vol.8, No.8 (2014) 574–587
Available online at www.expresspolymlett.com
DOI: 10.3144/expresspolymlett.2014.61

Novel epoxy-benzoxazine water-based emulsions with reactive benzoxazine surfactants for coatings

*R. Ambrožič, U. Šebenik, M. Krajnc**

University of Ljubljana, Faculty of Chemistry and Chemical Technology, Aškerčeva cesta 5, 1000 Ljubljana, Slovenia

Received 2 March 2014; accepted in revised form 18 April 2014

Abstract. Novel epoxy-benzoxazine emulsions designed for water-based coatings were prepared and investigated. Bisphenol A-based epoxy resins with molar weights of 340, 377 and 1750 g/mol along with epoxidized soybean oil were emulsified using mono- and bi-functional benzoxazine surfactants, which are able to react with epoxy resins at their cure temperature. The structure of synthesized surfactants carrying one or two polyether chains was confirmed using Fourier transform infrared spectroscopy, ^{1}H nuclear magnetic resonance and differential scanning calorimetry. Stability of emulsions was verified by particle diameters measurements. Coatings, made directly from emulsions, were dried and cured at elevated temperature using 3,3′-dimetoxybenzidine as curing agent to ensure a highly cross-linked structure of thermosetting films. Curing process, thermal properties and hardness of cured films were investigated. It was found that benzoxazine molecules were well incorporated into the epoxy network upon curing, which ensures no void structure of cured copolymer and enhanced coating properties.

Keywords: *thermosetting resins, epoxy resins, benzoxazine, emulsions, coatings*

1. Introduction

Benzoxazine resins are a novel class of thermosetting phenolic resins, which can be synthesized from raw materials, such as phenols, formaldehyde and primary amines. Holly and Cope [1] were the first who reported the synthesis of benzoxazine in 1944. The polymerization and curing process of a benzoxazine compound is subjected to thermally accelerated, cationic ring-opening polymerization with or without an added initiator [2]. Benzoxazine polymerization is autocatalyzed as the newly produced phenolic structure, generated with ring opening mechanism, acts as an initiator and catalyst [2–5]. No by-products are formed during the curing process, resulting in no void in the final structure. Polybenzoxazines have excellent mechanical properties such as high modulus, high strength and high glass transition temperature (T_g), which is usually higher than their curing temperature. This, in combination with other advantages, such as high char yield, storage stability of the resins at room temperature, low heat release, near-zero shrinkage during curing, superior FST (fire, smoke, toxicity) properties and low water uptake, make polybenzoxazines very promising materials for future applications [2, 4–7]. Moreover, the versatile chemistry of benzoxazines offers the possibility of designing benzoxazine molecules with novel and/or specific properties, which give applicative functions. Designed properties of benzoxazine molecules may be achieved by a proper selection of phenol and amine compounds for the synthesis.

The polymerization and curing temperature of benzoxazine resins, which usually take place in temperature range between 140 and 220°C, may be higher than desirable for some industrial applications.

*Corresponding author, e-mail: matjaz.krajnc@fkkt.uni-lj.si

Their low cross-linking density, which is surprisingly low considering their high stiffness and T_g compared with other thermosets, is an additional problem. The main reason for high stiffness is the presence of strong H-bonds between polybenzoxazine molecules. Therefore, to further improve material properties a number of studies are directed toward reducing the curing temperature of benzoxazine, finding new low-temperature curing catalysts and increasing the cross-linking density of polybenzoxazine material [3, 5, 6, 8, 9].

A promising way to achieve a higher cross-linking density is the incorporation of epoxy resins into the benzoxazine matrix [8, 10, 11], because the ring-opening polymerization of a benzoxazine produces phenolic groups, which can react with epoxy compounds. Unfortunately, also copolymerization of benzoxazines with epoxy resins takes place at elevated temperatures [8, 10–18]. However, combining epoxy and benzoxazine resins seems a very perspective approach to design thermosets of enhanced properties, since also epoxy resins possess some excellent properties, such as good chemical resistance to solvents and good adhesion to many substrates [8, 11, 18, 19]. One of promising applications may be an epoxy-benzoxazine coating for different substrates. Due to environmental and economic concerns water-based emulsions to organic solvent-based polymer solutions are preferred in coating industries. The main drawback of an emulsion coating system is the presence of a non-polymerizable surfactant in its formulation, which reduces coating's cross-linking density, film hardness and weakens its corrosion protection function. By applying a benzoxazine molecule, which acts as reactive surfactant in an epoxy water-based emulsion, this problem could be overcome. Moreover, such approach may offer the possibility of preparing novel blends from epoxy resins and to them incompatible polymers in emulsions, where benzoxazine surfactant would acts as compatibilizer as well. Sawaryn *et al*. [20, 21] have already designed benzoxazine surfactants. They confirmed that benzoxazine surfactants could stabilize benzoxazine miniemulsions.

The aim of the work presented in this article was to apply reactive benzoxazine surfactants in epoxy emulsions. The surfactants should be able to stabilize oil in water (o/w) epoxy emulsions and should be capable of crosslinking with epoxy resins and therefore become part of cured epoxy-benzoxazine copolymer network. Water-based epoxy-benzoxazine emulsions were prepared using two benzoxazine surfactants and different epoxy resins. Thin epoxy-benzoxazine films were prepared directly from emulsions to investigate, if benzoxazine surfactant could be properly incorporated into the epoxy structure after drying, film formation and curing process, which is of great importance for possible industrial applications. Thermal properties and hardness of cured films were investigated as well.

2. Experimental

2.1. Materials

Paraformaldehyde (≥95.0%), 3,3′-dimetoxybenzidine (*o*-dianisidine), sodium hydroxide and anhydrous sodium sulfate (≥99.0%) were purchased from Sigma Aldrich, Chemie GmbH, Steinheim, Germany. Synthetic epoxy resins of bisphenol A diglycidyl ether type with different molar weights were purchased from Sigma Aldrich Co., St. Louis, MO, USA. The epoxy resins with molar weights 340, 377 and 1750 g/mol, are further referred to as Epoxy 340, Epoxy 377 and Epoxy 1750, respectively. As a bio-renewable resin, epoxidized soybean oil (Drapex 39, Galata Chemicals, Southbury, CT, USA) with 6.5% epoxy oxygen content and epoxide equivalent weight 246 g/eq, was used. Phenolic components, bisphenol A (≥98.0%) and 4-*tert*-butylphenol (≥98.0%), along with chloroform (≥99.0%) and dichloromethane (≥99.0%) were used as received from Merck KGaA, Darmstadt, Germany. Polyether monoamine (Jeffamine M-1000, molar weight 1000 g/mol) and N-phenyl bisphenol A based 1,3-benzoxazine (Araldite MT 35600 CH, BA-a benzoxazine) were received from Huntsman Holland BV, Rozenburg, Holland and Huntsman Advance Materials BVBA, Everberg, Belgium, respectively. Chemical structures of epoxy, benzoxazine and amine materials used are depicted in Figure 1.

2.2. Synthesis of benzoxazine surfactants

Benzoxazine surfactants were synthesized from Jeffamine M-1000, phenol component (bisphenol A or 4-*tert*-butylphenol) and paraformaldehyde. Chloroform was used as a solvent for all syntheses.

Synthesis of 4-tert-butylphenol-based surfactant

The 4-*tert*-butylphenol-based benzoxazine surfactant (Figure 2a) was synthesized according to

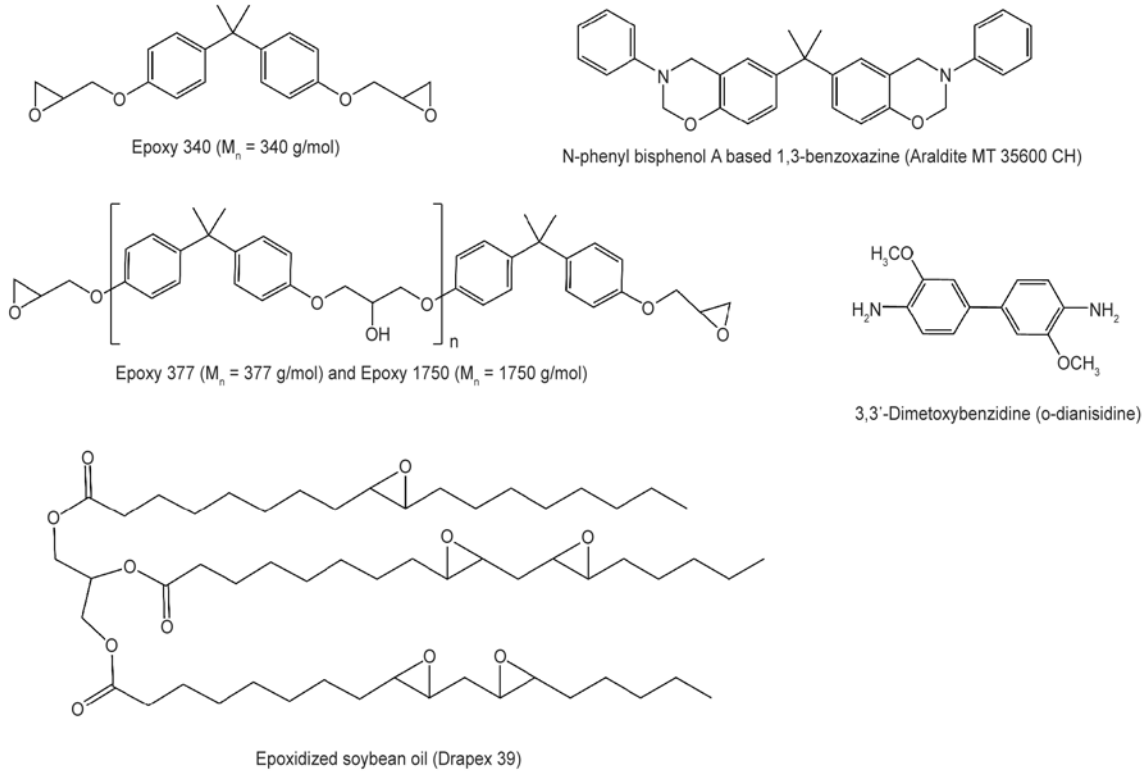

Figure 1. Chemical structures of epoxy and benzoxazine resins as well as amine curing agent used in this study

Chernykh *et al.* [22]. Jeffamine M-1000 (50.0 g, 0.05 mol) and paraformaldehyde (3.003 g, 0.1 mol) were stirred in a round-bottomed flask in 80 mL of chloroform at room temperature for 30 minutes, and then 4-*tert*-butylphenol (7.511 g, 0.05 mol) was added. The reaction mixture was refluxed for 24 h in a flask equipped with a condenser. The reaction was followed by thin layer chromatography (TLC). A yellow viscous liquid solution was obtained. The solution was washed three times with 1M NaOH aqueous solution and finally several times with distilled water, until neutral pH value. The organic phase was dried with anhydrous Na_2SO_4 and the solvent was removed at low pressure. A yellowish solid was obtained (yield ~85%). This benzoxazine surfactant is further referred to as Boxsurf 1.

Synthesis of bisphenol A-based surfactant

Bisphenol A-based benzoxazine surfactant (Figure 2b) was prepared by analogy to the procedure described above for the synthesis of 4-*tert*-butylphenol-based benzoxazine surfactant. Because of the bi-functionality of bisphenol A, the molar ratio of phenol, paraformaldehyde and Jeffamine M-1000

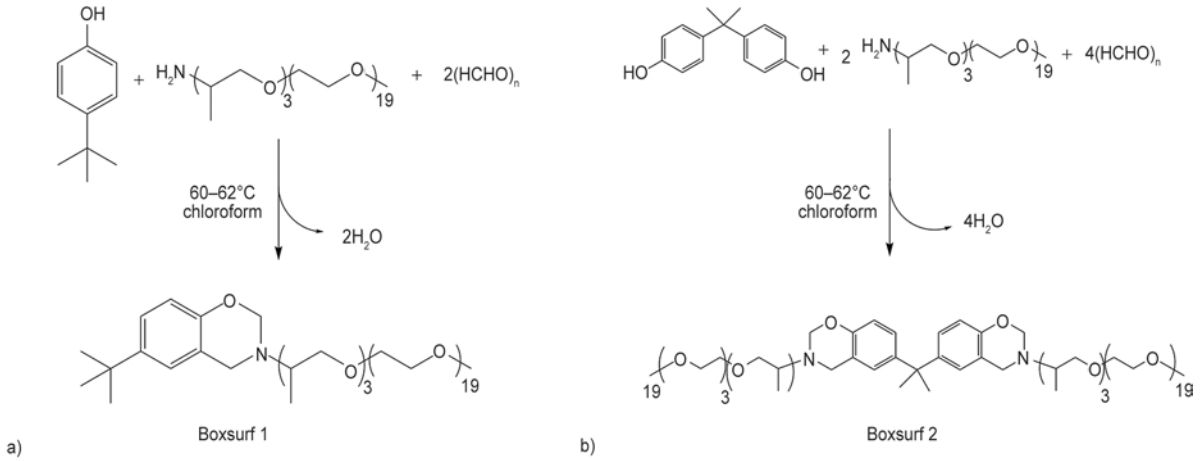

Figure 2. Synthesis of benzoxazine surfactants from Jeffamine M-1000, paraformaldehyde and phenolic compounds (4-*tert*-butyl phenol for synthesis of Boxsurf 1 (a) and bisphenol A for synthesis of Boxsurf 2 (b))

was changed from 1:2:1 to 1:4:2. A yellowish solid was obtained (yield~90%). This benzoxazine surfactant is further referred to as Boxsurf 2.

The formation of both benzoxazine surfactants was confirmed by Fourier transform infrared spectroscopy (FT-IR) using KBr disks on Perkin Elmer Spectrum 1000 spectrometer (Waltham, USA) and by ^{1}H nuclear magnetic resonance (NMR) analysis on Bruker Avance III 500 MHz NMR spectrometer (Billerica, USA). By FT-IR analysis also polymerization of benzoxazines at three different temperatures (150, 180 and 210°C) was investigated.

2.3. Preparation of epoxy emulsions with benzoxazine surfactants

A chosen amount of benzoxazine surfactant was solubilized in 6.5 g of water (continuous phase) and heated to 60°C. The pure epoxy resins (dispersed phase) were heated to 60°C as well. Elevated temperature was necessary to ensure lower viscosity of the dispersed phase. The continuous and dispersed phases were mixed together at elevated temperature (60°C) using a vortex stirrer (Ultra-Turrax IKA T25, Staufen, Germany) at 8400 rpm for 1 h. Weight ratio between water and dry matter (epoxy and benzoxazine) was constant for all experiments, namely 1:1. Emulsions prepared by this procedure were slowly cooled to room temperature. Average particle sizes and distributions of so prepared emulsions were determined using Microtrac Bluewave, FLEX 10.6.2 (Meerbusch, Germany) instrument. *O*-dianisidine (0.65 g), which was used as a curing agent for the curing process of epoxy-benzoxazine system, was dissolved in a small amount of dichloromethane. The solution of dichloromethane and curing agent was mixed with pre-prepared emulsions at room temperature. This ensures no polymerization or curing process of epoxy resins during emulsification.

2.4. Preparation of epoxy-polybenzoxazine thin films

Epoxy-polybenzoxazine thin films were made directly from aqueous emulsions containing the curing agent. Approximately 5 g of the emulsion was transferred to a glass plate by a four sided applicator frame (Zehntner ZAF 2010, Sissach, Switzerland) and 120 μm thick films were made. Three films for emulsion formulation were made. Films were dried and cured according to the temperature program shown in Figure 3 in a programmable thermostatic oven (APT. line™ FP, Binder, Tuttlingen, Germany). The long residence time at 210°C, recommended also by group of Grishchuk [14, 15, 18], was selected based on FT-IR analysis to achieve complete curing of both epoxy and benzoxazine resins. Transparent brownish epoxy-polybenzoxazine thin films were obtained after curing.

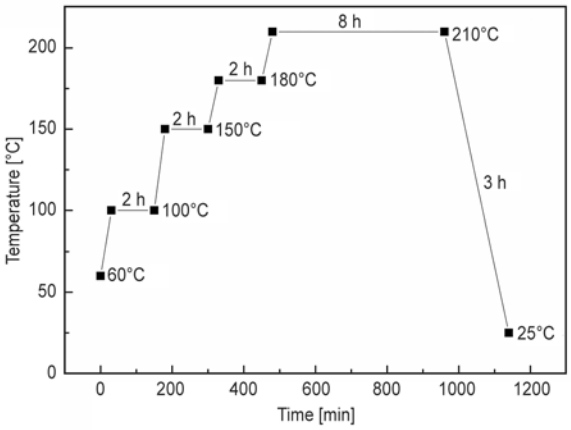

Figure 3. Cure cycle of epoxy-benzoxazine thermosetting copolymers

2.5. Curing and thermal properties of epoxy-polybenzoxazine thin films

Curing behavior of each resin was studied using differential scanning calorimetry (DSC, DSC 1, Mettler Toledo, Greifensee, Switzerland). Before DSC measurements the water from emulsions was evaporated at 50°C and under low pressure. Curing agent was added after drying to prevent curing during drying. Then 5–8 mg of samples were sealed in an aluminum pan with a lid. The purge nitrogen gas flow was maintained to be constant at 30 mL/min. The samples were heated from –100 to 300°C using 10°C/min heating rate. Two heating runs for each sample were performed. From DSC results also T_g of non-cured and cured epoxy-polybenzoxazine films could be determined.

2.6. Hardness measurement

Pendulum hardness

A König pendulum hardness tester (BYK pendulum hardness tester, Wesel, Germany) was used to measure the surface hardness of the cured films. The pendulum hardness is determined by measuring oscillation time of pendulum from 6 to 3° at room temperature. This test is based on the principle that the

harder the measured surface, the greater the amplitude time of pendulum oscillation (ASTM D 4366). The glass plate was used as a reference sample.

Pencil hardness

A Pencil hardness measurement is a relatively simple method to determine the hardness of coating films. The investigated film is placed on a firm horizontal surface and the pencil is held firmly against the film at 45° angle and pushed away from the operator in a 6.5 mm stroke. The minimum hardness able to scratch the surface of the cured film was determined by this method with BYK 5800 pencil hardness tester (Wesel, Germany) (ASTM D 3363-74, 2000) [23].

3. Results and discussion

Both synthesized benzoxazine surfactants consist of a hydrophobic head group with benzoxazine unit and a hydrophilic polyether tail. The long polyether chain consists of hydrophilic poly(ethylene oxide), PEO and hydrophobic poly(propylene oxide), PPO. Jeffamine M-1000 used in this study contains 19 PEO units and only 3 PPO units. The theoretical values for the hydrophobic-lipophilic balance, HLB, according to Griffin [24] were calculated from the different molar weight of hydrophobic and hydrophilic units of molecule of surfactants. HLB values for both surfactants were 14, which indicate a predominantly hydrophilic character of synthesized surfactants and potential ability for stabilization of o/w emulsions [20, 21].

3.1. Characterization of benzoxazine surfactants

The chemical structure of benzoxazine surfactants was confirmed by FT-IR and ^{1}H NMR spectroscopy. As representative example the FT-IR spectrum of Boxsurf 2 is shown in Figure 4, where the characteristic signal for oxazine ring, which corresponds to the asymmetric stretching vibration of C–O–C group, can be observed at around 1250 cm^{-1}. The formation of the tri-substituted aromatic ring was confirmed by typical signals at around 1503 and 952 cm^{-1}, while the strongest absorption band at 1105 cm^{-1} corresponds to C–O–C stretching vibration of polyether chain [20, 21].

Curing and polymerization of benzoxazine surfactants was investigated with FT-IR analyses as well. In Figure 4 the FT-IR spectra of Boxsurf 2 after its exposure to different elevated temperatures for 3 hours are shown. The diminishment or disappearance of signals at 1503 and 952 cm^{-1} confirmed benzoxazine curing. During curing, the peak at 1503 cm^{-1} disappears and shifts to around 1450 cm^{-1} because tri-substituted aromatic ring becomes tetra-substituted. Due to curing also the peak at 952 cm^{-1} disappears, as a result of oxazine ring-opening process. Results in Figure 4 clearly indicated that Boxsurf 2 should be cured for at least 3 hours or longer at 210°C to achieve a high degree of cure.

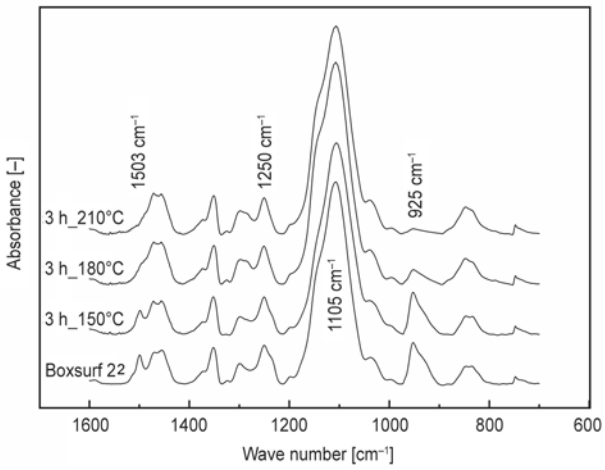

Figure 4. FT-IR spectra of Boxsurf 2 before and after 3 h of polymerization at 150, 180 and 210°C

The ^{1}H NMR spectroscopy (Figure 5) enabled determination of the amount of benzoxazine rings in benzoxazine surfactants. The amount of closed benzoxazine rings in Boxsurf 2 was calculated from the ratio between signals at 4.9 ppm (corresponding to oxazine –CH_2 group in –O–CH_2–N- group) and 1.6 ppm (corresponding to methyl groups of bisphenol A). It was found that 75% of Boxsurf 2 was bi-functional (had two benzoxazine units) and the rest was mono-functional. On the other hand, the amount of closed benzoxazine rings in Boxsurf 1, which was calculated from the ratio between signals at 4.9 and 1.3 ppm (corresponding to methyl group of *t*-butyl group), was 90%. Accordingly, the spectra of Boxsurf 1 and Boxsurf 2 also showed that some unreacted phenol (signals at 7.2 ppm) was still present. Other characteristic signals in ^{1}H NMR spectra were attributed to oxazine –CH_2 group in Ph–CH_2–N– group (at 4.0 ppm), to methylene groups of the polyether chain (from 3.3 to 3.7 ppm) and to aromatic rings (from 6.6 to 7.1 ppm) [20, 21]. The purity of Boxsurf 1 and Boxsurf 2, calculated from NMR data, was 91 and 72%, respectively.

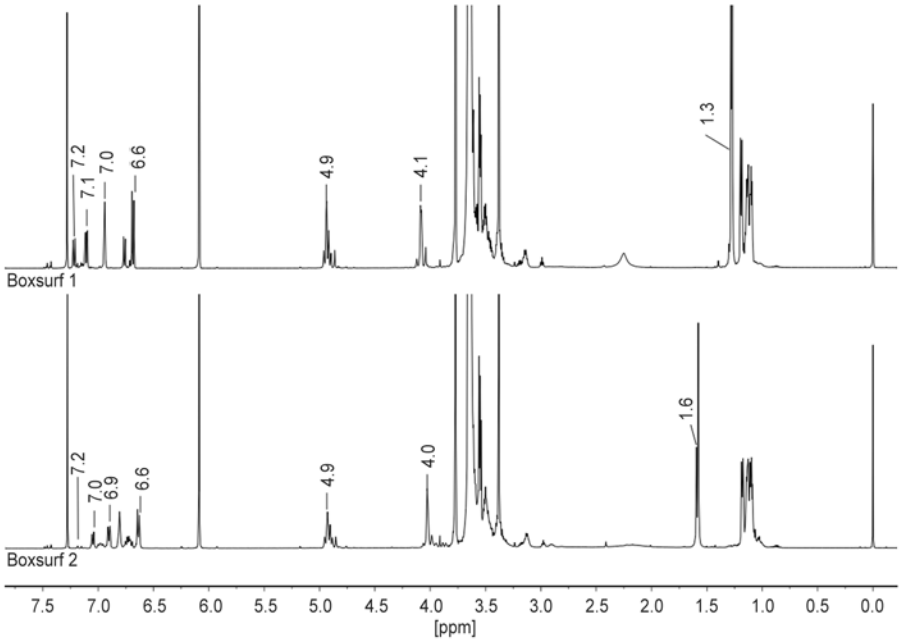

Figure 5. ^{1}H NMR spectra of Boxsurf 1 and Boxsurf 2 in $CDCl_3$

3.2. Formation and stability of epoxy emulsions

The aim of the next part of the research was to check if stable epoxy water-based emulsions could be obtained by using synthesized benzoxazines as surfactants. The emulsions were made following the procedure described in the experimental section. Different epoxy resins were chosen as dispersed phase. Effects of surfactant amount and molar weight of epoxy resins on the emulsion average particle size and distribution and emulsion stability were studied. Detailed compositions of investigated emulsions are collected in Table 1. High amount of surfactants were chosen, so epoxy-benzoxazine copolymerization process after emulsification, can be studied.

The viscosity of dispersed phase is one of the crucial criteria for the preparation of stable o/w emulsions, because a too big difference in viscosity between dispersed and continuous phases may leads to unstable emulsion system [20, 21, 25]. In the worst case emulsion cannot be obtained at all. Due to high viscosities of epoxy resins at room temperature and to prevent epoxy resin cooling during emulsification step, dispersed and continuous phase were first heated to 60°C. In experiments with Epoxy 1750 the temperature was still too low to ensure a sufficient reduction of viscosity and a solvent (dichloromethane) was added to the dispersed phase to further reduce the viscosity of the system. However it was still impossible to obtain a stable emulsion with Epoxy 1750.

After emulsification, the emulsions were stored in covered test tubes at room temperature to determine their stability with time. It was observed that after 3–4 days almost all systems showed a tendency to settle. The extent of settling increased with decreasing concentration of Boxsurf 1 or Boxsurf 2. Emulsions with Boxsurf 1 showed slightly better stability compared to emulsions with Boxsurf 2, although the HLB value of surfactants was very similar. The hydrophobic part of the Boxsurf 2 molecule is entrapped between two hydrophilic tails (Figure 2), which may hinder hydrophobic interactions between emulsifier and epoxy resin in emulsions. On the other hand, the emulsion stability decreased with increasing molar weight of the epoxy resin applied mainly due to the increased particle size, which was a consequence of higher resin viscosity. However, when the covered test tubes containing samples, which had settled, were just lightly shaken by hand, emulsions easily became perfectly homogenous again. This is of great importance especially for application purposes. The only system, which was stable even after a few weeks of storage and did not show any signs of settling, was the system with Drapex 39. This is due to low density of epoxidized soybean oil (0.99 g/mL at 25°C). The density of synthetic epoxy resins was 1.16 g/mL at 25°C.

Table 1 summarizes results of number average particle size (d_{num}) and particle size distribution measurements for emulsions with different epoxy resins and concentrations of benzoxazine surfactants. It

Table 1. Number average particle diameters (d_{num}) and polydispersity indexes (d_{vol}/d_{num}) for emulsions measured immediately after emulsification and after one week of storage. Mass of water was the same for all emulsions (6.5 g).

Emulsion	Epoxy resin amount	Surfactant amount		Average particle size and distribution			
				Immediately		*After 1 week	
				d_{num}	d_{vol}/d_{num}	d_{num}	d_{vol}/d_{num}
	[g]	[g]	[g/L]	[μm]	[–]	[μm]	[–]
Epoxy 340/Boxsurf 2							
E.1	5.69	0.81	125	0.80	10.7	0.91	11.3
E.2	5.57	0.93	143	0.87	10.0	0.84	11.1
E.3	5.41	1.09	168	0.87	9.4	0.97	9.8
E.4	5.20	1.30	200	0.89	5.9	0.96	8.1
E.5	4.88	1.62	249	0.97	4.2	1.30	5.3
E.6	4.34	2.16	332	1.09	3.2	1.55	3.7
Epoxy 340/Boxsurf 1							
E.7	5.41	1.09	168	0.85	7.5	0.91	8.7
E.8	5.20	1.30	200	0.85	6.9	1.20	5.0
E.9	4.88	1.62	249	0.93	3.6	1.41	3.1
Epoxy 377/Boxsurf 2							
E.10	5.41	1.09	168	0.72	10.9	0.86	11.1
E.11	5.20	1.30	200	0.78	7.1	0.87	8.0
E.12	4.88	1.62	249	0.91	4.1	1.00	4.4
Epoxy 1750/Boxsurf 2							
E.13	5.41	1.09	168	not stable			
E.14	5.20	1.30	200	not stable			
E.15	4.88	1.62	249	not stable			
Drapex 39/Boxsurf 2							
E.16	5.41	1.09	168	0.82	3.0	0.77	4.4
E.17	5.20	1.30	200	0.64	3.4	0.64	3.8
E.18	4.88	1.62	249	0.83	2.7	0.77	3.7

*Emulsions were shaken only by hand prior to measurements

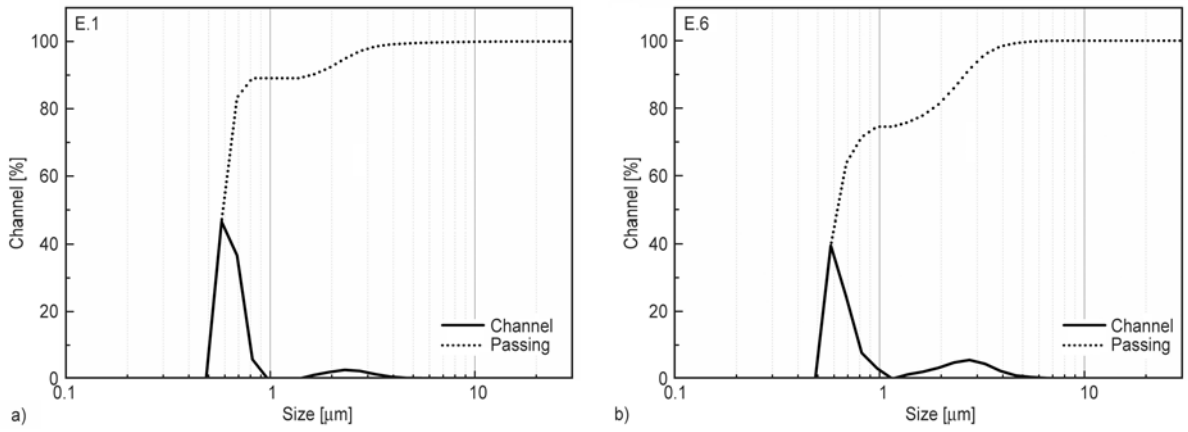

Figure 6. Number particle size distribution for emulsion E.1 (a) (12.5% Boxsurf 2 and 87.5% Epoxy 340) and emulsion E.6 (b) (33.3% Boxsurf 2 and 66.7% Epoxy 340) determined immediately after emulsification

may be seen in Table 1 that emulsions with the lowest average particle size were obtained for the emulsion containing epoxidized soybean oil, i.e. for the system with the lowest viscosity and density of the dispersed phase.

However, bimodal particle size distribution curves for emulsions were observed (Figure 6). The more intense peak, representing the diameter of a major number part of particles, appeared between 0.5 and 1 μm. The second peak was broader and appeared above 1 μm (with peak maximum between 2 and 3 μm). Interestingly the magnitude of the second peak increased with increasing surfactants amounts. Since surfactant should be in excess, the first peak most likely represented the size of epoxy particles, emulsified by the surfactant, while the second peak represented the size of clusters of unused surfactant. This was confirmed by particle size measure-

ment of pure surfactant emulsions, where a single peak with maximum at around 2.5 μm was observed. Therefore it may be concluded that molecules of the surfactant were in excess and effectively covered the surface of epoxy particles with diameter between 0.5 and 1 μm.

Pure surfactant particles are large due to the hydrophilic nature of polyether tails, which swell in water. The result of this phenomenon is the increasing number average particle size of emulsions with increasing benzoxazine concentration, which is not usual. For example, the number average particle size for emulsion Epoxy 340/Boxsurf 2, was increasing from 0.80 to 1.09 μm when concentration of benzoxazine surfactant increased from 125 to 332 g/L. Ratio between volume (d_{vol}) and number (d_{num}) average particle diameters (d_{vol}/d_{num}), as a measure for the polydispersity, decreased with increasing surfactant concentration for all emulsions, because dnum increased and dvol decreased with surfactant concentration. The dnum increase and simultaneous dvol decrease for such systems were observed elsewhere [20, 21, 25–27].

Since emulsions showed a tendency to settle after a few days, particle diameters were measured again after one week. Before measurements the test tubes containing emulsions were shaken (only by hand) to obtain homogeneous systems. The measured results are listed in Table 1 and are very similar to the results obtained immediately after emulsification. This suggested that emulsions were stable (they only settle, but not coagulate) and may be used for practical applications. The settling, which depended on the amount of surfactant used, was due to difference in density between dispersed and continuous phase. Over time the two peaks in distribution curves separated even more, indicating some surfactant redistribution between particles and confirming that two different kinds of particles did not coagulate. As a consequence also d_{vol}/d_{num} values increased just slightly with time.

3.3. Curing behavior of epoxy-benzoxazine films

Thermal properties of both surfactants were investigated by DSC analysis using two heating runs. Figures 7 and 8 show thermograms in higher and lower temperature region of interest, respectively. In DSC thermogram, obtained at heating rate 10°C/min, Boxsurf 1 showed an exothermic peak, which corresponded to curing, with onset (T_i) and maximum (T_p) at 230 and 262°C, respectively. Boxsurf 2 had T_i and T_p at 205 and 250°C, respectively. Boxsurf 1 released less heat (27.5 J/g) than Boxsurf 2 (32.2 J/g) during its curing process. Results in Figure 7 indicate that higher benzoxazine functionality of Boxsurf 2 shifted the onset temperature of the curing process to a lower temperature. However, the curing temperature intervals for both surfactants were very broad; the peaks in Figure 7 extended up to almost 300°C. We believe this was because of the steric hindrance of the curing process, which was induced by long polyether chains.

To estimate the effect of polyether chains on curing, N-phenyl bisphenol-A based 1,3-benzoxazine (BA-a benzoxazine), was scanned by the same DSC method (Figure 7). Results showed that considerably more heat were released during BA-a benzoxazine curing (300 J/g) and that the exothermic peak was not as broad as for benzoxazine surfactants. Similar results were obtained also by Ning and Ishida [28, 29]. The main reason for differences in reaction enthalpy is, without doubt, the chemical structure of benzoxazine surfactants, which contain long hydrophilic tails and have therefore less reactive oxazine groups per gram of material. The steric hindrance induced by long polyether tails prolonged the curing process to higher temperatures.

The catalytic effect of amine moieties on curing processes of benzoxazines was demonstrated and published by several authors [2, 10, 13–15]. *O*-dianisidine (10 wt%), with diamine structure, was used as

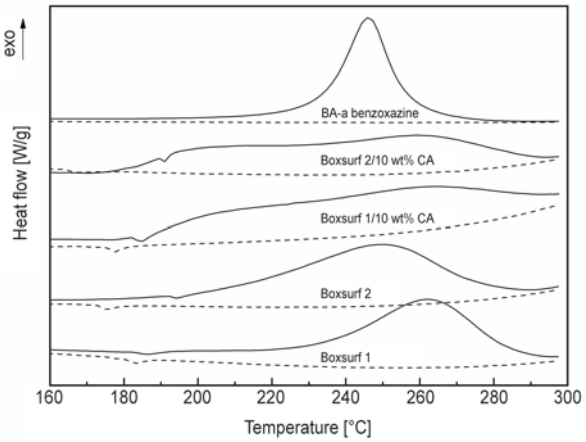

Figure 7. DSC thermograms of Boxsurf 1 and Boxsurf 2 with and without 10 wt% of curing agent and DSC thermograms of BA-a benzoxazine in the curing temperature range. Full lines represent first heating runs (material before cure) and dashed lines represent second heating runs (cured material).

curing agent to reduce the temperature of curing. Added curing agent had a positive effect on the curing process of both surfactants (Figure 7), since the onset temperature of curing was reduced. However, as a consequence of lowered curing onset temperature, even broader exothermic peaks were observed. This indicates that during the curing process different reactions take place [8, 14, 15, 17, 19]. Figure 7 also shows that benzoxazine surfactants were completely cured already after first DSC runs, since no exothermic peak was observed in DSC thermograms of second runs. To estimate the effect of added curing agent on degree of cure, isothermal curing of benzoxazine surfactants, with and without curing agent, was carried out at 180°C for 30 minutes. Then dynamic DSC thermograms were scanned and the degree of cure was calculated according to Equation (1):

$$\text{Degree of cure}\,[\%] = \left(1 - \frac{\Delta H_r}{\Delta H_0}\right)\cdot 100 \qquad (1)$$

where ΔH_r is the heat of reaction of the partially cured specimen and ΔH_0 is the heat of reaction of the uncured resin. Degree of cure after 30 minutes at 180°C increased with the addition of the curing agent (10 wt%) from 17.4 to 68.0% and from 39.3 to 72.3% for Boxsurf 1 and Boxsurf 2, respectively. Positive effect of curing agent addition was thus clearly seen in both cases, although broader curing peaks were observed in DSC thermograms (Figure 7) when *o*-dianisindine was added.

In DSC thermograms of Boxsurf 1 and Boxsurf 2 in the lower temperature region (Figure 8) an endothermic peaks due to a pronounced melting transition could be observed. The minimums of melting peaks of Boxsurf 1 and Boxsurf 2 were observed at 29 and 30°C, respectively. These melting transitions were observable also after curing, because polyether chains, which melted, were not involved in curing reactions. Added curing agent had no impact on melting.

Curing behavior of epoxy-benzoxazine films was investigated next. The aim of this investigation was to confirm if benzoxazine molecules are well incorporated in the epoxy structure upon emulsification, film formation and curing and to investigate how different molar weights of epoxy resin and different benzoxazine contents influence on film curing process. For curing 10 wt% of *o*-dianisidine as curing agent was used.

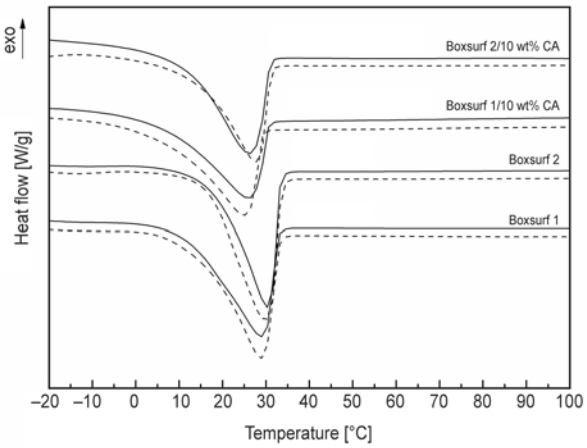

Figure 8. DSC thermograms of Boxsurf 1 and Boxsurf 2 with and without 10 wt% of curing agent in the polyether chains melting temperature range. Full lines represent first heating runs (material before cure) and dashed lines represent second heating runs (cured material).

Curing parameters of neat epoxy and neat benzoxazine resins, as well as curing parameters of their mixtures, are listed in Table 2. In accordance with the literature [14, 15, 30–32], epoxy resins, if a proper curing agent is used, usually polymerize at lower temperatures than benzoxazine resins, which is well observed by comparing Figures 7 and 9. The only exception was found for systems with Drapex 39, where no curing process was detected under these conditions. To achieve fully cross-linked structure of Drapex 39, the concentration of added curing agent should be higher (stoichiometric ratio) and the time of curing should be longer. We must be aware of the fact that epoxidized soybean oil is a large triglyceride molecule (Figure 1) with large steric barriers that

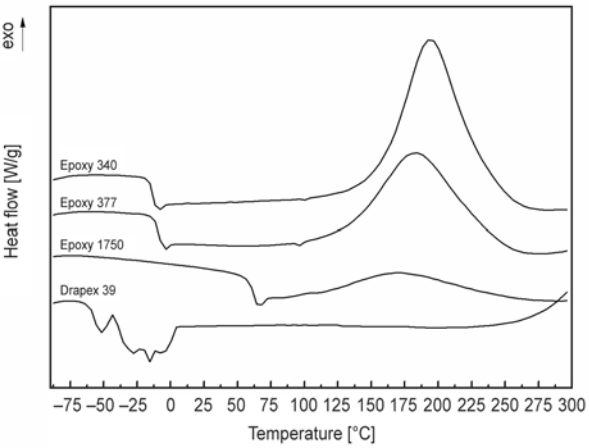

Figure 9. DSC thermograms of Epoxy 340, Epoxy 377, Epoxy 1750 and Drapex 39 with 10 wt% of *o*-dianisidine in the temperature range from –100 to 300°C with heating rate 10°C/min

Table 2. Curing parameters of epoxy-benzoxazine mixture with addition 10 wt% of curing agent

Film	Surfactant content [%]	Epoxy content [%]	Onset temperature (T_i) [°C]	Peak temperature (T_P) [°C]	Released heat (ΔH) [J/g]	T_g of uncured resin [°C]	T_g of cured resin [°C]
Epoxy 340/Boxsurf 2							
E.1	12.5	87.5	144	193	133	–20	65
E.2	14.3	85.7	149	193	126	–22	63
E.3	16. 7	83.3	151	194	123	–22	58
E.4	20.0	80.0	151	194	120	–25	48
E.5	25.0	75.0	154	195	115	–27	39
E.6	33.3	66.7	154	196	108	–32	27
Epoxy 340/Boxsurf 1							
E.7	16.7	83.3	154	195	164	–23	56
E.8	20.0	80.0	154	195	154	–25	48
E.9	25.0	75.0	157	198	128	–27	39
Epoxy 377/Boxsurf 2							
E.10	16.7	83.3	132	183	128	–16	57
E.11	20.0	80.0	130	185	101	–21	49
E.12	25.0	75.0	132	187	97	–22	40
Epoxy 1750/Boxsurf 2							
E.13	16.7	83.3	110	170	79	–	61
E.14	20.0	80.0	111	174	75	–	53
E.15	25.0	75.0	113	178	70	–	42
Drapex 39/Boxsurf 2							
E.16	16.7	83.3	–	–	–	–62	–51
E.17	20.0	80.0	232	275	15	–60	0
E.18	25.0	75.0	247	277	9	–62	–4
Pure compounds							
Epoxy 340	0.0	100.0	154	194	202	–14	66
Epoxy 377	0.0	100.0	96	183	146	–9	83
Epoxy 1750	0.0	100.0	70	172	53	60	107
Drapex 39	0.0	100.0	–	–	–	<–30*	<–30*
Boxsurf 1	100.0	0.0	194	213	26	–57	–35
Boxsurf 2	100.0	0.0	187	212	31	–55	–33

*No exact determination of T_g value is possible.

hinder chemical reactions. In addition, the concentration of epoxy groups per weight of the Drapex 39 molecules is significantly lower compared to synthetic epoxy resins [30].

The heat released during curing reactions (reaction enthalpy, ΔH) was determined from the area under the exothermic peak in DSC thermograms. Curing of epoxy resins is a more exothermic process than curing of benzoxazine surfactants. Therefore the value of ΔH decreased with increasing amount of benzoxazine in the mixture (Figure 10). ΔH value, on the other hand, increased with increasing concentration of epoxy groups in epoxy resin, which is confirmed by Figure 9 and results listed in Table 2, where it can be seen that Epoxy 340, which has the lowest molar weight, releases more heat during curing compared to other epoxy resins.

Some epoxy-benzoxazine combinations have two exothermic peaks in their thermograms (Figure 10),

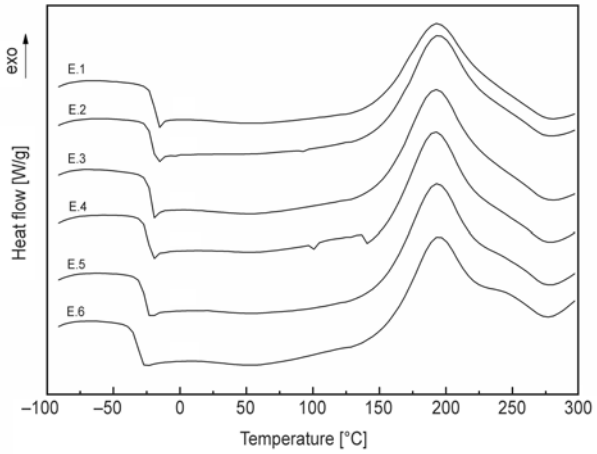

Figure 10. DSC thermograms for uncured system Epoxy 340/Boxsurf 2 in the range from –100 to 300°C with heating rate 10°C/min

which became more distinguishable with increasing benzoxazine content, because curing of an epoxy-benzoxazine system is a multiple step process including more than one reaction [8, 14, 15, 17, 19].

3.4. Thermal properties of uncured and cured films

Thin films were prepared directly from aqueous emulsions. Films could be made even for system Epoxy 1750/Boxsurf 2, although stable emulsions were not obtained. Glass transitions of uncured samples were well defined for all epoxy resins, both surfactants and their blends (films made form emulsions), except for neat Drapex 39, which had a multistep transition; most likely the glass transition (between –60 and –40°C) was followed by cold crystallization and melting (Figure 9). With increasing molar weight, T_g values of epoxy resins shifted toward higher temperature. The T_g values of uncured resins increased from –14 to 60°C when molar weight increased from 340 to 1750 g/mol, respectively. Uncured benzoxazine surfactants showed their glass transition at lower temperature than epoxy resins; T_g values of –57 and –55°C for Boxsurf 1 and Boxsurf 2 were determined, respectively. For uncured epoxy-benzoxazine films only one T_g was observed, which indicated that homogeneous blends of epoxy and benzoxazine at molecular level were obtained. The incorporation of benzoxazine in epoxy resins resulted in a decreased T_g value (Table 2) as expected. It has to be mentioned, that T_g for uncured Epoxy 1750/Boxsurf 2 film was not obtained because its T_g appears at higher temperature than onset curing (T_i). In such cases process of vitrification occurs. Due to vitrification signals looking as small endothermic peaks on DSC curves are often observed (Figures 9 and 10).

By comparing Figures 8 and 10 one may observe that combining benzoxazine surfactants with epoxy resins resulted in a complete disappearance of the benzoxazine melting peak (by DSC analysis of Jeffamine M-1000 it was confirmed, that this is the melting peak of polyether chain crystals). This observation supports the observation of a single T_g, indicates that benzoxazines were dissolved in epoxy resins to a certain level, and confirms that intermolecular interactions between epoxy and benzoxazine, which prevent crystallization of polyether chains, were formed. It may be assumed that H-bonds present in the epoxy-benzoxazine blend prevented orientation and arrangement of polyether chains into crystal structure. Intermolecular bonds in the epoxy-benzoxazine system have been demonstrated and studied by several authors [4, 15, 33, 34].

Therefore, from results obtained by DSC measurements it may be concluded that benzoxazine surfactant should be homogeneously incorporated in epoxy matrix and that secondary interactions between epoxy and benzoxazine compounds were established.

As expected, the glass transition temperatures of films increased significantly (Table 2, Figure 11) after curing process. Cured films with higher benzoxazine amounts had lower T_g values. For example, the T_g value for system Epoxy 340/Boxsurf 2, decreased from 65 to 27°C, when the amount of benzoxazine increased from 12.5 to 33.3%. Differences in T_g values of neat epoxy resins and neat benzoxazines are the main reason for such behavior, since cross-linking density of benzoxazine surfactants is probably much lower than that of epoxy resins. The highest T_g values were observed for cured systems containing epoxy resin of the highest molar weight (Epoxy 1750). The increase of cured system T_g value with molar mass of the uncured resin can be explained by non-stoichiometric amount of amine curing agent. In case of stoichiometric epoxy resins/curing agent ratios, lower cross-linking densities of cured epoxy resins with higher molar weight are expected because of the increase in the chain length between crosslinks. The lowest T_g values were observed for systems with Drapex 39, since these films were not properly cured. As explained before, the large steric hindrance and lower concentration of epoxy groups in Drapex 39 are the main reasons for such behavior.

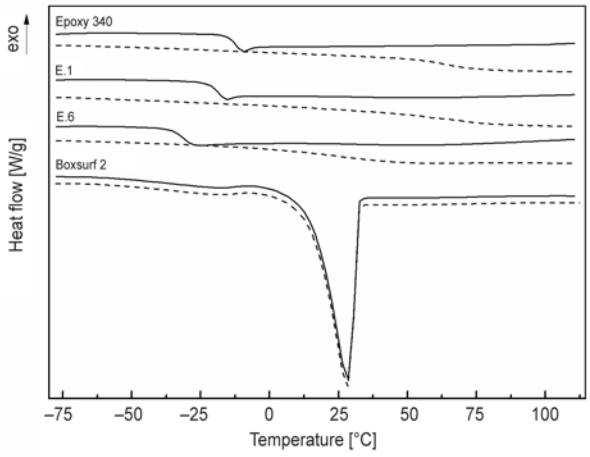

Figure 11. DSC thermograms of Epoxy 340, Boxsurf 2 and their mixtures E.1 (87.5% Epoxy 340 and 12.5% Boxsurf 2) and E.6 (66.7% Epoxy 340 and 33.3% Boxsurf 2). Full lines represent uncured films and dashed lines represent cured films.

3.5. Hardness of cured films

There are several methods used for measuring the surface hardness of a coating, which give complementary results. The pendulum hardness test (König) and the pencil hardness test were used in the present study.

Pendulum hardness of the cured materials was measured for 120 μm thick films (Figure 12a). The measured values for neat epoxy resins were much higher than those for neat benzoxazines. Therefore, pendulum hardness of cured epoxy-benzoxazine films decreased with increasing amount of benzoxazine and also with decreasing molar weight of epoxy resins, as predicted by T_g results. The results showed that cured epoxy-benzoxazine films with small amounts of benzoxazine surfactant had lower pendulum hardness but still comparable to that of the control glass plate, whose hardness was 250 s. Figure 12a also shows that slightly higher film hardness with Boxsurf 2 than Boxsurf 1 was obtained. Boxsurf 2 is a bi-functional molecule with two reactive sites, which probably contribute to higher crosslinking density of cured copolymer network and, consequently, the hardness of films was improved.

The results obtained by pencil hardness tests are shown in Figure 12b. The results were in good agreement with those obtained by pendulum hardness measurements: Pencil hardness of cured films increased with increasing amount and molar weight of epoxy resins. However, a maximum value of pencil hardness was observed for films containing around 80–90% of epoxy resins and 10–20% of benzoxazines, which indicated that a lower amount of benzoxazine surfactant even improved surface properties of cured films. The differences between detected tendencies of dependency of pendulum and pencil hardness from benzoxazine content might be sought in principles of hardness determination techniques; the pencil hardness reflects combination of modulus, tensile strength and adhesion properties, while the pendulum hardness depends mainly on the loss factor of investigated coating. Pencil hardness of films for Drapex 39/Boxsurf 2 film could not be determined, because its hardness was lower than that of the softest pencil, 9B.

To conclude, the results of hardness measurements were in excellent agreement with determined T_g values. This means that thermal properties and hardness of cured films improved with the increasing amount of epoxy resins, increasing functionality of benzoxazine surfactant and with increasing molar weight of epoxy resins.

4. Conclusions

Mono- and bi-functional benzoxazine nonionic surfactants were successfully synthesized and used as surfactants for water-based epoxy emulsions. All emulsions, except emulsions made with epoxidized soybean oil, settled after few days, but a homogeneous system was easily obtained again, only by light emulsion shaking in a covered test tube. Emulsions contained emulsified epoxy particles and larger clusters of benzoxazine surfactant, indicating that surfactant was in excess and that the molecules of the surfactant effectively covered the surface of epoxy particles. Slightly more stable emulsions with smaller particles were obtained with mono functional benzoxazine surfactant.

Different epoxy resins were used to investigate the impact of molar weight of epoxy resin on the formation and stability of emulsions. By decreasing the molar weight of synthetic epoxy resin the emulsion

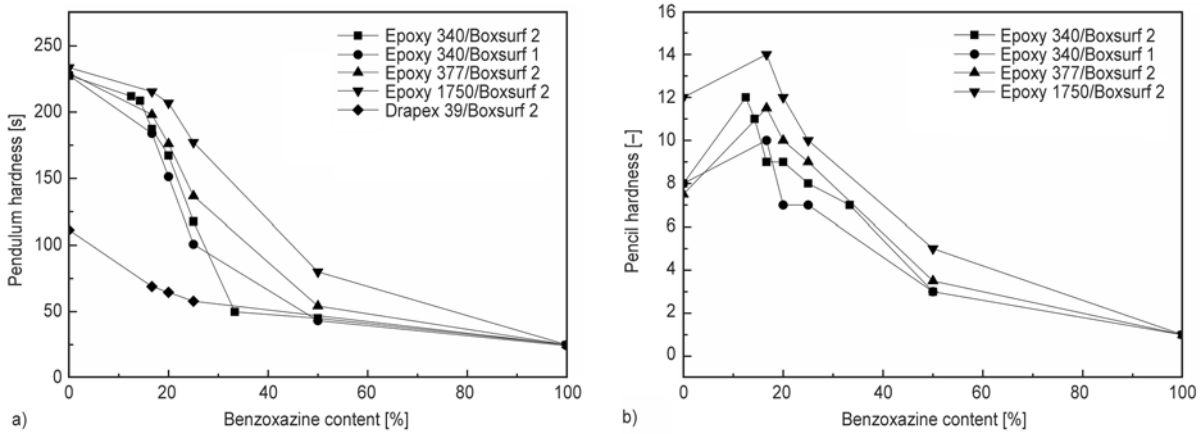

Figure 12. Pendulum hardness (a) and pencil hardness (b) of cured films as a function of benzoxazine content

stability was improved. It was found that emulsion with epoxidized soybean oil was the most stable and had the smallest average particle size, due to relatively low resin density and viscosity.

Thin films were successfully made directly from emulsions. They were dried and cured in a thermostatic oven at 210°C. Only one glass transition temperature was observed for films before and after curing, although neat benzoxazine and epoxy had considerably different glass transition temperatures. After curing, the benzoxazine melting point disappeared as well, meaning that epoxy-benzoxazine films were homogeneous at molecular level. T_g values of cured films were higher than those of uncured films. However, results indicate that T_g value of films, before and after curing, and consequently film hardness, decreased with increasing benzoxazine content, which was due to low T_g values of benzoxazine surfactants, containing polyether chains in the structure. T_g values were strongly affected by molar weight of epoxy resin as well.

On the basis of the obtained results, we can conclude that already small amounts (<12.5 wt%) of benzoxazine surfactant can stabilize water-based epoxy emulsions. The necessary amount of benzoxazine surfactant could be that low that the key film properties of neat epoxy resin, such as cross-linking density, glass transition temperature and hardness, are insignificantly affected. In the next step of the research the lowest concentration of benzoxazine surfactant, which still provides stable emulsions will be determined and the amount of curing agent will be optimized.

Acknowledgements

The financial support of this work by the Slovenian Ministry of Higher Education, Science and Technology (Grant P2-0191) is gratefully acknowledged. We kindly thank Dr. Branko Alič for ^{1}H NMR spectra analyses.

References

[1] Holly F. W., Cope A. C.: Condensation products of aldehydes and ketones with o-aminobenzyl alcohol and o-hydroxybenzylamine. Journal of the American Chemical Society, **66**, 1875–1879 (1944). DOI: 10.1021/ja01239a022

[2] Ishida H., Agag T.: Handbook of benzoxazine resins. Elsevier, Amsterdam (2011).

[3] Nair C. P. R.: Advances in addition-cure phenolic resins. Progress in Polymer Science, **29**, 401–498 (2004). DOI: 10.1016/j.progpolymsci.2004.01.004

[4] Ishida H., Allen D. J.: Physical and mechanical characterization of near-zero shrinkage polybenzoxazines. Journal of Polymer Science Part B: Polymer Physics, **34**, 1019–1030 (1996). DOI: 10.1002/(SICI)1099-0488(19960430)34:6<1019::AID-POLB1>3.0.CO;2-T

[5] Ghosh N. N., Kiskan B., Yagci Y.: Polybenzoxazines – New high performance thermosetting resins: Synthesis and properties. Progress in Polymer Science, **32**, 1344–1391 (2007). DOI: 10.1016/j.progpolymsci.2007.07.002

[6] Yagci Y., Kiskan B., Ghosh N. N.: Recent advancement on polybenzoxazine – A newly developed high performance thermoset. Journal of Polymer Science Part A: Polymer Chemistry, **47**, 5565–5576 (2009). DOI: 10.1002/pola.23597

[7] Takeichi T., Kano T., Agag T.: Synthesis and thermal cure of high molecular weight polybenzoxazine precursors and the properties of the thermosets. Polymer, **46**, 12172–12180 (2005). DOI: 10.1016/j.polymer.2005.10.088

[8] Ishida H., Allen D. J.: Mechanical characterization of copolymers based on benzoxazine and epoxy. Polymer, **37**, 4487–4495 (1996). DOI: 10.1016/0032-3861(96)00303-5

[9] Chernykh A., Agag T., Ishida H.: Novel benzoxazine monomer containing diacetylene linkage: An approach to benzoxazine thermosets with low polymerization temperature without added initiators or catalysts. Polymer, **50**, 3153–3157 (2009). DOI: 10.1016/j.polymer.2009.04.061

[10] Kimura H., Matsumoto A., Ohtsuka K.: Studies on new type of phenolic resin – Curing reaction of bisphenol-A-based benzoxazine with epoxy resin using latent curing agent and the properties of the cured resin. Journal of Applied Polymer Science, **109**, 1248–1256 (2008). DOI: 10.1002/app.28279

[11] Kimura H., Matsumoto A., Hasegawa K., Ohtsuka K., Fukuda A.: Epoxy resin cured by bisphenol A based benzoxazine. Journal of Applied Polymer Science, **68**, 1903–1910 (1998). DOI: 10.1002/(sici)1097-4628(19980620)68:12<1903::aid-app2>3.0.co;2-p

[12] Rimdusit S., Pirstpindvong S., Tanthapanichakoon W., Damrongsakkul S.: Toughening of polybenzoxazine by alloying with urethane prepolymer and flexible epoxy: A comparative study. Polymer Engineering and Science, **45**, 288–296 (2005). DOI: 10.1002/pen.20273

[13] Kimura H., Matsumoto A., Ohtsuka K.: New type of phenolic resin: Curing reaction of phenol-novolac based benzoxazine with bisoxazoline or epoxy resin using latent curing agent and the properties of the cured resin. Journal of Applied Polymer Science, **112**, 1762–1770 (2009). DOI: 10.1002/app.29301

[14] Grishchuk S., Mbhele Z., Schmitt S., Karger-Kocsis J.: Structure, thermal and fracture mechanical properties of benzoxazine-modified amine-cured DGEBA epoxy resins. Express Polymer Letters, **5**, 273–282 (2011). DOI: 10.3144/expresspolymlett.2011.27

[15] Grishchuk S., Schmitt S., Vorster O. C., Karger-Kocsis J.: Structure and properties of amine-hardened epoxy/benzoxazine hybrids: Effect of epoxy resin functionality. Journal of Applied Polymer Science, **124**, 2824–2837 (2012). DOI: 10.1002/app.35302

[16] Rao B. S., Reddy K. R., Pathak S. K., Pasala A. R.: Benzoxazine–epoxy copolymers: effect of molecular weight and crosslinking on thermal and viscoelastic properties. Polymer International, **54**, 1371–1376 (2005). DOI: 10.1002/pi.1853

[17] Rimdusit S., Kunopast P., Dueramae I.: Thermomechanical properties of arylamine-based benzoxazine resins alloyed with epoxy resin. Polymer Engineering and Science, **51**, 1797–1807 (2011). DOI: 10.1002/pen.21969

[18] Grishchuk S., Sorochynska L., Vorster O. C., Karger-Kocsis J.: Structure, thermal, and mechanical properties of DDM-hardened epoxy/benzoxazine hybrids: Effects of epoxy resin functionality and ETBN toughening. Journal of Applied Polymer Science, **127**, 5082–5093 (2013). DOI: 10.1002/app.38123

[19] Kuo S-W., Liu W-C.: Synthesis and characterization of a cured epoxy resin with a benzoxazine monomer containing allyl groups. Journal of Applied Polymer Science, **117**, 3121–3127 (2010). DOI: 10.1002/app.32093

[20] Sawaryn C., Landfester K., Taden A.: Benzoxazine miniemulsions stabilized with polymerizable nonionic benzoxazine surfactants. Macromolecules, **43**, 8933–8941 (2010). DOI: 10.1021/ma101169g

[21] Sawaryn C., Landfester K., Taden A.: Benzoxazine miniemulsions stabilized with multifunctional main-chain benzoxazine protective colloids. Macromolecules, **44**, 5650–5658 (2011). DOI: 10.1021/ma200973g

[22] Chernykh A., Liu J., Ishida H.: Synthesis and properties of a new crosslinkable polymer containing benzoxazine moiety in the main chain. Polymer, **47**, 7664–7669 (2006). DOI: 10.1016/j.polymer.2006.08.041

[23] Choi J-H., Kim H-J.: Three hardness test methods and their relationship on UV-curable epoxy acrylate coatings for wooden flooring systems. Journal of Industrial and Engineering Chemistry, **12**, 412–417 (2006).

[24] Griffin W. C.: Calculation of HLB values of non-ionic surfactants. Journal of the Society of Cosmetic Chemists, **5**, 249–256 (1954).

[25] Hecht L. L., Schoth A., Muñoz-Espi R., Javadi A., Köhler K., Miller R., Landfester K., Schuchmann H. P.: Determination of the ideal surfactant concentration in miniemulsion polymerization. Macromolecular Chemistry and Physics, **214**, 812–823 (2013). DOI: 10.1002/macp.201200583

[26] Landfester K., Bechthold N., Tiarks F., Antonietti M.: Formulation and stability mechanisms of polymerizable miniemulsions. Macromolecules, **32**, 5222–5228 (1999). DOI: 10.1021/ma990299+

[27] Landfester K.: Recent developments in miniemulsions – Formation and stability mechanisms. Macromolecular Symposia, **150**, 171–178 (2000). DOI: 10.1002/1521-3900(200002)150:1<171::aid-masy171>3.0.co;2-d

[28] Ning X., Ishida H.: Phenolic materials via ring-opening polymerization: Synthesis and characterization of bisphenol-A based benzoxazines and their polymers. Journal of Polymer Science Part A: Polymer Chemistry, **32**, 1121–1129 (1994). DOI: 10.1002/pola.1994.080320614

[29] Ning X., Ishida H.: Phenolic materials via ring-opening polymerization of benzoxazines: Effect of molecular structure on mechanical and dynamic mechanical properties. Journal of Polymer Science Part B: Polymer Physics, **32**, 921–927 (1994). DOI: 10.1002/polb.1994.090320515

[30] Karger-Kocsis J., Grishchuk S., Sorochynska L., Rong M. Z.: Curing, gelling, thermomechanical, and thermal decomposition behaviors of anhydride-cured epoxy (DGEBA)/epoxidized soybean oil compositions. Polymer Engineering and Science, **54**, 747–755 (2014). DOI: 10.1002/pen.23605

[31] Chow W. S., Grishchuk S., Burkhart T., Karger-Kocsis J.: Gelling and curing behaviors of benzoxazine/epoxy formulations containing 4,4′-thiodiphenol accelerator. Thermochimica Acta, **543**, 172–177 (2012). DOI: 10.1016/j.tca.2012.05.015

[32] Wang H., Zhao P., Ling H., Ran Q., Gu Y.: The effect of curing cycles on curing reactions and properties of a ternary system based on benzoxazine, epoxy resin, and imidazole. Journal of Applied Polymer Science, **127**, 2169–2175 (2013). DOI: 10.1002/app.37778

[33] Wirasate S., Dhumrongvaraporn S., Allen D. J., Ishida H.: Molecular origin of unusual physical and mechanical properties in novel phenolic materials based on benzoxazine chemistry. Journal of Applied Polymer Science, **70**, 1299–1306 (1998). DOI: 10.1002/(sici)1097-4628(19981114)70:7<1299::aid-app6>3.3.co;2-b

[34] Kim H-D., Ishida H.: Study on the chemical stability of benzoxazine-based phenolic resins in carboxylic acids. Journal of Applied Polymer Science, **79**, 1207–1219 (2001). DOI: 10.1002/1097-4628(20010214)79:7<1207::aid-app80>3.0.co;2-3

eXPRESS Polymer Letters Vol.8, No.8 (2014) 588–595
Available online at www.expresspolymlett.com
DOI: 10.3144/expresspolymlett.2014.62

Superhydrophobic polyimide films with high thermal endurance via UV photo-oxidation

H. Y. Gu[1,2], *Z. Y. Qi*[1], *W. Wu*[3], *Y. Zeng*[3], *L. X. Song*[1*]

[1]Key Laboratory of Inorganic Coating Materials, Shanghai Institute of Ceramics, Chinese Academy of Sciences, 1295 Dingxi Road, 200050 Shanghai, China
[2]University of Chinese Academy of Sciences, 19 Yuquan Road,, 100049 Beijing, China
[3]The State Key Laboratory of High Performance Ceramics and Superfine Microstructures, Shanghai Institute of Ceramics, Chinese Academy of Sciences, 1295 Dingxi Road, 200050 Shanghai, China

Received 16 February 2014; accepted in revised form 21 April 2014

Abstract. UV photo-oxidation was first applied to fabricate superhydrophobic polyimide (PI) films in combination with fluoroalkylsilane (FAS) modification. During prolonged UV irradiation, commercial flat PI films evolved to form unique micro/nanostructures. Meanwhile, the root mean square (RMS) surface roughness increased from 1.74 to 53.70 nm, leading to a gradual increase of WCA from 105.1 to 159.2° after FAS treatment. After 72 h of UV radiation exposure, the micro/nano-structured and FAS-modified PI films exhibited superhydrophobicity with water contact angle (WCA) larger than 150° and sliding angle (SA) less than 5°. The superhydrophobicity remained even after annealing at 350°C, which enabled stable utilization under elevated temperature. Stable micro/nanostructures and chemical bonding of FAS were found to contribute to the high thermal endurance. Moreover, the formation mechanism of the superhydrophobic PI films was investigated. The proposed UV photo-oxidation method provides a new route for the industrial fabrication of thermally stable superhydrophobic PI films.

Keywords: *nanomaterials, superhydrophobic polyimide, UV photo-oxidation, thermal properties*

1. Introduction

Superhydrophobic surfaces with water contact angle (WCA) larger than 150° have attracted extensive interest in recent years [1, 2]. Superhydrophobic polymers such as polystyrene (PS) are quite attractive owing to their low cost, light weight and ease of processing [3–5]. However, the performance of these materials deteriorates considerably when exposed to extreme environmental conditions (e.g., heat and tension), which severely limits their applications in harsh environments [6]. Polyimide (PI), a widely used polymer, can overcome these drawbacks due to its unique physical and chemical properties such as excellent thermal stability, high strength and good chemical resistance [7–10]. Therefore, superhydrophobic PI is believed to be more durable for applications in anti-corrosion [11], anti-contamination [12], etc.

Superhydrophobic surfaces should have high surface roughness as well as low surface energy [1]. Generally, CF_3-terminated flat surfaces with the lowest surface energy have a WCA not greater than 120°. Larger WCA could only be obtained by altering the surface roughness [13]. Techniques including template [11, 14–16], electrospinning [6, 17, 18], laser [12, 19] and plasma [20–22] are used to construct surface structures for superhydrophobic PI. However, complex operations, novel precursors,

*Corresponding author, e-mail: sicsonglx@gmail.com

masks or vacuum instruments are usually involved. Hence, facile strategies suitable for industrial fabrication are urgently required.

In this paper, a facile UV photo-oxidation method, which can be easily performed in air at atmospheric pressure, was proposed for the first time to tailor surface morphology of commercial PI films to achieve superhydrophobicity. The evolution of topography and WCA during prolonged UV treatment was investigated. Thermal endurance of the superhydrophobic PI films and formation mechanism of the superhydrophobicity were discussed.

2. Experimental

2.1. Materials

Pyromellitic dianhydride-oxydianiline (PMDA-ODA) type PI films (Kapton 100H, $C_{22}H_{10}O_5N_2$) were obtained from Toray DuPont (Tokyo, Japan). 1H,1H,2H,2H-Perfluorodecyltriethoxysilane (FAS, $C_{10}F_{17}H_4Si(OCH_2CH_3)_3$) was supplied by Alfa Aesar (Ward Hill, MA, USA). Ultra-pure water was prepared using a Milli-Q-Plus system (Millipore, Bedford, MA, USA). Analytical grade ethanol was provided by Sinopharm Chemical Reagent Co., Ltd. (Shanghai, China). Prior to use, all PI films were ultrasonically cleaned for 5 min with purified water followed by ethanol and dried in an oven (DHG-9023B, Bilon, Shanghai, China) under 100°C for 1 h. Other chemicals were used as received.

2.2. Fabrication of hydrophobic polyimide

The method consisted of two main steps, i.e. UV photo-oxidation and consequent fluoroalkylsilane modification (UV/FAS), as shown in Figure 1. UV photo-oxidation was conducted in a chamber (HWS-80, BiLon, Shanghai, China) with a mercury-quartz lamp (GPHO287T5VH/4, SunMonde, Shanghai, China) emitting UV light at 254 and 185 nm. The output at 185 nm was equivalent to about 10% of that at 254 nm according to the instructions of the UV lamp. PI films were irradiated 10 mm from the lamp for 24, 48, 72 or 144 h in air at atmospheric pressure, where the intensity of the 254 nm UV light was measured to be 10 mW/cm^2. Fluoroalkylsilane modification was then carried out with FAS in a heated reactor. Specifically, a few droplets (30–50 μL) of FAS were dispensed at the bottom of a Teflon container (200 mL) using a micro-adjustable pipette (720000, Dragon, Shanghai, China) while the UV-treated PI films were placed vertically in the

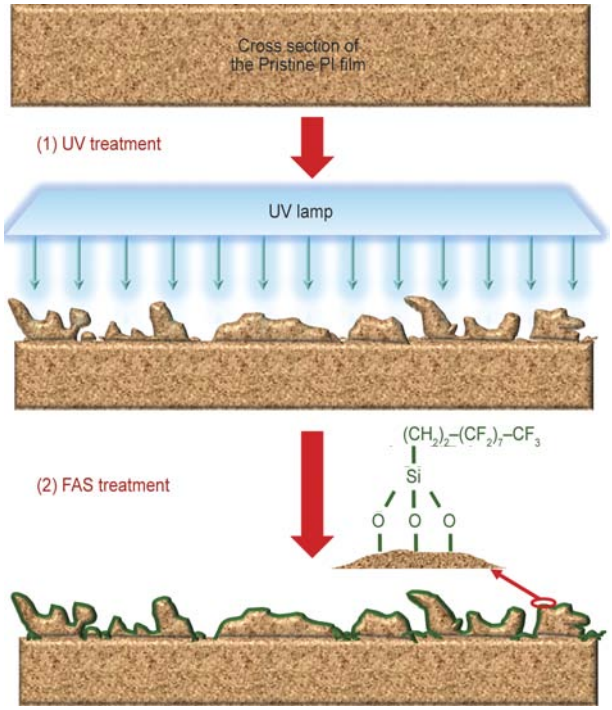

Figure 1. Schematic illustration of the processes involved in the fabrication of hydrophobic PI films

Teflon container, which was further sealed in a stainless steel autoclave. The reactor was then annealed at 120°C for 2 h to enable the vapor of FAS to react with the modified PI films. Finally, the samples were heated at 150°C for 3 h to volatilize unreacted FAS molecules.

2.3. Thermal treatment

Thermal endurance of superhydrophobicity of the films was assessed by measuring WCA after annealing for 2 h under various temperature conditions. A piece of 25×70 mm^2 superhydrophobic PI film was fabricated using the method described above (72 h of UV photo-oxidation). Then it was cut into seven pieces with identical dimension. One piece is preserved in air at atmospheric pressure without any further treatment, the other six pieces were annealed for 2 h at 100, 150, 200, 250, 300 and 350°C, respectively. Then the wettability was studied after the thermally treated films cooled down.

2.4. Characterization

The morphology and element distribution were characterized by scanning electron microscopy (SEM) coupled with energy-dispersive X-ray spectroscopy (EDS) on an FEI Magellan 400 microscope (Hillsboro, OR, USA). The surface roughness was analyzed using an atomic force microscope (AFM)

(Nanoscope V Multimode AFM system, Bruker, Germany) in tapping mode. The surface chemical composition and bonding were examined using an X-ray photoelectron spectroscopy (XPS) (ESCALAB-250 instrument, Thermo VG Scientific, West Sussex, UK). Elemental content was calculated from XPS spectra, based on the peak area of C1s, O1s, F1s and Si2p and corresponding sensitivity factors using the Avantage software. The static WCA was measured with 5 μL water using a contact angle system (SL200B, Solon, Shanghai, China) at ambient temperature. The average WCA value was obtained by measuring the same sample at five different positions. The sliding angle (SA) was determined by slowly tilting the sample stage until the 10 μL water droplet starting moving.

3. Results and discussion

3.1. Surface morphology and wettability

The pristine PI film possessed a flat and slightly hydrophilic surface (WCA = 74. 5°) as shown in Figure 2a. To obtain hydrophobicity, FAS treatment was firstly performed on the pristine PI films directly since FAS containing fluoroalkyl chains is commonly used to lower the surface energy [1, 14, 16]. The modified PI surface exhibited hydrophobicity with a WCA of 105.1° (Figure 2b), which was still far below the criterion value (i.e., 150°) of superhydrophobicity. This indicated that the reduction of surface energy was not enough to render the flat PI surface superhydrophobicity and modification of surface structure was required. For this reason, UV irradiation was carried out, in an attempt to change the surface morphology. After 72 h of UV radiation exposure, as expected, significant surface roughening was observed and an obvious reduction of WCA to nearly 0° (Figure 2a, 2c) was measured. Further treatment by FAS after 72 h of UV irradiation resulted in a WCA of up to 156.8° (Figure 3c) and a low SA less than 5° (Figure 3g), indicating a superhydrophobic surface. The notable changes of WCA clearly demonstrated the importance of specific surface topography for the wettability. Moreover, UV irradiation was proven to be an effective way to alter the surface topography of PI films.

The evolution of surface morphology and corresponding WCA with UV radiation exposure time was further investigated. As presented in Figure 3a–3l, nanoprotrusions emerged, aggregated and interconnected progressively when UV radiation exposure prolonged from 24 to 144 h. After 72 h, micro/nanostructures with protrusions, ridges and channels were formed on the surfaces, leading to significant surface roughening. The roughness of the surfaces was further quantified by AFM. The root mean square (RMS) roughness and WCA values against UV irradiation time are plotted in Figure 4. As shown in Figure 4, the RMS roughness increased from 1.74 to 53.70 nm with irradiation time extended from 0 to 144 h. Simultaneously, the WCA increased from 105.1 to 159.2° due to the surface roughening. Additionally, water drops (10 μL) were found to readily roll off the resultant hydrophobic PI films when UV photo-oxidation time exceeded 72 h. Therefore, the wettability of PI films could be tuned by changing the UV irradiation time and 72 h of exposure time was enough to achieve superhydrophobicity. Considering possible adverse effects on the substrates during UV radiation exposure, minimum UV irradiation time should be used, provided that the required superhydrophobicity is achieved.

3.2. Thermal endurance

High thermal stability is a significant advantage of PI over other polymers. It is reasonable to expect the as-prepared superhydrophobic PI films to be thermally stable. In order to validate the hypothesis, we invested the thermal endurance of superhydropho-

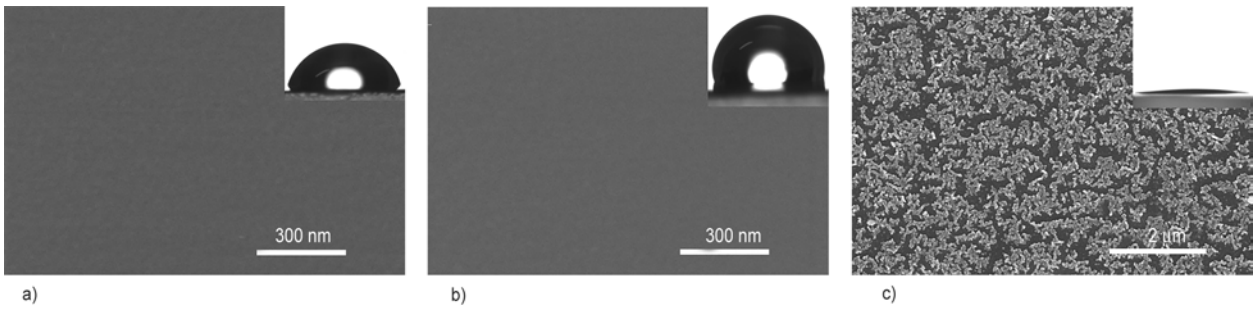

Figure 2. SEM images of pristine (a), FAS (b) and UV (c) treated PI films. The insets are optical images of water droplets on corresponding surfaces.

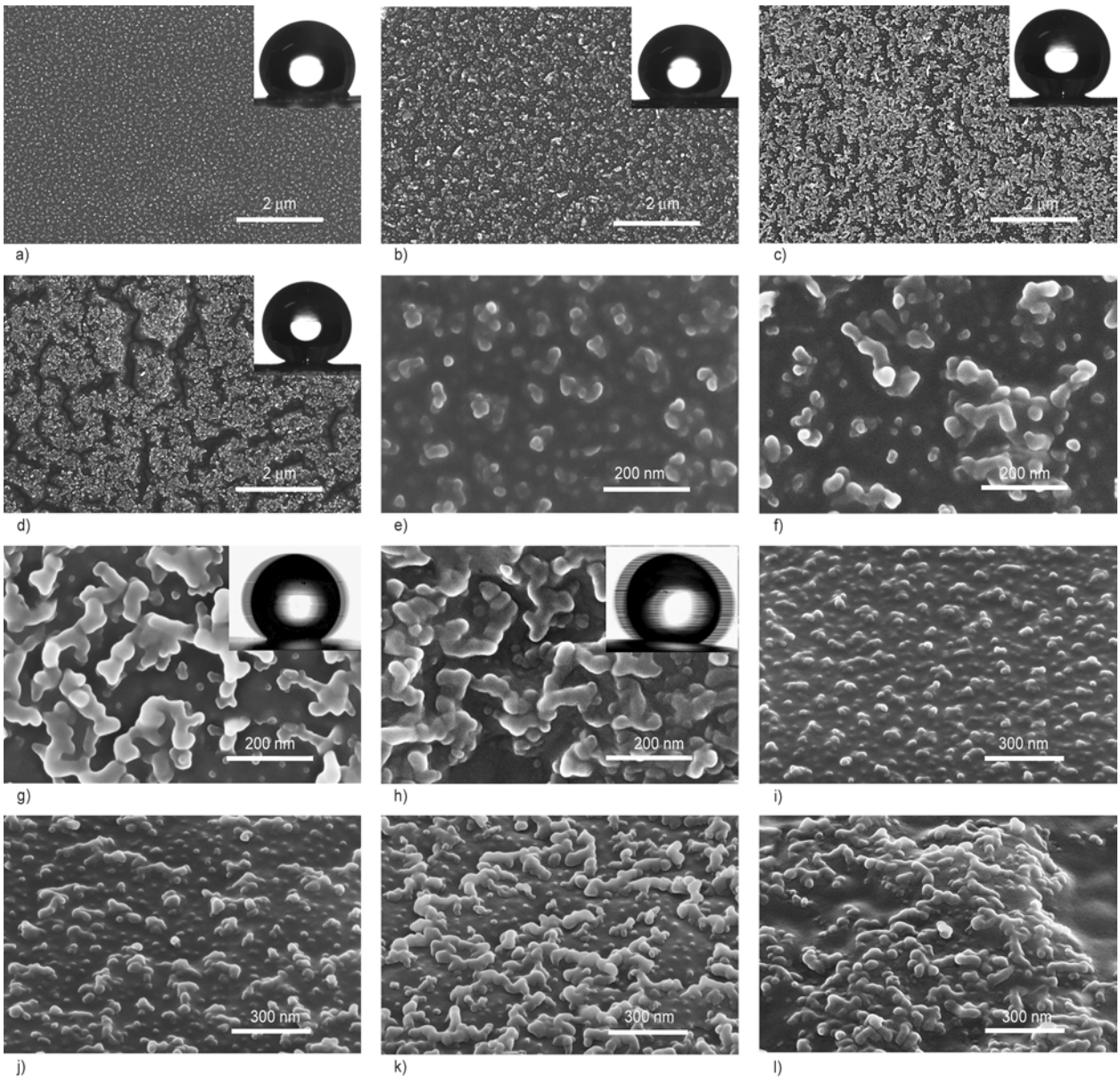

Figure 3. 0° (a–h) and 45° (i–l) tilt SEM images of UV/FAS treated PI films. The UV treatment periods are 24 h (a, e, i), 48 h (b, f, j), 72 h (c, g, k) and 144 h (d, h, l), respectively. The insets are optical images of static water droplets (a–d) on corresponding horizontal surfaces and water droplets (g, h) sliding on slightly tilted surfaces.

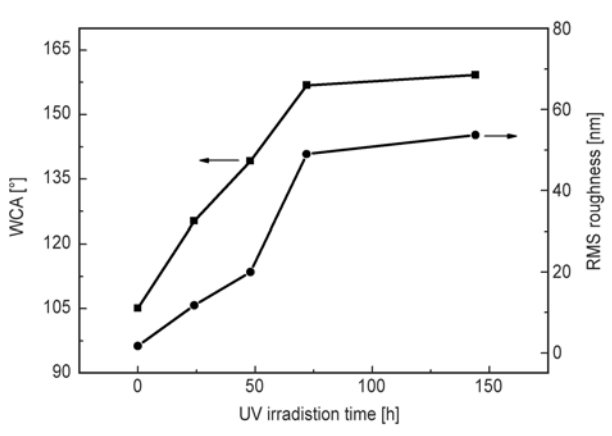

Figure 4. WCA and RMS roughness plotted against UV irradiation time

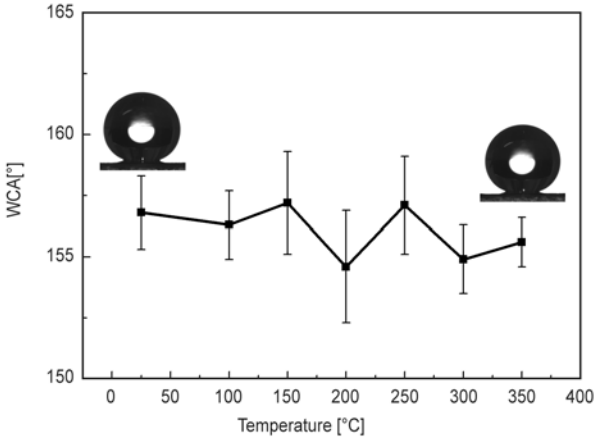

Figure 5. WCA plotted against thermal treatment temperature

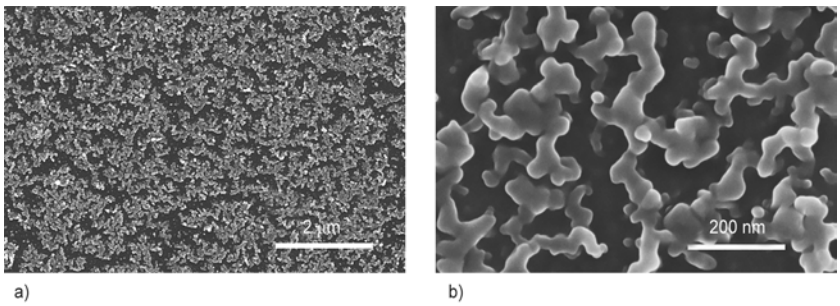

Figure 6. SEM images of annealed (350°C) superhydrophobic PI films using different magnifications

bicity by annealing the UV (72 h)/FAS-treated PI films below the glass transition temperature (T_g) of PI [7]. Figure 5 presents the WCA values of samples annealed at corresponding temperatures (100–350°C) for 2 h. Long time thermal treatment seemed to have little effect on the WCA. Only a slight fluctuation of WCA around 155° was observed. The SA was also below 5° for all samples investigated in Figure 5. The WCA larger than 150° and SA less than 5° after annealing of the superhydrophobic films demonstrated the highly stable superhydrophobicity. To the contrary, most well-known polymers such as PS cannot sustain their superhydrophobicity at high temperature due to unstable micro/nanostructures [6]. The remained superhydrophobicity of PI films can be ascribed to the thermally stable surface topography and composition. This is confirmed by the well-preserved micro/nanostructures of 350°C annealed UV (72 h)/FAS-treated PI (Figure 6) and almost unchanged surface elemental content (relative intensity of peaks) as determined by XPS shown in Figure 7. Specifically, the amount of F changed little from 53.4 at.% (before annealing) to 52.1 at.% (after annealing). In addition, the distribution of elements for UV (72 h)/FAS-treated PI films during annealing at 350°C were further investigated. As shown in Figure 8, F and Si (derived

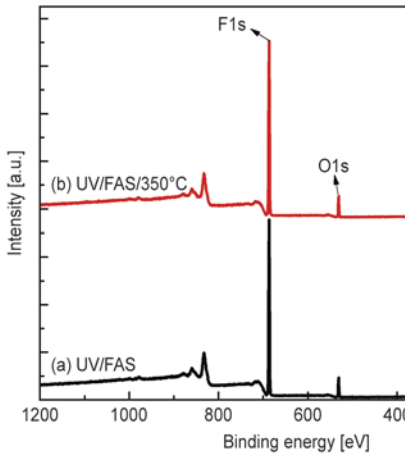

Figure 7. XPS spectra of UV (72 h)/FAS-treated PI before (a) and after (b) annealing at 350°C

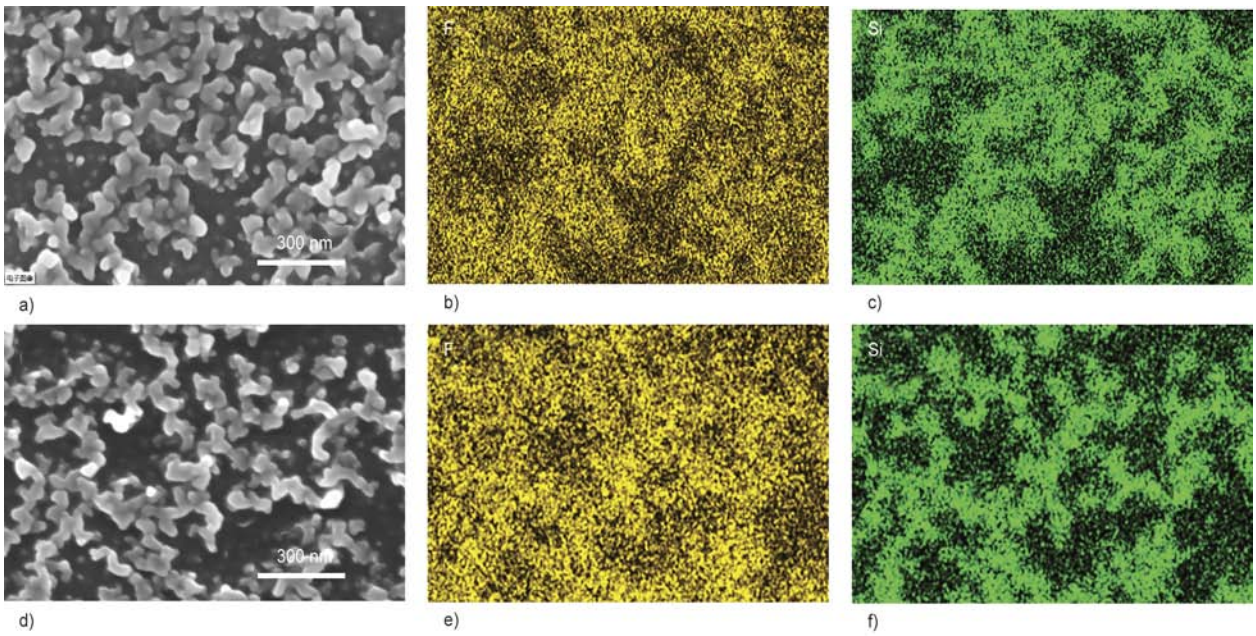

Figure 8. FESEM-EDS mappings for F and Si of UV (72 h)/FAS-treated PI before (a–c) and after (d–f) annealing at 350°C

from FAS) presented the coincident distribution patterns with the corresponding SEM images both before and after heat treatment at 350°C. Little change in the distribution of F and Si was found after annealing. It is worth pointing out the non-uniform distribution of F and Si revealed by the FESEM-EDS mappings. It is clearly shown that FAS distributed preferentially at the ridges on both the as-prepared and the annealed films. FAS modification was proven to be a chemical process that was more likely to occur at the ridges. The strong chemical bonding of FAS on the surface also contributed to the stable superhydrophobicity.

3.3. Formation mechanism

Based on the previous discussion, we propose a possible formation mechanism for the superhydrophobic PI films, which was illustrated in Figure 9. During the UV irradiation, low-molecular-weight polymer chains were firstly formed on the film surfaces because of the UV photo-oxidation induced chain scission and recombination [23]. Meanwhile, active oxygens such as atomic oxygens generated during UV radiation also reacted with PI [23]. These oxidized polymer chains had a tendency to aggregate into nanoprotrusions due to high energy dangling bonds and polar groups. Driven by the different interface free energy levels between irradiated surface and underlying PI, the nanoprotrusions further interconnected to form ridges through surface dynamics (e.g., etching, migration and redeposition) [24]. The evolution of the nanoprotrusions with prolonged UV irradiation resulted in the increase of surface roughness, as shown in Figure 3 and Figure 4. Consequently, unique micro/nanostructures with the RMS roughness larger than 49.00 nm were constructed. Simultaneously, oxidized polymer chains generated hydrophilic groups in the presence of water molecules in air on UV-treated surfaces (e.g., OH groups) [23], especially at the ridges since more oxidized polymer chains aggregated there. These groups reacted with FAS (fluoroalkyl silanization). Thus, fluoroalkyl chains were firmly grafted onto the UV-irradiated surfaces, resulting in stable superhydrophobicity on the PI films.

4. Conclusions

In summary, UV irradiation was used for the first time to prepare superhydrophobic PI films. Unique micro/nanostructures consisting of protrusions, ridges and channels were constructed on the PI surfaces after 72 h of UV photo-oxidation. The surface roughening led to continuously increased hydrophobicity after further fluoroalkyl silanization. Superhydrophobic surfaces with WCA larger than 156.8° and SA less than 5° were achieved for the micro/nano-struc-

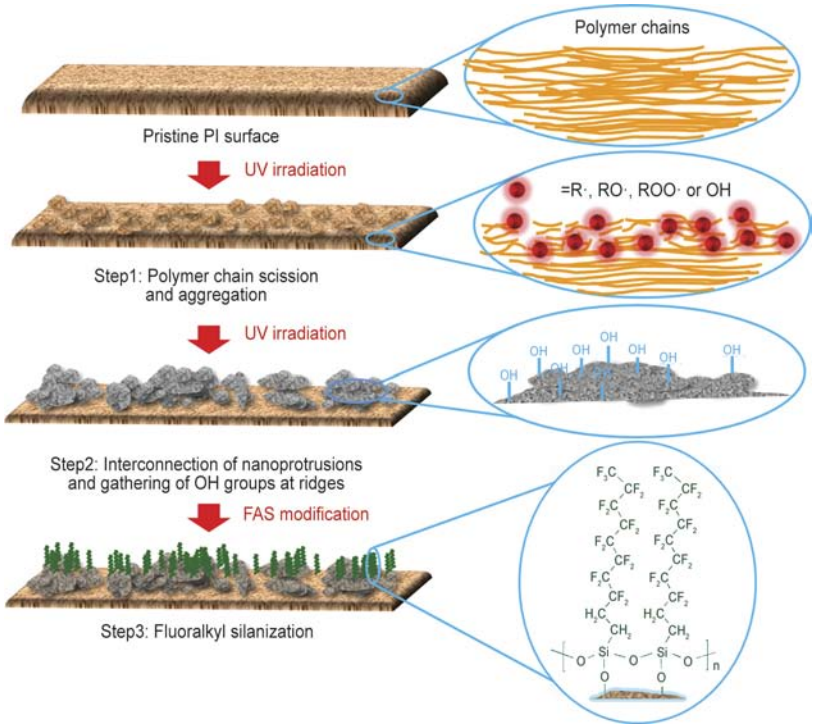

Figure 9. Proposed mechanism for the formation of superhydrophobic PI films

tured and FAS-modified PI films, indicating that the water drops will easily roll off a slightly tilted substrate. The superhydrophobicity remained even after annealing under 350°C. Stable micro/nanostructures and chemical bonding of FAS were responsible for the high thermal endurance of superhydrophobicity. These heat endurable superhydrophobic PI films would find lots of practical applications in anti-corrosion, anti-contamination and anti-icing systems.

References

[1] Liu K., Tian Y., Jiang L.: Bio-inspired superoleophobic and smart materials: Design, fabrication, and application. Progress in Materials Science, **58**, 503–564 (2013). DOI: 10.1016/j.pmatsci.2012.11.001

[2] Liu K., Jiang L.: Bio-inspired self-cleaning surfaces. Annual Review of Materials Research, **42**, 231–263 (2012). DOI: 10.1146/annurev-matsci-070511-155046

[3] Darmanin T., de Givenchy E. T., Amigoni S., Guittard F.: Superhydrophobic surfaces by electrochemical processes. Advanced Materials, **25**, 1378–1394 (2013). DOI: 10.1002/adma.201204300

[4] Wolfs M., Darmanin T., Guittard F.: Superhydrophobic fibrous polymers. Polymer Reviews, **53**, 460–505 (2013). DOI: 10.1080/15583724.2013.808666

[5] Sahoo B. N., Kandasubramanian B., Sabarish B.: Controlled anisotropic wetting behaviour of multi-scale slippery surface structure of non fluoro polymer composite. Express Polymer Letters, **7**, 900–909 (2013). DOI: 10.3144/expresspolymlett.2013.88

[6] Gong G., Wu J., Liu J., Sun N., Zhao Y., Jiang L.: Bio-inspired adhesive superhydrophobic polyimide mat with high thermal stability. Journal of Materials Chemistry, **22**, 8257–8262 (2012). DOI: 10.1039/c2jm16503a

[7] Ghosh M. K., Mittal K. L.: Polyimides: Fundamentals and applications. Marcel Dekker, New York (1996).

[8] Zhu Y-Q., Zhao P-Q., Cai X-D., Meng W-D., Qing F-L.: Synthesis and characterization of novel fluorinated polyimides derived from bis[4-(4′-aminophenoxy) phenyl]-3,5-bis(trifluoromethyl)phenyl phosphine oxide. Polymer, **48**, 3116–3124 (2007). DOI: 10.1016/j.polymer.2007.03.057

[9] Han Y., Fang X-Z., Zuo X-X.: Melt processable homo- and copolyimides with high thermo-oxidative stability as derived from mixed thioetherdiphthalic anhydride isomers. Express Polymer Letters, **4**, 712–722 (2010). DOI: 10.3144/expresspolymlett.2010.86

[10] Uğur M. H., Toker R. D., Kayaman-Apohan N., Güngör A.: Preparation and characterization of novel thermoset polyimide and polyimide-peo doped with $LiCF_3SO_3$. Express Polymer Letters, **8**, 123–132 (2014). DOI: 10.3144/expresspolymlett.2014.15

[11] Chang K-C., Lu H-I., Peng C-W., Lai M-C., Hsu S-C., Hsu M-H., Tsai Y-K., Chang C-H., Hung W-I., Wei Y., Yeh J-M.: Nanocasting technique to prepare lotus-leaf-like superhydrophobic electroactive polyimide as advanced anticorrosive coatings. ACS Applied Materials and Interfaces, **5**, 1460–1467 (2013). DOI: 10.1021/am3029377

[12] Wohl C. J., Belcher M. A., Chen L., Connell J. W.: Laser ablative patterning of copoly(imide siloxane)s generating superhydrophobic surfaces. Langmuir, **26**, 11469–11478 (2010). DOI: 10.1021/la100958r

[13] Nishino T., Meguro M., Nakamae K., Matsushita M., Ueda Y.: The lowest surface free energy based on $–CF_3$ alignment. Langmuir, **15**, 4321–4323 (1999). DOI: 10.1021/la981727s

[14] Zhao Y., Li M., Lu Q., Shi Z.: Superhydrophobic polyimide films with a hierarchical topography: Combined replica molding and layer-by-layer assembly. Langmuir, **24**, 12651–12657 (2008). DOI: 10.1021/la8024364

[15] Zhu S., Li Y., Zhang J., Lü C., Dai X., Jia F., Gao H., Yang B.: Biomimetic polyimide nanotube arrays with slippery or sticky superhydrophobicity. Journal of Colloid and Interface Science, **344**, 541–546 (2010). DOI: 10.1016/j.jcis.2009.12.047

[16] Liu K., Du J., Wu J., Jiang L.: Superhydrophobic gecko feet with high adhesive forces towards water and their bio-inspired materials. Nanoscale, **4**, 768–772 (2012). DOI: 10.1039/c1nr11369k

[17] Weng C-J., Jhuo Y-S., Chang C-H., Feng C-F., Peng C-W., Dai C-F., Yeh J-M., Wei Y.: A smart surface prepared using the switchable superhydrophobicity of neat electrospun intrinsically electroactive polyimide fiber mats. Soft Matter, **7**, 10313–10318 (2011). DOI: 10.1039/c1sm06097j

[18] Park J. Y., Oh K. O., Won J. C., Han H., Jung H. M., Kim Y. S.: Facile fabrication of superhydrophobic coatings with polyimide particles using a reactive electrospraying process. Journal of Materials Chemistry, **22**, 16005–16010 (2012). DOI: 10.1039/c2jm32210b

[19] Oliveira V., Nunes B., Vilar R.: Wetting response of KrF laser ablated polyimide surfaces. Nuclear Instruments and Methods in Physics Research Section B: Beam Interactions with Materials and Atoms, **268**, 1626–1630 (2010). DOI: 10.1016/j.nimb.2010.03.006

[20] Scheen G., Ziouche K., Bougrioua Z., Godts P., Leclercq D., Lasri T.: Simultaneous fabrication of superhydrophobic and superhydrophilic polyimide surfaces with low hysteresis. Langmuir, **27**, 6490–6495 (2011). DOI: 10.1021/la1050805

[21] Barshilia H. C., Ananth A., Gupta N., Anandan C.: Superhydrophobic nanostructured Kapton® surfaces fabricated through Ar + O_2 plasma treatment: Effects of different environments on wetting behaviour. Applied Surface Science, **268**, 464–471 (2013).
DOI: 10.1016/j.apsusc.2012.12.130

[22] Wohl C. J., Belcher M. A., Ghose S., Connell J. W.: Modification of the surface properties of polyimide films using polyhedral oligomeric silsesquioxane deposition and oxygen plasma exposure. Applied Surface Science, **255**, 8135–8144 (2009).
DOI: 10.1016/j.apsusc.2009.05.030

[23] Sener U., Parekh B., Entenberg A., Debies T., Takács G. A.: Surface modification of poly(biphenyl dianhydride-para-phenylene diamine) (BPDA-PDA) polyimide by UV photo-oxidation. Journal of Adhesion Science and Technology, **20**, 319–334 (2006).
DOI: 10.1163/156856106776381776

[24] Yun J., Bae T-S., Kwon J-D., Lee S., Lee G-H.: Antireflective silica nanoparticle array directly deposited on flexible polymer substrates by chemical vapor deposition. Nanoscale, **4**, 7221–7230 (2012).
DOI: 10.1039/c2nr32381h

eXPRESS Polymer Letters Vol.8, No.8 (2014) 596–608
Available online at www.expresspolymlett.com
DOI: 10.3144/expresspolymlett.2014.63

Evolution of carbon nanotube dispersion in preparation of epoxy-based composites: From a masterbatch to a nanocomposite

M. Aravand[*]*, S. V. Lomov, I. Verpoest, L. Gorbatikh*

Department of Materials Engineering, KU Leuven, Kasteelpark Arenberg 44, B-3001 Leuven, Belgium

Received 1 February 2014; accepted in revised form 22 April 2014

Abstract. The state of carbon nanotube (CNT) dispersion in epoxy is likely to change in the process of composite production. In the present work CNT dispersion is characterized at different stages of nanocomposite preparation: in the original masterbatch with high CNT concentration, after masterbatch dilution, in the process of curing and in the final nanocomposite. The evaluation techniques included dynamic rheological analysis of the liquid phases, optical, environmental and charge contrast scanning electron microscopy, electrochemical impedance spectroscopy and dynamic mechanical analysis. The evolution of the CNT dispersion was assessed for two CNT/epoxy systems with distinctly different dispersion states induced by different storage time. Strong interactions between CNT clusters were revealed in the masterbatch with a longer storage time. Upon curing CNT clusters in this material formed a network-like structure. This network enhanced the elastic behaviour and specific conductivity of the resulting nanocomposite, leading to a partial electrical percolation after curing.

Keywords: *nanocomposites, multiwall carbon nanotubes, dispersion state, rheometry, microscopy*

1. Introduction

Carbon nanotubes (CNTs) have shown potential to improve the performance of fiber-reinforced composites when added in small quantities in the polymer matrix. They can influence the composite mechanical, electrical and thermal properties [1–3]. Reported improvements, however, vary significantly from one study to another and are not always reproducible. Variations in the dispersion state of nanotubes are likely to be responsible for these problems.

Agglomeration represents an important challenge when using CNTs as reinforcement in polymers and their composites. The excessive surface area of CNTs creates substantial van der Waals attraction forces, which together with the low viscosity of the matrix can give rise to the formation of relatively large agglomerates during composite production. The reinforcing efficiency of CNTs in the agglomerated form is known to be significantly lower than of individually dispersed CNTs [4, 5]. A uniform dispersion of nanotubes within the polymer matrix is, therefore, an important prerequisite for improved mechanical properties at minimal CNT contents [6, 7]. Additionally, the presence of CNT agglomerates in the liquid resin can impose serious issues when this resin is used to produce a fibre reinforced composite. Large clusters of nanotubes can be filtered out by the fibre reinforcement during the impregnation step or act as defects in consolidated composite [2]. However, agglomeration of the initially dispersed nanotubes is not always an undesirable phenomenon. For example, formation of an agglomerated CNTs network is beneficial and even necessary

[*]Corresponding author, e-mail: aravand@gmail.com

for electrical conductivity of the composite [7–10]. The results of recent study suggest that the presence of such a network in the matrix, can enhance certain mechanical properties of a fibre reinforced composite [11].

During the multi-step composite production process various factors can affect the dispersion of CNTs. These effects could not be necessarily anticipated and generalized through the characterization results of any other step. For instance, when the nanotubes are introduced to the epoxy resin at high concentrations (masterbatches), the dispersion state can be affected by storage history, processing conditions and also by curing reaction which can induce so called secondary agglomerations [9]. This may or may not lead to the formation of a three dimensional network of CNT agglomerates depending on the different factors and the initial dispersion state of the liquid resin.

Depending on the physical state of the system, various direct or indirect methods for the assessment of the CNT dispersion in epoxy based composites have been reported in the literature. Scanning and transmission electron microscopy are widely used to directly visualize CNT dispersion in the solid state [12–15]. Optical microscopy is also commonly used to observe larger CNT agglomerates both in liquid dispersions and solid nanocomposite films [9, 16–19]. However, microscopic techniques could not be efficiently employed at liquid state (especially in high concentration dispersions) and could merely provide a qualitative measure of the dispersion state over a small field of view.

Indirect methods based on static or dynamic rheological analyses could efficiently be employed to obtain quantitative measures of the nanoparticle dispersion in liquid resins [4, 19–22]. This is mainly based on the fact that the dispersion quality of the nanoparticles often affects the viscosity and viscoelastic properties of liquid suspensions in different ways. However, rheological characterizations are better to be confirmed by other techniques, such as microscopy, because reagglomeration of the nanotubes during measurement sometimes leads to erratic viscosity measurements [19, 22].

Conductive nature of CNTs has made it possible to use electric conductivity measurements to investigate percolation behaviour of particles with respect to the filler concentration, dispersion quality, etc., both in liquid and solid states [4, 23, 24]. Dispersion state of CNTs controls interactions between nanotube clusters, hence affecting the electrical properties of the blend. It is generally accepted that a better CNT dispersion shows a higher electrical conductivity [4, 23]; nevertheless, intensive agglomeration of the nanotubes may result in the formation of interconnected networks with enhanced conductivity. Schultz *et al*. have shown that the insulator to conductor transition in the epoxy/CNT composites could be controlled by re-arranging CNT networks at a constant nanotube concentration.

However, most of the studies concerning the application of CNTs in polymer composites either ignore the dispersion assessment or rely on certain preliminary evaluations limited to a specific stage of the manufacturing process.

The purpose of our research is to address this deficiency by assessing the evolution of the CNT dispersion state during the entire composite preparation process, in a comparative fashion. This comparison is made using a stepwise analysis which is illustrated on two extreme cases of the dispersion morphology. The chosen systems for the analysis are epoxy based resins with CNTs that are identical in terms of the type and concentration of the components. The only difference is the storage time of the masterbatch. More specifically, CNTs used in the two systems were chosen from masterbatches of the same type, which were stored for a different time. The difference in aging led to a different agglomeration morphology, enabling us to establish the stepwise dispersion characterization in a comparative manner. However, the aging mechanism, as well as the effect of masterbatch aging on CNTs dispersion, although being observed in this work, are not by themselves the focus of the present study and demands another detailed investigation.

The characterizations were conducted in four stages, i.e.: CNT/epoxy masterbatch, diluted masterbatch, transition stage (during curing) and cured nanocomposite, as schematically shown in Figure 1. Such a detailed analysis provides information on the state of the CNT dispersion at each step, explicating different properties observed in the resulting nanocomposites. At each step, key factors that can influence CNT dispersion are discussed. The main purpose of this study is to emphasize the importance of a stepwise dispersion analysis in preparation of the nanocomposite, and to introduce a series of different methods, suited for characterization at each

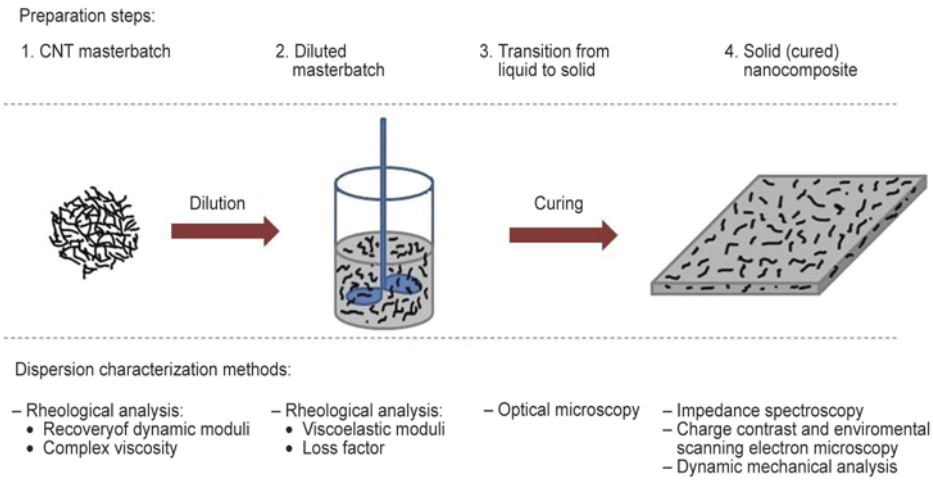

Figure 1. Schematic overview of the multistep characterization of the CNT dispersion state during preparation of CNT/epoxy nanocomposite

step. This will greatly facilitate the reproducibility of the results, which is currently one of the biggest challenges involved in manufacturing of CNT modified fibre reinforced composites.

2. Experimental

2.1. Materials

The epoxy monomer used in this work (Epikote 828LVEL) was a diglycidyl ether of bisphenol A (DGEBA). This was cured with 1,2-diaminocyclohexane (Dytek DCH-99) as hardener which was added to the resin at 15.2 phr (parts per hundred resin). Multi-wall carbon nanotubes (MWNTs) were supplied by Nanocyl in the form of highly concentrated, pre-dispersed mixtures (masterbatches) with a similar bisphenol-A epoxy resin (Epocyl NC R128-02). MWCNTs incorporated in this masterbatch have an average diameter of around 9 nm, a specific surface of 250–300 m^2/g and a carbon purity >90%.

For the study of the CNT dispersion two CNT/epoxy model systems were prepared based on the same type of materials with equal compositions. However, CNT masterbatches used in the two systems spent different times in storage. One system is prepared from a fresh (non-aged) version of the CNT masterbatch Epocyl NC R128-02. The other system is prepared from an older (aged) version of the same masterbatch, which was received and stored almost two years before the experiments. DSC analysis of the two systems does not show any trace of curing in the aged masterbatch. Melting endotherm observed in the DSC curve of the aged masterbatch, (Figure 2) indicates that during storage, the epoxy resin in the masterbatch mixture has been partially crystallized. As it is shown, this endotherm vanishes in the second temperature sweep. However, although both systems under study are thermally treated before the experiments are carried out, it seems that partial crystallization of the epoxy resin has significantly contributed to the agglomeration of carbon nanotubes in the aged system, where CNTs are repelled from the epoxy crystallites. In the text to follow non-aged and aged systems are to be referred to as 'N' and 'A', respectively. In both systems nanotube masterbatches were diluted with DGEBA epoxy so that a final CNT concentration of 0.3 wt% is attained. In order to homogenize the concentrated mixtures, prior to dilution, the masterbatches were thoroughly stirred using a marine type blade stirrer at 600 rpm for 10 minutes at room temperature. The same stirring procedure was repeated following dilution of the systems and the addition of the hardener. The blends were then degassed using a vacuum

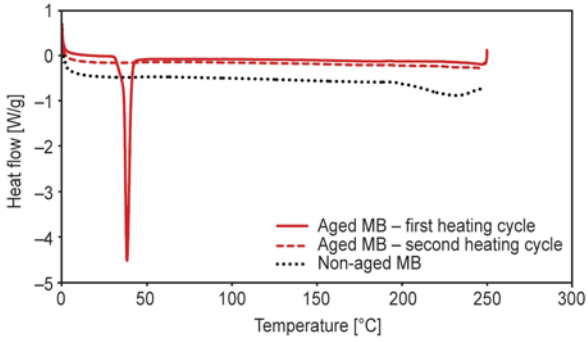

Figure 2. DSC Thermograms of the aged and non-aged masterbatches before thermal treatment, showing the first (solid line) and second (dashed line) heating cycles for the aged system

oven for 15 minutes. Solid samples were produced by pouring and then curing the resin mixtures in aluminum molds at 70°C for one hour followed by post curing at 140°C for another one and a half hours. The produced samples were then cut into the test specimens specified further.

2.2. Characterization methods

Rheological measurements at stage 1 and stage 2 (see Figure 1) were carried out at room temperature using an AR2000 rheometer, equipped with a 2° cone and plate geometry. The oscillation time sweep was performed at sufficiently low strain and angular frequency (ω) values of 0.5% and 0.5 rad/sec, to guarantee a linear behaviour. This oscillatory test was performed in order to investigate the structure recovery behaviour of the mixture through the measurement of the time evolution of shear storage modulus (G'), right after the sample experienced a pre-shear of 100 s^{-1} for two minutes.

Optical microscopy was used in order to observe the nanotubes behaviour during curing at stage 3. Imaging was carried out using an Olympus BHS Microscope. The samples of a few milligrams weight were put between two glass slides and placed in a Mettler FP82-HT hot stage. The micrographs were then obtained by a JVC TK-C1381 camera during the course of curing on time intervals of 5 seconds programmed through Qwin software from Leica Company.

Charge contrast scanning electron microscopy was carried out on the nanocomposite at stage 4 using a FEI NOVA Nanolab 600 microscope with a TLD (through the lens) detector. This was done on 5 μm thick sections which were cut from the solid cured samples using a Leica Ultracut UCT microtome. No conductive layer was coated on the films so as to take advantage of the contrast effect in electron charging (or 'voltage contrast') of the sample surface. This made it possible to have an in depth view into the cured film so that the nanotubes embedded in the resin film could be observed.

Environmental Scanning Electron Microscopy (ESEM) micrographs were captured from the solid nanocomposite samples using a Philips ESEM XL30. Multiple images taken from each sample were then digitally combined into one single larger image, in order to observe a wider region. The images were taken with sufficient overlap so that the stitching is done more accurately.

The electrical properties of the nanocomposite samples were measured at stage 4 by means of a Solartron Frequency Analyzer SI 1225 together with a Solartron Electrochemical Interface SI 1287. Measurements were carried out at frequencies ranging from 0.1 to 106 Hz with a constant amplitude of 2 V and a DC potential of 0.4 V. Samples with a dimension of 1 mm×10 mm×10 mm were cut and then the two surfaces of each sample were covered with a conductive silver paint.

Glass transition temperature (T_g) of the samples were identified at stage 4 using a dynamic mechanical analyzer (TA-Instruments DMA Q800 V 7.5). The analyses were carried out by heating the samples from 25 to 250°C with a heating rate of 3°C/min using dual cantilever clamps at a frequency of 1 Hz. Similar to the three point bending loading mode, it is possible to make reliable T_g measurements using a dual cantilever fixture [25]. Samples for this measurement were in the form of rectangular pieces of 3.5 mm thickness, 35 mm length and 11.5 mm width.

3. Results and discussion

3.1. Masterbatch (stage 1)

Highly concentrated CNT/resin mixtures (masterbatches) are nowadays widely used both at laboratory and industrial scales to facilitate the processing of nanocomposite materials [26–28]. Although the increased viscosity of the CNT masterbatch can limit diffusion and sedimentation of CNTs by restricting the Brownian motions, reduced distances between the nanotubes at high loadings can give rise to the strong attractive forces, leading to further agglomeration of CNTs during sufficiently long storage periods. Recovery of the storage and loss moduli of the two concentrated (masterbatch) systems after they were subjected to a pre-shear of a 100 s^{-1} for two minutes are shown in Figure 3a. Such a high pre-shear is able to destroy looser clusters of CNTs [20, 29].

Both systems reflect a solid-like behaviour as $G' > G''$. Moreover, a significantly higher shear storage modulus for the aged masterbatch compared to the fresh one, observed throughout the recovery period, represents a much more pronounced elastic contribution. This indicates a stronger interaction between the nanotubes in case of the aged system where apparently a more robust network of CNT agglomerates exist. Moreover, the fresh masterbatch represents an obvious recovery over time for G' (a factor

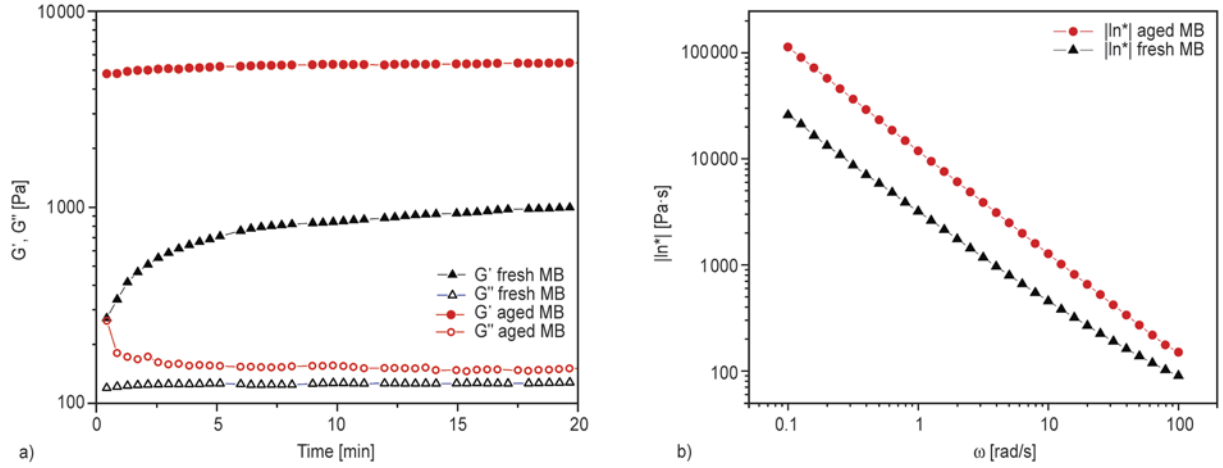

Figure 3. Rheological behaviour the aged (circles) and fresh (triangles) CNT masterbatches: a) recovery of the storage, G' (solid symbols) and loss, G'' (closed symbols) moduli as a function of time following a pre-shear of 100 s^{-1} for two minutes; b) log-log plot of the complex viscosity, $|\eta^*|$, vs angular frequency

of 3), whereas in case of the aged version the corresponding recovery is smaller and faster. This suggests that CNT agglomerates (agglomerate network) existing in the aged masterbatch, are either very difficult to break under the applied pre-shear or restructure extremely fast as soon as the shearing is ceased. The complex viscosity of the aged system also shows higher values in the whole frequency range from 100 to 0.1 rad/s, being more considerable at lower frequencies (Figure 3b). This indicates that the motion of the matrix molecules is more restricted in the aged masterbatch which confirms the findings in the oscillatory recover analysis.

3.2. Diluted masterbatch (stage 2)

The concentrated masterbatch mixtures were diluted under shear mixing to the final CNT concentration of 0.3 wt%. This will be the ultimate concentration of nanotubes in the final composite material. It has been previously reported that the matrix preparation process can largely affect the dispersion of CNTs both before and after the curing process. For instance, Schulz *et al.* [9] showed that application of a high pre-shear can even enhance the agglomeration and network formation of CNTs during the following mixing steps, due to the so called shear induced nanotube agglomerate formation. Mixing time, intensity, and temperature are amongst the other important processing parameters that can influence the agglomerate formation at this stage [7, 8, 22]. In these works it has been proven that the dispersion state of the nanotubes after completion of the curing process depends greatly on their dispersion quality at the resin preparation level; Therefore, evaluation of the dispersion quality following the resin preparation step is deemed necessary, even if the initial CNT masterbatch is well mixed. In the present work we take advantage of the accuracy and sensitivity of the rheological analysis to characterize the dispersion/agglomeration state of CNTs.

Characteristics of the microstructure and dispersion state of a suspension can be revealed by measuring the low and high frequency viscoelastic moduli [21, 22]. Figure 4a presents linear viscoelastic storage and loss shear moduli of the diluted samples as a function of frequency.

Significant differences are observed in the viscoelastic behaviour of the two systems. Shear moduli of the 'A' system are considerably higher than that of the 'N' system. Furthermore, the storage modulus (G') of the resin system 'A' (solid circles) develops a plateau at low frequencies ($\omega \rightarrow 0$). A frequency independent rubbery plateau of G' is caused by highly interacting nanotubes, and is a well-known characteristic of a network or a structured entanglement in the suspending medium [21, 30, 31]. This, together with a loss modulus (G'') remaining lower than G' all over the swept frequency range, indicates the presence of a network of entangled CNT clusters with a pseudo–solid-like behaviour. This situation is quite comparable to the cases where a solid-like gel network is emerged following an increase in the nanofiller content as observed in [21, 30].

In contrast, the diluted 'N' resin system represents the typical hallmarks of a liquid-like material with a perfectly linear $G''(\omega)$ staying higher than G' over a wide range of frequencies. The crossover of G' and G'' at 50 rad/s shows that an interconnected network

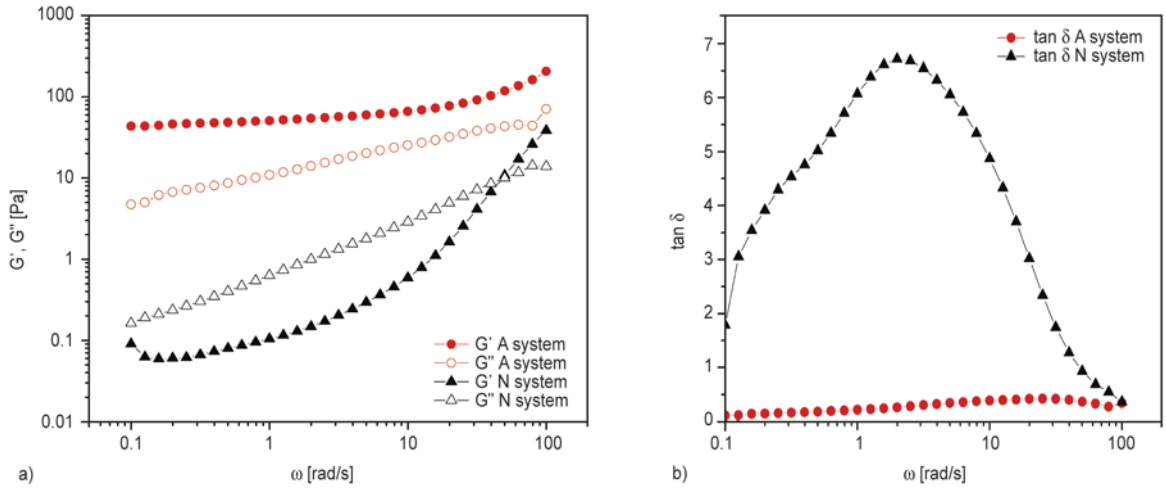

Figure 4. Rheological behaviour of the aged (circles) and non-aged (triangle) CNT (diluted to 0.3 wt% CNT) samples at 70°C. a) Storage, G' (solid symbols) and loss, G'' (closed symbols) moduli as a function of angular frequency; b) Loss factor, tan δ, against angular frequency

of the CNTs is formed only at higher frequencies. At this point, the initially dispersed agglomerates entangle with each other and thenceforth a dominantly elastic (rather than viscous) behaviour is observed [32].

An even more pronounced distinction between the two types of samples can be made through the evaluation of the corresponding loss factor, tan δ (= G''/G'), as a function of frequency (Figure 4b) obtained from the dynamic moduli presented in Figure 4a. The variations in the intensity of the peak value of tan δ can be employed as an effective empirical measure to quantify nanotube dispersion state in a liquid matrix [22]. A better dispersed system normally exhibits a higher peak value (or tan δ in general), which here is the case for the 'N' system. This is due to the fact that the storage modulus, G', of the system with better dispersed CNTs is most often lower than that of a poorly dispersed system, as it was also the case in our system (Figure 4a) where the 'A' system exhibits a more solid-like behaviour. Lower tan δ values observed in the 'A' system again imply its enhanced elastic properties compared to the 'N' system. Such a difference between viscoelastic properties of the two diluted systems may originate from the distinct elasticity of the entangled nanotube clusters at the masterbatch level, where stronger interactions were found in the 'A' system. Our observations at this stage indicate that the shear forces applied during the dilution step were not sufficient to homogenize the dispersion including the aged CNT masterbatch, so that a solid-like behaviour induced by an interconnected network of CNT agglomerates still persists.

3.3. Transition from liquid to solid (stage 3)

Addition of the hardener and the subsequent curing reaction can both independently provoke further agglomeration (reagglomeration) of the nanotubes in an epoxy/CNT resin system [7, 16, 19, 33]. This type of reagglomeration is sometimes referred to as 'secondary agglomeration' so as to differentiate it from the primary or initial agglomeration, normally existing in the dry un-processed (raw) bulk CNTs [7, 10]. Addition of hardener can enhance CNT reagglomeration by lowering the viscosity and hence increasing the mobility of the nanotubes, even at the same temperature and before the onset of curing [16]. Furthermore, hardener can enhance ionic concentration of the dispersion, thereby leading to a reduction in the stability of the dispersion [33]. Curing temperature plays a very important role in nanoparticle reaggregation and cluster formation, as it can control the mobility of the particles by altering the matrix viscosity as well as the kinetics of the curing reaction. A trade-off exists between viscosity and curing rate as both are differently affected by temperature. A lower curing temperature will cause prolonged gelation times, so that nanoparticles (or local clusters) will have more time to organize themselves into agglomerated structures. However, this process will be slower here due to the higher viscosity of the system in comparison with curing at higher temperatures. Higher curing temperatures on

the other hand, can create the same effect by boosting the mobility of the particles and lowering the viscosity; but instead, the onset of gelation will arrive faster. Rheological evidence discussed in the previous sections, already revealed possible presence of an interconnected network-like CNT structure with considerable elastic contribution in the 'A' resin system (Figure 4). In this part of the analysis, morphological evolution of the two systems under study was monitored during the curing reaction using an optical microscope equipped with a heating element. Figure 5a–5d shows the optical micrographs obtained right before and after the curing reaction.

The difference between the microstructure of the two systems prior to curing (Figure 5a and 5c) is already visible. CNT clusters in the non-aged system (Figure 5c), look denser (and hence darker) while the ones in the aged system (Figure 5a) look swollen and further pushed into each other in such a way that the boundaries of the clusters are less distinguishable. This can be due to gradual resin diffusion during storage. Partial crystallization of the epoxy resin in the aged-CNT masterbatch, (Fig-

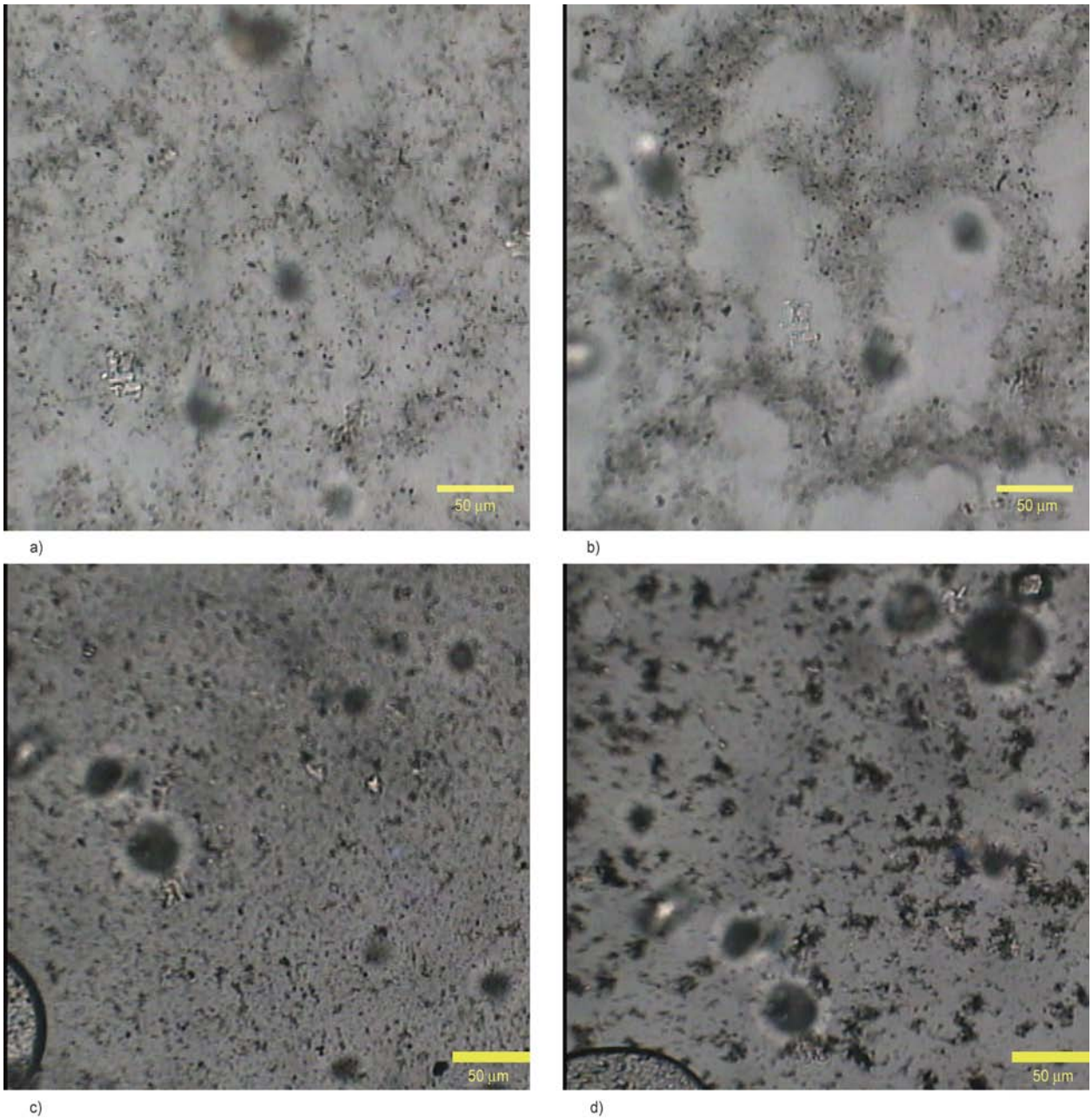

Figure 5. Optical micrographs of the 0.3 wt% diluted CNT/epoxy suspensions during curing following the addition of hardener at 70°C for: system 'A' before (a) and after (b) curing and system 'N' before (c) and after (d) curing. Images have a 50 µm scale bar

ure 2) as discussed in section 2.1, seems to be responsible for the non-homogeneity in CNT dispersion at this stage, as can be seen in Figure 5a.

As a result of the curing reaction, the tenuous structure of the aged CNT clusters in 'A' system (Figure 5a) is transformed into a more robust three dimensional interconnected network with clear and well defined borders (Figure 5b). This is markedly different from the micro-structure of the 'N' system after curing reaction (Figure 5d). In this case, further aggregation of the clusters apparently did not lead to the formation of any macroscopic network being observed in the former case (Figure 5b). Instead, homogenously dispersed initial clusters have slightly grown into the individually distinguishable larger clusters. The higher contrast of these local clusters with the background might suggest a higher packing density of CNTs inside the agglomerates, in comparison with the lower contrast interconnected network of the 'A' system.

3.4. Solid (cured) nanocomposite (stage 4)

Upon completion of the curing reaction, the final microstructure of the nanotubes will be frozen by the reaction induced glass transition. Characterization of the resulting nanocomposite matrix can provide important information about the dispersion quality of CNTs in the solid state.

Due to the conductive nature of the CNTs the conductivity measurement is currently considered a popular technique for quantitative evaluation of the CNT dispersion or network formation; especially to determine the electrical percolation of the nanofillers upon increasing the filler concentration [23, 34]. Electrical percolation is identified by a sudden rise of several orders of magnitude in conductivity as a function of the volume fraction of the filler particles.

Figure 6 compares specific conductivity of the two samples, as a function of frequency.

The graphs are obtained using the modulus of the complex admittance function, calculated based on the AC impedance spectroscopy results of the samples at room temperature [23]. The sample containing aged CNT demonstrates specific conductivity values of about five orders of magnitude higher than that of the 'N' sample at the lowest registered frequencies. Comparable to the results of our previous rheological analysis, where a partial mechanical percolation was identified in the 'A' system at

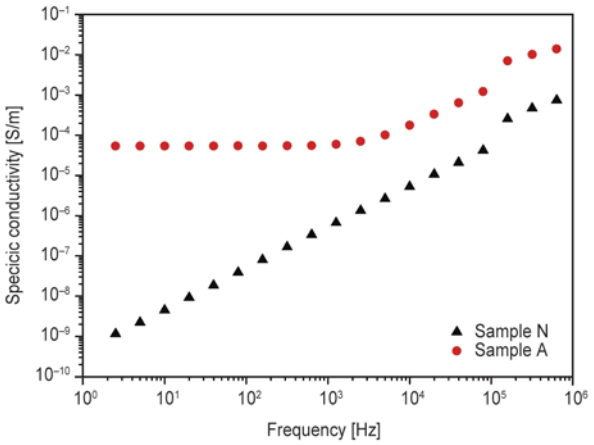

Figure 6. Log-log plot of the specific conductivity versus frequency of the cured 'A' (circles) and 'N' (squares) nanocomposites, measured at room temperature

stage 2 (diluted masterbatch, Figure 4a), here at stage 4, the cured film of the same system reveals a frequency independent specific conductivity at lower frequencies ($< 10^3$ Hz). This is a typical response of a percolated system in which conductive fillers created electrically connected pathways throughout the sample's thickness [23, 24, 33]. However, the frequency dependent increase in the specific conductivity observed at higher frequencies implies that this system is not fully percolated [24]. On the other hand, specific conductivity of the 'N' system monotonically increases with frequency. Such a linear frequency dependent increase in conductivity is a characteristic of highly resistive materials. In fact the slope of unity observed on the log-log plot for this sample, can be explained by the expression $\sigma = \omega\varepsilon'\varepsilon_0$ which is used for dielectric materials [23] (where σ: conductivity, ε': real part of the dielectric constant, ω: angular frequency and ε_0: vacuum permittivity). This is in fair agreement with our previous microscopic observations where formation of a network like morphology in the 'A'system was verified.

Charge contrast SEM images shown in Figure 7a and 7b can provide better visualization of the nanotubes within the epoxy matrix.

In this technique the inherent difference between the charging potential of the conductive CNTs and the dielectric matrix will give rise to a charging contrast [12, 20, 35]. Using a right detector (as explained in the experimental section), such a contrast will make it possible to gain some insights into the placement of the nanoparticles embedded in the matrix. Clusters of highly entangled nanotubes could read-

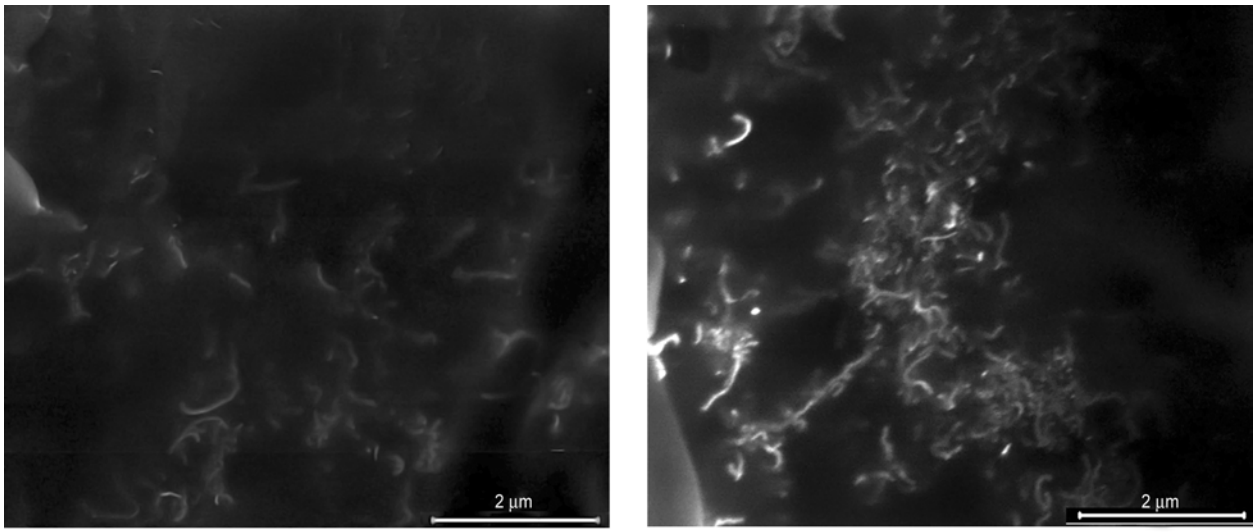

Figure 7. Charge contrast SEM micrographs of the cured a) 'N' and b) 'A' nanocomposites. Both images were taken at 35 000× magnification and have a 2 µm scale bar

ily be identified in these micrographs. The 'A' system distinguishes itself from the other system by larger localized clusters while a more homogenous state of dispersion can be observed in the 'N' system.

Dispersion morphology of CNTs in the two systems, could be compared at a larger scale using multiple ESEM images stitched together in Figure 8a and 8b. Although unlike the charge contrast SEM, here the CNTs embedded in the matrix are not completely visible; one still can clearly observe large agglomerates of CNTs in the 'A' system (bright clusters), while this is not the case in the 'N' system, where isolated CNT aggregates are far apart.

Thermo-mechanical properties of the solid matrix materials were measured by DMA over a range of temperature. Figure 9 shows damping coefficient, $\tan\delta$, of the epoxy/CNT nanocomposites as well as the neat sample as a function of temperature. The major peak position of $\tan\delta$, which corresponds to the alpha relaxation or the glass transition temperature, T_g, shows the highest value for the neat epoxy resin. T_g value of the 'A' system is only slightly lower than that of the neat epoxy while in case of the 'N' system a considerable decrease of about 26°C is observed.

Effect of CNTs on the glass transition temperature of epoxy resins is controversial and a concrete conclusion based on the available data could hardly be made. Allaoui and El Bouina [36], have summarized some of the available results in a review paper.

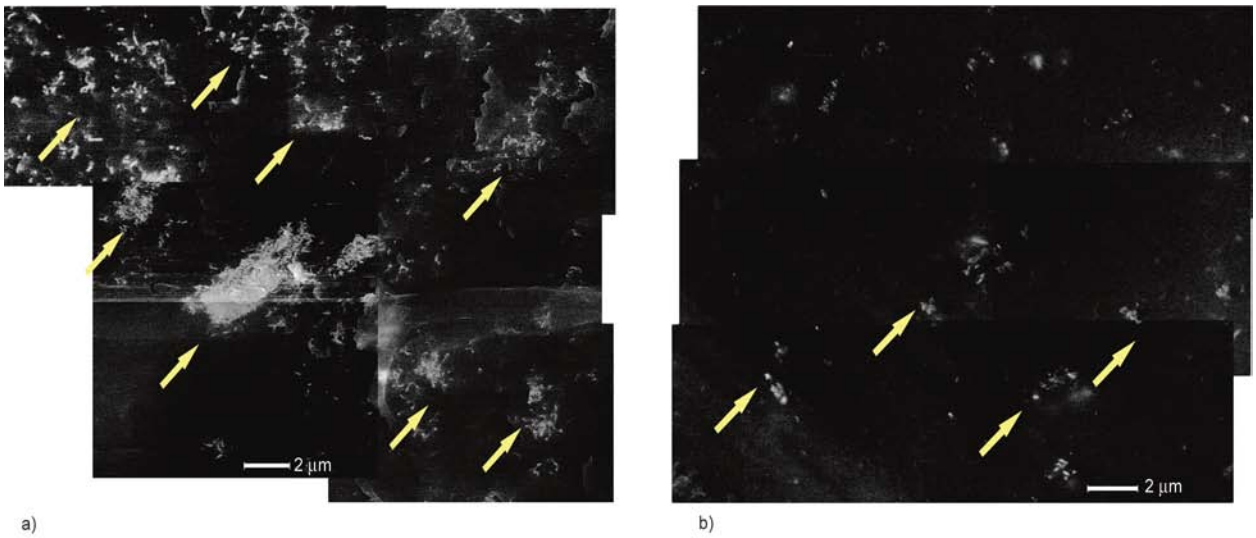

Figure 8. Stitched ESEM micrographs of the cured a) 'A' and b) 'N' nanocomposites. All images were taken at 10 000× magnification and have a 2 µm scale bar. Arrows indicate CNT agglomerates.

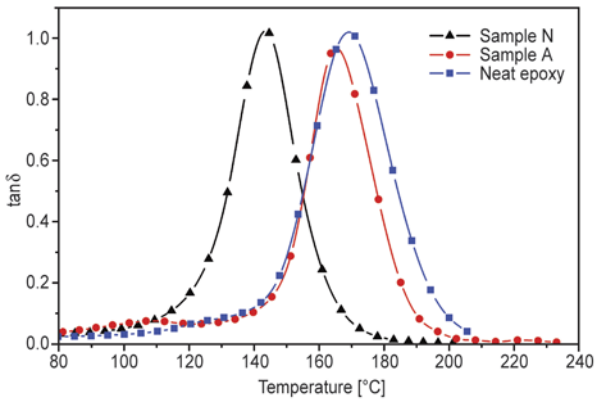

Figure 9. Tan δ versus temperature of the cured neat epoxy (squares) and 'A' (circles) and 'N' (triangles) nanocomposites, obtained by DMA at a frequency of 1 Hz

Most of the reported results suggest an increase or almost no change in the T_g values [16, 19, 37–41] while some reductions have also been reported [42, 43]. Such inconsistent results are attributed to a complex simultaneous influence of various parameters such as aspect ratio, functionality, packing density and purity (presence of metallic catalysts) of the nanotubes. Type and stoichiometric ratio of epoxy/hardener system as well as rheological properties of the CNT containing resin are also of great importance. Specific composite processing and curing condition can control the fate of the composite material in favor of some of these competing factors.

It can be elucidated from Figure 9 that a better dispersion of the CNTs results in a lower T_g which seems to be caused by a reduced curing degree of the 'N' system. A possible explanation is that the catalytic effect of CNTs on curing [43, 44] expedites the second stage of the epoxy curing reaction which is dominantly diffusion-controlled. This results in a lower crosslinking degree and hence a lower T_g. It is also likely that individual CNTs block the reaction sites in the epoxy monomer; consequently, a better dispersed system more dominantly hinders the curing reaction. This will have the same effect on the crosslinking degree as well as the glass transition temperature. This can result in a lower crosslinking degree, thus reducing the T_g of the cured epoxy. Kim *et al*. [45] even took advantage of the CNTs hindering effect on epoxy curing as a means of assessing the state of dispersion.

There is no doubt that dispersion evaluation techniques are not limited to those employed in this study; however, it was impossible (and perhaps not necessary) to cover all of the techniques reported in the literature in a single report. Instead, these methods were chosen in view to collect the most important information regarding the dispersion state of CNTs in each step. Moreover, the assessment methods employed at each step of the work, could be performed in more detail provided that more in depth information is desired. In such cases, interested reader is referred to the relevant references provided in each section of this study.

4. Conclusions

1. A methodology for the multi-step characterization of the CNT dispersion state at different stages of the nanocomposite preparation was developed. It enabled us to investigate the evolution of the CNT dispersion in the initial masterbatch, diluted masterbatch, during transition to the solid (cured) state and in the final cured nanocomposite.
2. This methodology was applied to two CNT containing epoxy based systems with extreme cases of dispersion morphologies. These different dispersion morphologies were induced by storing the CNT masterbatches for a different time.
3. Characterizations performed on the two systems revealed that fresh CNT masterbatch exhibits a transition from a solid-like to a dominantly liquid-like behaviour upon dilution, as expected; while the aged masterbatch keeps behaving dominantly solid-like after dilution. Following curing reaction, the aged system showed orders of magnitude higher electrical conductivity owing to the partial percolation of CNTs together with a higher T_g in comparison with the non-aged system.
4. The underlying cause for such distinct behaviour was found to originate from very different structures of the two systems. The existence of a highly interacting microstructure in the aged system was evident from the early stages of the stepwise characterization. This was later on evolved into a clearly visible network of CNT agglomerates during curing reaction. The footsteps of this network were identified in the postcuring solid state, where an electrical percolation induced by this network was detected. A correlation between the electrical conductivity measurements of the cured material and rheological analysis of the liquid resin was then elucidated. The results obtained in different steps of the dispersion characterization

were always consistent and in good agreement with the morphological observations.

5. Various factors are able to independently control and alter the dispersion state of nanotubes during the nanocomposite manufacturing process. This work emphasizes the necessity of a stepwise evaluation of the dispersion quality so as to enhance reproducibility in manufacturing CNT/epoxy nanocomposites with specific physical, thermal, electrical and mechanical properties.

Acknowledgements

The work was performed in the scope of the GOA/10/004 project 'New model-based concepts for nanoengineered polymer composites', funded by the Research Council of KU Leuven. Collaboration between KULeuven and Nanocyl S.A was performed under the framework agreement between the Department MTM, KULeuven and Nanocyl S.A. Collaboration with the Department of Chemistry and the Department of Chemical Engineering (CIT Lab.) within the framework of the Materials Research Center at KU Leuven is gratefully acknowledged.

References

[1] Joshi S. C., Dikshit V.: Enhancing interlaminar fracture characteristics of woven CFRP prepreg composites through CNT dispersion. Journal of Composite Materials, **46**, 665–675 (2012).
DOI: 10.1177/0021998311410472

[2] da Costa E. F. R., Skordos A. A., Partridge I. K., Rezai A.: RTM processing and electrical performance of carbon nanotube modified epoxy/fibre composites. Composites Part A: Applied Science and Manufacturing, **43**, 593–602 (2012).
DOI: 10.1016/j.compositesa.2011.12.019

[3] Domingues D., Logakis E., Skordos A. A.: The use of an electric field in the preparation of glass fibre/epoxy composites containing carbon nanotubes. Carbon, **50**, 2493–2503 (2012).
DOI: 10.1016/j.carbon.2012.01.072

[4] Song Y. S., Youn J. R.: Influence of dispersion states of carbon nanotubes on physical properties of epoxy nanocomposites. Carbon, **43**, 1378–1385 (2005).
DOI: 10.1016/j.carbon.2005.01.007

[5] Gkikas G., Barkoula N-M., Paipetis A. S.: Effect of dispersion conditions on the thermo-mechanical and toughness properties of multi walled carbon nanotubes-reinforced epoxy. Composites Part B: Engineering, **43**, 2697–2705 (2012).
DOI: 10.1016/j.compositesb.2012.01.070

[6] Coleman J. N., Khan U., Blau W. J., Gun'ko Y. K.: Small but strong: A review of the mechanical properties of carbon nanotube–polymer composites. Carbon, **44**, 1624–1652 (2006).
DOI: 10.1016/j.carbon.2006.02.038

[7] Alig I., Pötschke P., Lellinger D., Skipa T., Pegel S., Kasaliwal G. R., Villmow T.: Establishment, morphology and properties of carbon nanotube networks in polymer melts. Polymer, **53**, 4–28 (2012).
DOI: 10.1016/j.polymer.2011.10.063

[8] Schulz S. C., Faiella G., Buschhorn S. T., Prado L. A. S. A., Giordano M., Schulte K., Bauhofer W.: Combined electrical and rheological properties of shear induced multiwall carbon nanotube agglomerates in epoxy suspensions. European Polymer Journal, **47**, 2069–2077 (2011).
DOI: 10.1016/j.eurpolymj.2011.07.022

[9] Schulz S. C., Schlutter J., Bauhofer W.: Influence of initial high shearing on electrical and rheological properties and formation of percolating agglomerates for MWCNT/epoxy suspensions. Macromolecular Materials and Engineering, **295**, 613–617 (2010).
DOI: 10.1002/mame.201000065

[10] Alig I., Skipa T., Lellinger D., Pötschke P.: Destruction and formation of a carbon nanotube network in polymer melts: Rheology and conductivity spectroscopy. Polymer, **49**, 3524–3532 (2008).
DOI: 10.1016/j.polymer.2008.05.037

[11] Siegfried M., Tola C., Claes M., Lomov S. V., Verpoest I., Gorbatikh L.: Impact and residual after impact properties of carbon fiber/epoxy composites modified with carbon nanotubes. Composite Structures, **111**, 488–496 (2014).
DOI: 10.1016/j.compstruct.2014.01.035

[12] Kovács J. Z., Andresen K., Pauls J. R., Garcia C. P., Schossig M., Schulte K., Bauhofer W.: Analyzing the quality of carbon nanotube dispersions in polymers using scanning electron microscopy. Carbon, **45**, 1279–1288 (2007).
DOI: 10.1016/j.carbon.2007.01.012

[13] Schlea M. R., Brown T. R., Bush J. R., Criss Jr J. M., Mintz E. A., Shofner M. L.: Dispersion control and characterization in multiwalled carbon nanotube and phenylethynyl-terminated imide composites. Composites Science and Technology, **70**, 822–828 (2010).
DOI: 10.1016/j.compscitech.2010.01.019

[14] Li W., Bauhofer W.: Imaging of CNTs in a polymer matrix at low accelerating voltages using a SEM. Carbon, **49**, 3891–3898 (2011).
DOI: 10.1016/j.carbon.2011.05.027

[15] Luo Z. P., Koo J. H.: Quantitative study of the dispersion degree in carbon nanofiber/polymer and carbon nanotube/polymer nanocomposites. Materials Letters, **62**, 3493–3496 (2008).
DOI: 10.1016/j.matlet.2008.03.010

[16] Chakraborty A., Plyhm T., Barbezat M., Necola A., Terrasi G. P.: Carbon nanotube (CNT)–epoxy nanocomposites: A systematic investigation of CNT dispersion. Journal of Nanoparticle Research, **13**, 6493–6506 (2011).
DOI: 10.1007/s11051-011-0552-3

[17] Ma P-C., Mo S-Y., Tang B-Z., Kim J-K.: Dispersion, interfacial interaction and re-agglomeration of functionalized carbon nanotubes in epoxy composites. Carbon, **48**, 1824–1834 (2010).
DOI: 10.1016/j.carbon.2010.01.028

[18] Li J., Ma P. C., Chow W. S., To C. K., Tang B. Z., Kim J-K.: Correlations between percolation threshold, dispersion state, and aspect ratio of carbon nanotubes. Advanced Functional Materials, **17**, 3207–3215 (2007).
DOI: 10.1002/adfm.200700065

[19] Rahatekar S. S., Koziol K. K. K., Butler S. A., Elliott J. A., Shaffer M. S. P., Mackley M. R., Windle A. H.: Optical microstructure and viscosity enhancement for an epoxy resin matrix containing multiwall carbon nanotubes. Journal of Rheology, **50**, 599–610 (2006).
DOI: 10.1122/1.2221699

[20] Battisti A., Skordos A. A., Partridge I. K.: Monitoring dispersion of carbon nanotubes in a thermosetting polyester resin. Composites Science and Technology, **69**, 1516–1520 (2009).
DOI: 10.1016/j.compscitech.2008.05.012

[21] Galindo-Rosales F. J., Moldenaers P., Vermant J.: Assessment of the dispersion quality in polymer nanocomposites by rheological methods. Macromolecular Materials and Engineering, **296**, 331–340 (2011).
DOI: 10.1002/mame.201000345

[22] Huang Y. Y., Ahir S. V., Terentjev E. M.: Dispersion rheology of carbon nanotubes in a polymer matrix. Physical Review B, **73**, 125422/1–125422/9 (2006).
DOI: 10.1103/PhysRevB.73.125422

[23] Sandler J. K. W., Kirk J. E., Kinloch I. A., Shaffer M. S. P., Windle A. H.: Ultra-low electrical percolation threshold in carbon-nanotube-epoxy composites. Polymer, **44**, 5893–5899 (2003).
DOI: 10.1016/S0032-3861(03)00539-1

[24] Thakre P. R., Bisrat Y., Lagoudas D. C.: Electrical and mechanical properties of carbon nanotube-epoxy nanocomposites. Journal of Applied Polymer Science, **116**, 191–202 (2010).
DOI: 10.1002/app.31122

[25] Deng S., Hou M., Ye L.: Temperature-dependent elastic moduli of epoxies measured by DMA and their correlations to mechanical testing data. Polymer Testing, **26**, 803–813 (2007).
DOI: 10.1016/j.polymertesting.2007.05.003

[26] Mičušík M., Omastová M., Krupa I., Prokeš J., Pissis P., Logakis E., Pandis C., Pötschke P., Pionteck J.: A comparative study on the electrical and mechanical behaviour of multi-walled carbon nanotube composites prepared by diluting a masterbatch with various types of polypropylenes. Journal of Applied Polymer Science, **113**, 2536–2551 (2009).
DOI: 10.1002/app.30418

[27] De Greef N., Gorbatikh L., Godara A., Mezzo L., Lomov S. V., Verpoest I.: The effect of carbon nanotubes on the damage development in carbon fiber/epoxy composites. Carbon, **49**, 4650–4664 (2011).
DOI: 10.1016/j.carbon.2011.06.047

[28] Wichmann M. H. G., Sumfleth J., Fiedler B., Gojny F. H., Schulte K.: Multiwall carbon nanotube/epoxy composites produced by a masterbatch process. Mechanics of Composite Materials, **42**, 395–406 (2006).
DOI: 10.1007/s11029-006-0050-3

[29] Bauhofer W., Schulz S. C., Eken A. E., Skipa T., Lellinger D., Alig I., Tozzi E. J., Klingenberg D. J.: Shear-controlled electrical conductivity of carbon nanotubes networks suspended in low and high molecular weight liquids. Polymer, **51**, 5024–8027 (2010).
DOI: 10.1016/j.polymer.2010.09.013

[30] Chapartegui M., Markaide N., Florez S., Elizetxea C., Fernandez M., Santamaría A.: Specific rheological and electrical features of carbon nanotube dispersions in an epoxy matrix. Composites Science and Technology, **70**, 879–884 (2010).
DOI: 10.1016/j.compscitech.2010.02.008

[31] Trappe V., Weitz D. A.: Scaling of the viscoelasticity of weakly attractive particles. Physical Review Letters, **85**, 449–452 (2000).
DOI: 10.1103/PhysRevLett.85.449

[32] Fan Z., Advani S. G.: Rheology of multiwall carbon nanotube suspensions. Journal of Rheology, **51**, 585–604 (2007).
DOI: 10.1122/1.2736424

[33] Martin C. A., Sandler J. K. W., Shaffer M. S. P., Schwarz M-K., Bauhofer W., Schulte K., Windle A. H.: Formation of percolating networks in multi-wall carbon-nanotube–epoxy composites. Composites Science and Technology, **64**, 2309–2316 (2004).
DOI: 10.1016/j.compscitech.2004.01.025

[34] Moisala A., Li Q., Kinloch I. A., Windle A. H.: Thermal and electrical conductivity of single- and multi-walled carbon nanotube-epoxy composites. Composites Science and Technology, **66**, 1285–1288 (2006).
DOI: 10.1016/j.compscitech.2005.10.016

[35] Loos J., Alexeev A., Grossiord N., Koning C. E., Regev O.: Visualization of single-wall carbon nanotube (SWNT) networks in conductive polystyrene nanocomposites by charge contrast imaging. Ultramicroscopy, **104**, 160–167 (2005).
DOI: 10.1016/j.ultramic.2005.03.007

[36] Allaoui A., El Bounia N-E.: How carbon nanotubes affect the cure kinetics and glass transition temperature of their epoxy composites? – A review. Express Polymer Letters, **3**, 588–594 (2009).
DOI: 10.3144/expresspolymlett.2009.73

[37] Guadagno L., De Vivo B., Di Bartolomeo A., Lamberti P., Sorrentino A., Tucci V., Vertuccio L., Vittoria V.: Effect of functionalization on the thermo-mechanical and electrical behavior of multi-wall carbon nanotube/epoxy composites. Carbon, **49**, 1919–1930 (2011). DOI: 10.1016/j.carbon.2011.01.017

[38] Guadagno L., Vertuccio L., Sorrentino A., Raimondo M., Naddeo C., Vittoria V., Iannuzzo G., Calvi E., Russo S.: Mechanical and barrier properties of epoxy resin filled with multi-walled carbon nanotubes. Carbon, **47**, 2419–2430 (2009). DOI: 10.1016/j.carbon.2009.04.035

[39] Jin F-L., Ma C-J., Park S-J.: Thermal and mechanical interfacial properties of epoxy composites based on functionalized carbon nanotubes. Materials Science and Engineering: A, **528**, 8517–8522 (2011). DOI: 10.1016/j.msea.2011.08.054

[40] Prolongo S. G., Gude M. R., Ureña A.: The curing process of epoxy/amino-functionalized MWCNTs: Calorimetry, molecular modelling, and electron microscopy. Journal of Nanotechnology, **2010**, 420432/1–420432/11 (2010). DOI: 10.1155/2010/420432

[41] Hsieh T. H., Kinloch A. J., Taylor A. C., Kinloch I. A.: The effect of carbon nanotubes on the fracture toughness and fatigue performance of a thermosetting epoxy polymer. Journal of Materials Science, **46**, 7525–7535 (2011). DOI: 10.1007/s10853-011-5724-0

[42] Tao K., Yang S., Grunlan J. C., Kim Y-S., Dang B., Deng Y., Thomas R. L., Wilson B. L., Wei X.: Effects of carbon nanotube fillers on the curing processes of epoxy resin-based composites. Journal of Applied Polymer Science, **102**, 5248–5254 (2006). DOI: 10.1002/app.24773

[43] Zhou T., Wang X., Liu X., Xiong D.: Influence of multi-walled carbon nanotubes on the cure behavior of epoxy-imidazole system. Carbon, **47**, 1112–1118 (2009). DOI: 10.1016/j.carbon.2008.12.039

[44] Siddiqui N. A., Khan S. U., Ma P. C., Li C. Y., Kim J-K.: Manufacturing and characterization of carbon fibre/epoxy composite prepregs containing carbon nanotubes. Composites Part A: Applied Science and Manufacturing, **42**, 1412–1420 (2011). DOI: 10.1016/j.compositesa.2011.06.005

[45] Kim S. H., Lee W. I., Park J. M.: Assessment of dispersion in carbon nanotube reinforced composites using differential scanning calorimetry. Carbon, **47**, 2699–2703 (2009). DOI: 10.1016/j.carbon.2009.05.026

eXPRESS Polymer Letters Vol.8, No.8 (2014) 609–617
Available online at www.expresspolymlett.com
DOI: 10.3144/expresspolymlett.2014.64

Polylactide/poly(hydroxybutyrate-co-hydroxyvalerate) blends: Morphology and mechanical properties

T. Gerard[1], *T. Budtova*[1], *A. Podshivalov*[2], *S. Bronnikov*[3*]

[1]Mines ParisTech, Centre de Mise en Forme des Matériaux (CEMEF), UMR CNRS 7635, BP 207, 06904 Sophia Antipolis, France
[2]National Research University of Information Technologies, Mechanics and Optics, Kronverkskiy Prospekt 49, 197101 St. Petersburg, Russian Federation
[3]Russian Academy of Science, Institute of Macromolecular Compounds, Bolshoi Prospekt 31, 199004 St. Petersburg, Russian Federation

Received 10 March 2014; accepted in revised form 27 April 2014

Abstract. The morphology and the mechanical properties of polylactide/poly(hydroxybutyrate-co-hydroxyvalerate) blends of various compositions were studied. The statistical analysis of the scanning electron microscopy images allowed finding two statistical ensembles of the minor-phase particles. The first ensemble involves the dispersed particles, whereas the second one contains the coalesced particles. The mean diameters of both dispersed and coalesced minor-phase particles were calculated and plotted against the blend composition. Young's modulus, tensile strength, elongation at break, and Charpy impact strength of the blends were determined and examined as a function of the blend composition. The Young's modulus values were shown to be in accordance with theoretical predictions.

Keywords: *polymer blends and alloys, polylactide, polyhydroxyalkanoate, morphology, mechanical properties*

1. Introduction

Polylactide (PLA) is one of the most widespread biomass-based, biodegradable (compostable) and biocompatible polymers [1, 2]. It is water-insoluble, can be either transparent or semi-transparent depending on polymer crystallinity, and optically active [1, 3]. It can be processed as a conventional thermoplastic polymer. PLA is used for packaging materials, in agriculture, in textile industry (fibers), in medicine (scaffolds), and in pharmacology (drug delivery systems) [1, 3]. The main drawbacks of PLA are high brittleness, slow crystallization rate, and high permeability to gases. The ways for overcoming these problems are to use plasticizers, copolymerization with other components, making composites, and blending with other polymers [1, 4]. The latter allows fabrication of new materials with improved/modified properties. Besides, this way is less expensive than chemical modification or synthesis of tailor-made polymers.

If willing to keep PLA-based system fully biodegradable and biocompatible, the second component should also possess these properties. Polyhydroxyalkanoates, aliphatic polyesters, synthesized by microorganisms, are often used as components for blending with PLA and other natural polymers [5, 6]. The miscibility of PLA and poly(3-hydroxybutyrate) (PHB) strongly depends on both components molecular weight, as expected [7, 8]. For example, using differential scanning calorimetry (DSC) the authors reported that bi-phasic mixtures were obtained when mixing PHB of M_w = 650 000 g/mol with PLA of M_w above 20 000 g/mol [8]. Below this value, the polymers were miscible in the whole range of com-

*Corresponding author, e-mail: bronnik@hq.macro.ru

positions. Bartczak *et al*. [9] used atactic PHB for making PLA/PHB blends. They found that PLA and PHB form non-miscible or partially miscible blends. They also showed that PHB is well dispersed in the PLA matrix at various ratios and the glass transition temperature of blend decreases with increasing PHB concentration. The impact strength of a thin film of the PLA/PHB blend (80/20 wt%) achieves 120 kJ/m^2 as compared with 50 kJ/m^2 for neat PLA [9].

Another frequently used polymer from polyhydroxyalkanoate family mixed with PLA is poly(hydroxybutyrate-co-hydroxyvalerate) (PHBV). Its properties are known to depend on hydroxyvalerate (HV) content [10]. At very low HV content, PHBV is similar to conventional petrochemical thermoplastics, such as polypropylene, in terms of melting temperature, crystallinity, and tensile strength [11–15]. Most of literature agrees on immiscibility of PLA and PHBV [16–19]. Boufarguine *et al*. [17] created multilayered films of PLA/PHBV (90/10 wt%) using multilayer co-extrusion. The formation of highly crystalline thin and long lamellas of PHBV improved gas barrier properties as compared to neat PLA. Foams with various cell densities were produced from PLA/PHBV and PLA/PHBV/clay blends using microcellular injection molding technique [20]. Bicomponent PLA/PHBV fibers were prepared using bicomponent melt spinning [21]. In vitro biocompatibility studies with human dermal fibroblasts demonstrated no toxicity of the fibers making them promising for medical applications.

Because of PLA/PHBV immiscibility, the morphology of most of the blends presents either 'inclusions' of the dispersed phase (usually more or less spherical droplets in the cases of conventional processing) or co-continuous phases. The properties of the blend will depend on the proportion in which in components are mixed, their individual properties, and also on the size distribution of the dispersed phase. In our previous work [18], we reported molten-state rheology of the PLA/PHBV blends and their morphology. The present work is devoted to the detailed analysis and understanding of PLA/PHBV blends characteristics in the solid state: morphology and mechanical properties, both evolving as a function of blend composition. Morphology is investigated using statistical analysis of scanning electron microscopy (SEM) images and analytical description of the histograms of the minor-phase particles' size. Mechanical properties (tensile strength, Young's modulus, elongation at break, and impact strength) are analyzed with the increment of 10 wt%. The elastic properties of blends are compared to the calculated ones according to different theoretical predictions. We also demonstrate that ductile properties of PLA/PHBV blend with PHBV in the minor phase disappear after one month after injection.

2. Experimental

2.1. Materials

Both polymers, PLA (3051D, injection molding grade) produced by NatureWorks Co. Ltd., USA, and PHBV (Enmat Y1000P) produced by Tian An Biological Materials Co., People's Republic of China, were provided by Natureplast, France. Their main characteristics, as given by provider, are collected in Table 1.

2.2. Blends preparation

PLA/PHBV blends were prepared by components melting in a Haake Rheomix 600 internal batch mixer (Thermo Fisher, Germany), the composition varied from 0/100 to 100/0 wt% with the increment of 10 wt%. The mixing temperature (165°C), rotor speed (60 rpm), and mixing time (6 min) were chosen according to minimization of PHBV thermal degradation [18]. Because of high viscosity of molten polymers which induced energy dissipation in the mixing chamber, the temperature exceeded the set value by ca. 10°C for all blends. The prepared blends were cooled to ambient temperature and cut into granules using an M 50/80 granulator (Hellweg, Germany).

2.3. Morphology characterization

The morphology of the blends was studied using a high-resolution scanning electron microscope SUPRA 40 FEG-SEM (Zeiss, Germany). The samples were fractured in liquid nitrogen and sputter-coated with gold-palladium. The obtained images

Table 1. Physical properties of PLA and PHBV as given by provider

Polymer	Glass transition temperature [°C]	Melting temperature [°C]	Melt flow index, g/10 min [190°C/2.16 kg]	Density [g/cm^3]
PLA	55–60	145–155	12–20	1.25
PHBV	5	165–175	15–30	1.25

were segmented and processed by digital analysis using UTHSCSA ImageTool 3.0 software (Health Science Center, the University of Texas, San Antonio, USA) resulting in histograms describing minor phase particle size distribution. The histograms were consequently described using the model of reversible aggregation [22, 23].

2.4. Mechanical properties characterization

Dumbbell-shape tensile bars were obtained from the blends according to ISO 527-2 1BA standard using a Haake Mini Jet II injection molding machine (Thermo Fisher, Germany) at 190°C. Impact bars were made according to ISO 179 standard by compression moulding using a hydraulic press (Carver, USA).

The tensile properties were measured two days after injection according to ISO 527-1BA standard using a tensile testing machine (Erichsen, Germany) at crosshead speed of 5 mm/min at room temperature. For a selected blend, PLA/PHBV = 90/10, the evolution of mechanical properties were followed in time, during one month. Charpy impact strength of the blends was measured using CEAST 9050 (Instron, USA).

2.5. Background of the model of reversible aggregation

For statistical analysis of the size distributions of dispersed-phase particles we used the model of the reversible aggregation [22, 23]. The model is based on principles of irreversible thermodynamics and describes microstructure evolution in liquids. According to the model, a stationary microstructure in a liquid permanently fluctuates creating a sequence of the equivalent microstructures, and after liquid freezing, only one of many possible microstructure configurations is realized. The microstructure elements, the aggregates, represent the dynamic units which are permanently composed and decomposed (a condition of reversibility) under thermal fluctuations with energy kT (k is the Boltzmann constant and T is the absolute temperature). It is supposed that the quasi-stationary equilibrium is quickly reached as a result of self-organization in the system. The model has successfully been applied to different objects and processes, including analysis of morphology of incompatible polymer blends [24–28].

In the model, statistical distribution $h(s)$ of the planar size s of the microstructural entities can be read as Equation (1) [22, 23]:

$$h(s) = as^2 \exp\left(-\frac{s\Delta u_0}{kT} \right) \tag{1}$$

where a is the normalizing parameter and Δu_0 is the aggregation energy. The latter parameter can be treated as a potential barrier to be overcome for the formation of a statistical ensemble. Its value should rather be compared to the energy of thermal fluctuations: $\Delta u_0/kT$.

In some cases, the aggregates form not a single but multiple statistical ensembles. For blended incompatible polymers they are the ensembles of dispersed and coalesced particles [24–28]. In this case, Equation (1) should be read as Equation (2):

$$h(s) = \sum_{i=1}^{N} a_1 s_i^2 \exp\left(-\frac{s_i \Delta u_{0i}}{kT} \right) \tag{2}$$

where N is the total number of statistical ensembles, while i accounts the number of a statistical ensemble.

As the size parameter s we chose the planar area of the minor phase particles in the SEM images. Equation (2) allows determination of the mean area $\langle s_i \rangle$ of the minor-phase particles belonging to the i-th statistical ensemble as the normalized mathematical expectation Ms_i as shown by Equation (3):

$$\langle s_i \rangle = Ms_i = \frac{\int_0^\infty s_i^2 \exp\left(-\frac{s_i \Delta u_{0i}}{kT} \right) ds_i}{\int_{0_{0i}}^\infty s_i^2 \exp\left(-\frac{s_i \Delta u_{0i}}{kT} \right) ds_i} = \frac{3kT}{\Delta u_{0i}} \tag{3}$$

Assuming that the shape of the entities related to the i-th statistical ensemble is circular, their mean diameter $\langle d_i \rangle$ can be determined using a simple geometrical consideration, see Equation (4):

$$\langle d_i \rangle = 2\sqrt{\frac{\langle s_i \rangle}{\pi}} \tag{4}$$

3. Results and discussion

3.1. Blend morphology

In Figure 1, the SEM micrographs of PLA/PHBV blends of various compositions are presented. All images show that blended polymers are immiscible and the particles of the minor phase are well distinguished.

Figure 2 presents the histograms resulting from the statistical analysis of the minor phase particles shown in Figure 1 and their analytical descriptions using Equation (1) or Equation (2). As follows from

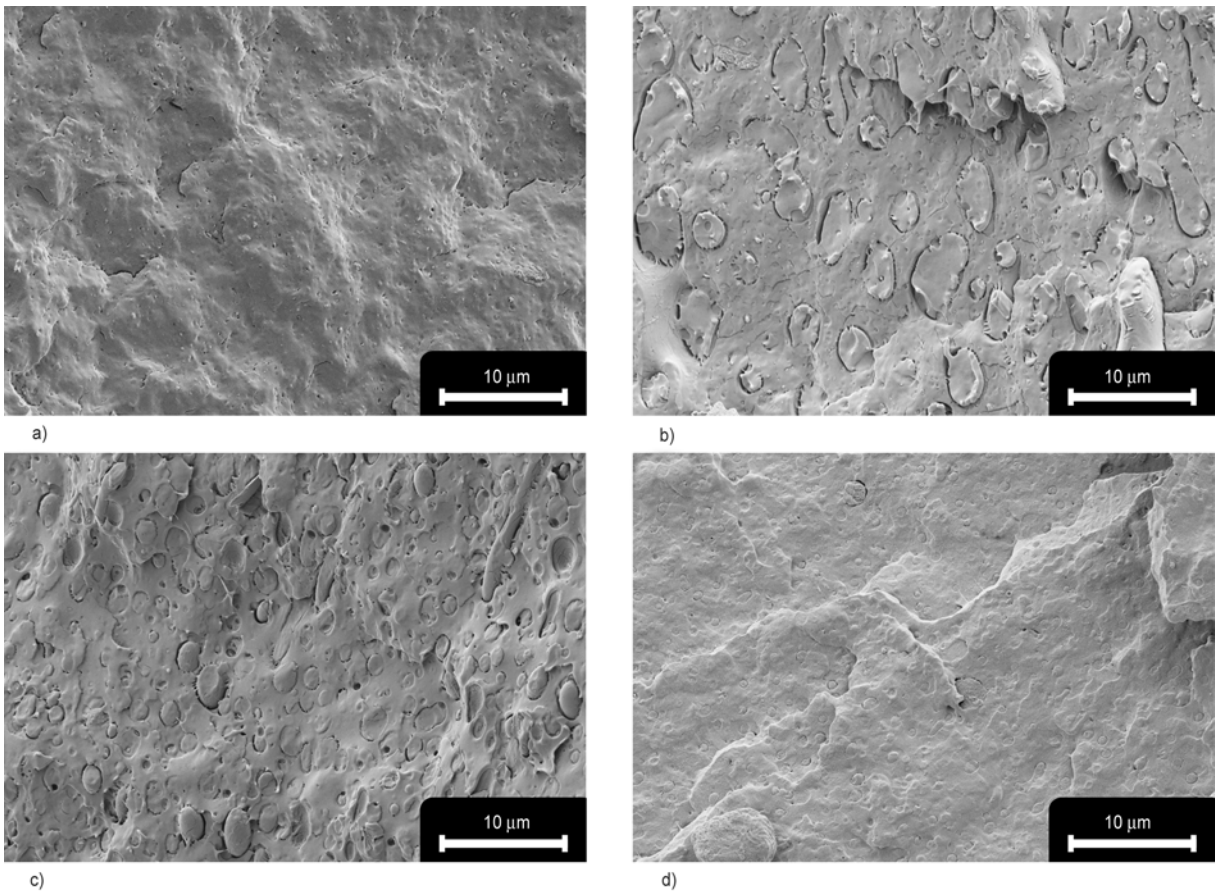

Figure 1. SEM images of the PLA/PHBV blends of the compositions: (a) 10/90, (b) 40/60, (c) 75/25, and (d) 90/10 wt%

Figure 2, the histograms corresponding to the blends with low PLA content (≤10 wt %, see, e.g., Figure 2a) can adequately be described using Equation (1). Similarly, the histograms corresponding to the blends with low PHBV content (≤10 wt%, see, e.g., Figure 2d), can also be successfully described using Equation (1). For the description of the histograms corresponding to the blends with the larger content of the minor component (PLA content >10 wt%, Figure 2b, and PHBV content >10 wt%, Figure 2c), the bimodal distribution (Equation (2), $N = 2$) rather than Equation (1) is suitable.

Mixing of molten immiscible polymers is known to be accompanied by two processes: i) break-up and dispersion of a minor phase droplets and ii) their coalescence [24–28]. The latter is especially pronounced when no compatibiliser is used. Taking this into consideration, the physical meaning of two statistical ensembles of the minor phase particles observed in Figures 2b and 2c and described with Equation (2) becomes clear: the first ensemble ($i = 1$) contains only the individual dispersed particles, while the second one ($i = 2$) contains exceptionally the coalesced particles.

The mean diameter of both dispersed and coalesced particles belonging to the minor phase was calculated using Equations (3) and (4). In Figure 3, this parameter is plotted as a function of blend composition. In most cases (except PLA/PHBV = 10/90), the mean diameter of dispersed PLA and PHBV particles varies from 0.7 to 1.2 µm; it very slightly increases with increasing minor phase concentration. The mean diameter of the coalesced particles increases more rapidly with increasing minor phase fraction. When the concentration of the minor component exceeds 40 wt%, the mean diameter of the coalesced particles significantly increases: the blend is formed of co-continuous phases (infinite diameter) with some inclusions of individual coalesced droplets. The result obtained is similar to that for the PLA/polystyrene blends [29]. According to the authors, large particles of the minor phase can be explained by weak interactions between the components and their incompability.

3.2. Mechanical properties

Tensile and impact properties of the blends of various compositions are presented in Table 2. It shows

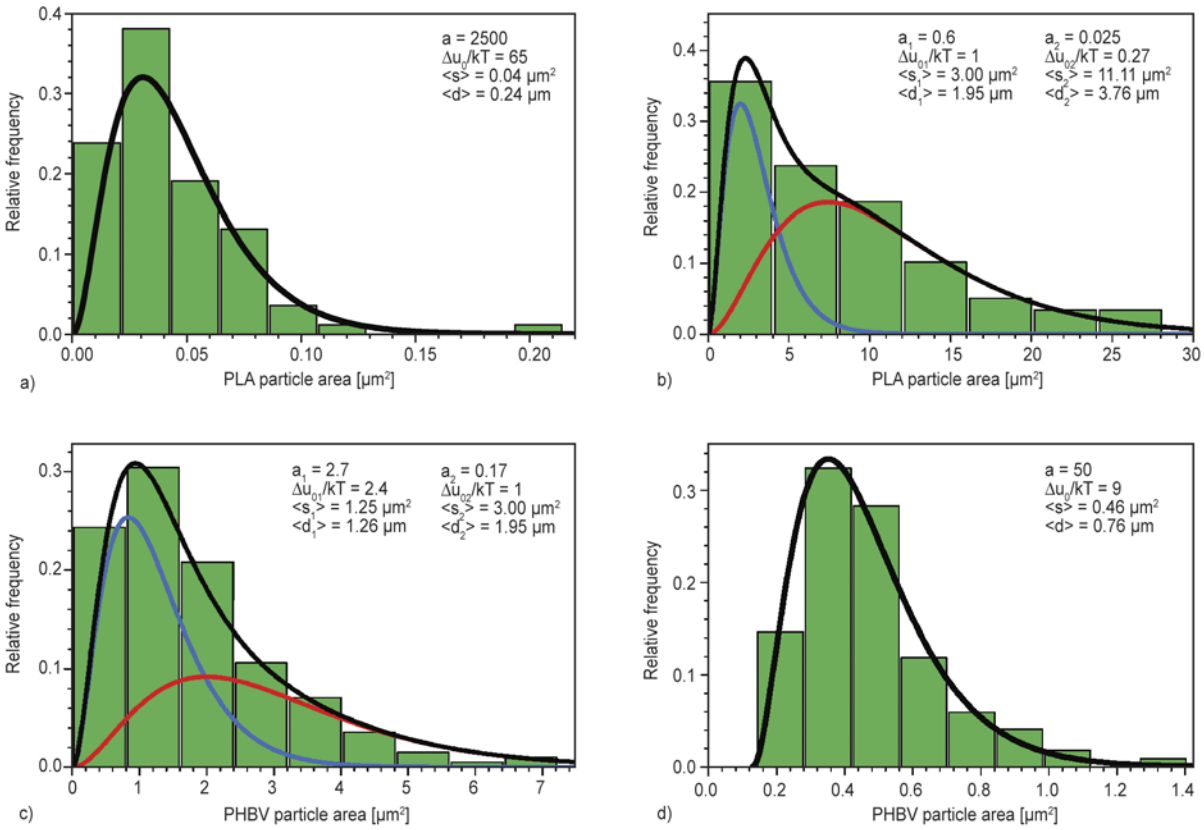

Figure 2. Statistical area distributions of the minor-phase particles in the PLA/PHBV blends of the compositions: (a) 10/90, (b) 40/60, (c) 75/25, and (d) 90/10 wt %. Their analytical description (black lines) using Equation (1) or Equation (2) ($i = 2$) with the equation parameters presented in boxes is provided along with the mean particle area $\langle s \rangle$ and mean particle diameter $\langle d \rangle$ calculated with Equations (3) and (4), respectively. In sub-figures (b) and (c), individual statistical ensembles related to dispersed and coalesced particles are presented as blue and red lines, respectively.

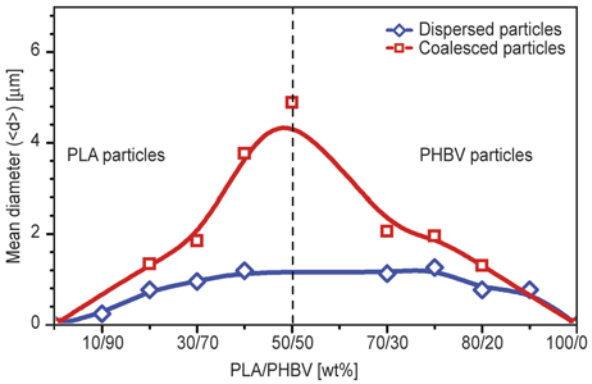

Figure 3. Mean diameter of both dispersed and coalesced minor-phase particles of the PLA/PHBV blends as a function of the blend composition

that both neat components (PLA and PHBV) and the majority of the blends are relatively brittle: their elongation at break varies from 3 to 6% and impact strength varies from 1 to 2.5 kJ/m^2. Only two PLA/PHBV compositions, with low content of PHBV, demonstrate high deformability: 50.7% (80/20 wt%) and 204% (90/10 wt%). This phenomenon is similar to that reported for PLA blended with some other PHA-based polymers with the latter being in the minor phase: for example, with poly(3-hydroxybutyrate-co-3-hydroxyhexanoate), so-called 'Nodax' copolymers, the elongation was 100–200% [30, 31]. It is known that both PLA and PHBV are subjected to aging: for example, PLA loses it ductile properties in 4–5 days at ambient temperature [32] and the mechanical properties of PHBV are stabilized after 20–30 days [33]. We followed the evolution of the elongation at break during one month for PLA/PHBV composition 90/10 wt%. The decrease of the elongation after 4, 14 and 24 days is shown in Figure 4: in about one month, the mixture stored at room temperature loses its ductile properties dramatically. A slight increase of Young's modulus, impact strength and tensile strength of the PLA/PHBV blends in time is within the experimental errors and thus is not shown.

In Figure 5, Young's modulus E and tensile strength S of the PLA/PHBV blends are presented as a function of blend composition. The experimental results are shown with points and theoretical predictions

Table 2. Mechanical properties of PLA/ PHBV compositions

PLA/PHBV composition	Stress at break [MPa]	Elongation at break [%]	Young's modulus [MPa]	Impact strength [kJ/m^2]
0/100	38.8±0.4	3.9±0.6	2310±80	1.20±0.20
10/90	39.8±0.2	3.8±0.5	2320±30	–
20/80	42.7±1.2	3.4±0.2	2380±50	0.95±0.30
30/70	46.1±0.8	3.7±0.3	2420±50	–
40/60	47.5±0.6	6.6±1.1	2410±20	–
50/50	53.6±0.4	4.1±0.7	2610±60	1.34±0.18
60/40	56.4±1.0	5.5±0.9	2610±60	–
70/30	57.0±0.8	9.8±2.2	2580±20	–
80/20	56.5±0.8	50.7±33.4	2490±70	2.63±0.50
90/10	58.0±0.3	204.3±20.5	2360±40	2.55±0.55
100/0	67.5±0.5	4.8±0.4	2630±30	2.00±0.90

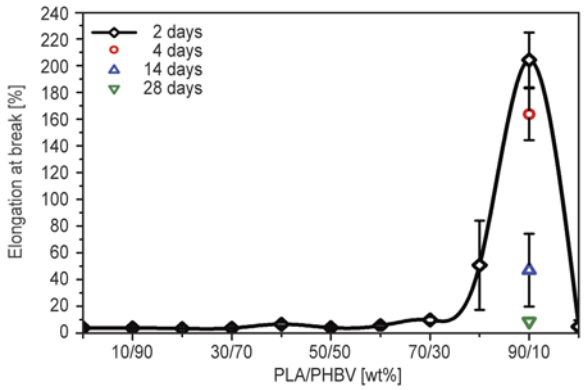

Figure 4. Elongation at break of the PLA/PHBV blends as a function of the blend composition as measured two days after injection. The results of testing the 90/10 wt% composition after 4, 14 and 28 days are also presented

for E_{blend} and S_{blend}, calculated according to Voigt (Equation (5)) and Reuss (Equation (6)) models, are given with solid and dashed lines, respectively:

$$E_{blend} = \sum_i f_i E_i, \quad S_{blend} = \sum_i f_i S_i \tag{5}$$

$$\frac{1}{E_{blend}} = \sum_i f_i \frac{1}{E_i}, \quad \frac{1}{S_{blend}} = \sum_i f_i \frac{1}{S_i} \tag{6}$$

where f_i is mass fraction of each component in the blend and E_i or S_i are neat component Young's modulus and tensile strength values, respectively.

It is clear that tensile strength increases with increasing concentration of PLA phase (Figure 5a) and follows, within the errors, the trends predicted by both models. Both give rather similar S_{blend} values and none of them can be privileged in terms of better matching the experimental data.

Young's modulus of the blends is in-between the values of neat components, from 2300 to 2600 MPa (Figure 5b), and increases, in overall, with increasing of PLA fraction in the blend, except for some blends with low PHBV weight fraction (80/20 and 90/10 wt%). Because of a very small difference between the moduli of neat PLA and PHBV, both models predict very similar E_{blend} values. The modulus of the blends with the components in equal proportions, forming co-continuous phases, is slightly above the additive prediction. Because the maxi-

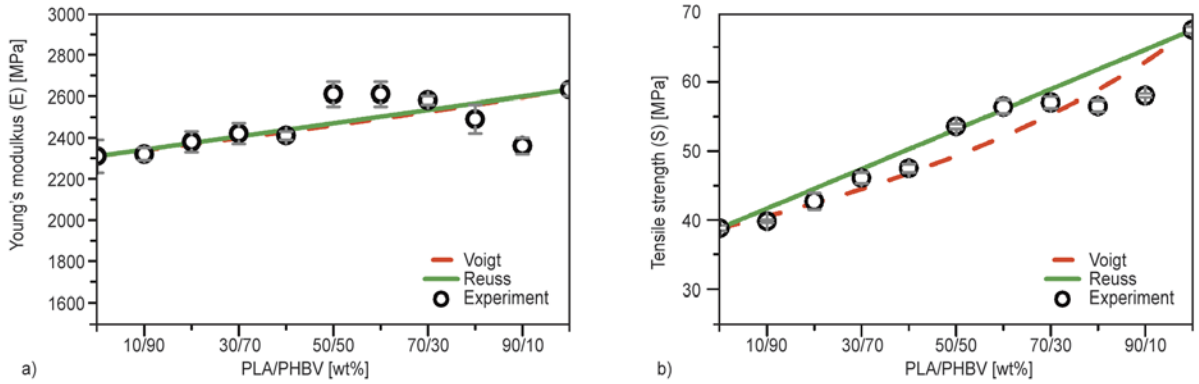

Figure 5. (a) Young's modulus and (b) tensile strength of the PLA/PHBV blends as a function of the blend composition. A comparison with the theoretical predictions (Voight and Reuss models) is also presented with solid green and dashed red lines, respectively.

mum deviation of experimental values from the predictions given by models is within 10%, we will not speculate about the reason of this slight increase of blend Young's modulus. Blends with low PHBV fraction, such as PLA/PHBV = 80/20 and 90/10, show moduli lower than the additive values, with the maximal deviation from the theoretical prediction being within 15%. One of the reasons of this negative deviation could be that after two days the mixture is still ductile and thus has weaker Young's modulus. As mentioned above, Young's modulus of the blend PLA/PHBV = 90/10 wt% slightly increases in time, practically reaching the additive values.

4. Conclusions

The morphological and mechanical properties of fully bio-based blends, PLA/PHBV, prepared by melt mixing, were investigated in details as a function of composition with the increment of 10 wt% in the full range of compositions. We statistically analyzed blend morphology using their SEM images and applying principles of irreversible thermodynamics. Two statistical ensembles of the minor-phase droplets involving dispersed and coalesced particles were found. When a content of the minor phase was low (≤10 wt%), only dispersed particles of the minor phase were found, whereas at the higher minor-phase concentration, both dispersed and coalesced minor-phase particles were observed. For 50/50 wt% composition, no dispersed particles were found. The mean diameters of both dispersed and coalesced minor-phase particles were calculated and plotted against blend composition. The mean diameter of the dispersed minor-phase particles was shown to be small (about 1 μm) and practically not varying with composition. The mean diameter of the coalesced particles was found to increase more considerably and achieves ca. 5 μm for the 50/50 wt% composition exhibiting co-continuous morphology.

Young's modulus and tensile strength of the PLA/PHBV blends were investigated as a function of blend composition. Both characteristics were found to increase with increasing proportion of the PLA component. The results obtained correspond, within the experimental errors, to the theoretical predictions according to Reuss and Voigt models.

Blends with low content of PHBV in the minor phase showed very high elongation at break, about 200%, for samples studied two days after injection. We found that this property decreases dramatically in one month (from 200 to few %) because of the aging process in both components, though tensile strength, Young's modulus, and impact strength did not change considerably in time.

Acknowledgements

The present work is performed in the frame of the Industrial Chair in Bioplastics, organized by CEMEF/MINES ParisTech and supported by Arkema, L'Oreal, Nestlé, PSA Peugeot Citroën, and Schneider Electric. Authors are grateful to Suzanne Jacomet (CEMEF/MINES ParisTech) for the help is SEM experiments.

References

[1] Garlotta D.: A literature review of poly(lactic acid). Journal of Polymers and the Environment, **9**, 63–84 (2001).
DOI: 10.1023/A:1020200822435

[2] Conn R. E., Kolstad J. J., Borzelleca J. F., Dixler D. S., Filer L. J., Ladu B. N., Pariza M. W.: Safety assessment of polylactide (PLA) for use as a food-contact polymer. Food and Chemical Toxicology, **33**, 273–356 (1995).
DOI: 10.1016/0278-6915(94)00145-E

[3] Lasprilla A. J. R., Martinez G. A. R., Lunelli B. H., Jardini A. L., Filho R. M.: Poly-lactic acid synthesis for application in biomedical devices – A review. Biotechnology Advances, **30**, 321–328 (2012).
DOI: 10.1016/j.biotechadv.2011.06.019

[4] Rasal R. M., Janorkar A. V., Hirt D. E.: Poly(lactic acid) modifications. Progress in Polymer Science, **35**, 338–394 (2010).
DOI: 10.1016/j.progpolymsci.2009.12.003

[5] Holmes P. A.: Biologically produced (R)-3-hydroxyalkanoate polymers and copolymers. Elsevier, London (1998).

[6] El-Hadi A., Schnabel R., Straube E., Müller G., Riemschneider M.: Effect of melt processing on crystallization behavior and rheology of poly(3-hydroxybutyrate) (PHB) and its blends. Macromolecular Materials and Engineering, **287**, 363–372 (2002).
DOI: 10.1002/1439-2054(20020501)287:5<363::AID-MAME363>3.0.CO;2-D

[7] Blümm E., Owen A. J.: Miscibility, crystallization and melting of poly(3-hydroxybutyrate)/ poly(L-lactide) blends. Polymer, **36**, 4077–4081 (1995).
DOI: 10.1016/0032-3861(95)90987-D

[8] Koyama N., Doi Y.: Miscibility of binary blends of poly[(*R*)-3-hydroxybutyric acid] and poly[(*S*)-lactic acid]. Polymer, **38**, 1589–1593 (1997).
DOI: 10.1016/S0032-3861(96)00685-4

[9] Bartczak Z., Galeski A., Kowalczuk M., Sobota M., Malinowski R.: Tough blends of poly(lactide) and amorphous poly([R,S]-3-hydroxy butyrate) – morphology and properties. European Polymer Journal, **49**, 3630–3641 (2013).
DOI: 10.1016/j.eurpolymj.2013.07.033

[10] Laycock B., Halley P., Pratt S., Werker A., Lant P.: The chemomechanical properties of microbial polyhydroxyalkanoates. Progress in Polymer Science, **38**, 536–583 (2013).
DOI: 10.1016/j.progpolymsci.2012.06.003

[11] Ferreira B. M. P., Zavaglia C. A. C., Duek E. A. R.: Films of PLLA/PHBV: Thermal, morphological, and mechanical characterization. Journal of Applied Polymer Science, **86**, 2898–2906 (2002).
DOI: 10.1002/app.11334

[12] Ramkumar D. H. S., Bhattacharya M.: Steady shear and dynamic properties of biodegradable polyesters. Polymer Engineering and Science, **38**, 1426–1435 (1998).
DOI: 10.1002/pen.10313

[13] Wang S., Ma P., Wang R., Wang S., Zhang Y.: Mechanical, thermal and degradation properties of poly(*d,l*-lactide)/poly(hydroxybutyrate-*co*-hydroxyvalerate)/poly (ethylene glycol) blend. Polymer Degradation and Stability, **93**, 1364–1369 (2008).
DOI: 10.1016/j.polymdegradstab.2008.03.026

[14] Marcilla A., Garcia-Quesada J. C., Lopez M., Gil E.: Study of the behavior of blends of a poly(hydroxybutyrate-valerate) copolymer, polypropylene, and SEBS. Journal of Applied Polymer Science, **113**, 3187–3195 (2009).
DOI: 10.1002/app.29939

[15] Sudesh K., Abe H., Doi Y.: Synthesis, structure and properties of polyhydroxyalkanoates: Biological polyesters. Progress in Polymer Science, **25**, 1503–1555 (2000).
DOI: 10.1016/S0079-6700(00)00035-6

[16] Modi S., Koelling K., Vodovotz Y.: Miscibility of poly (3-hydroxybutyrate-*co*-3-hydroxyvalerate) with high molecular weight poly(lactic acid) blends determined by thermal analysis. Journal of Applied Polymer Science, **124**, 3074–3081 (2012).
DOI: 10.1002/app.35343

[17] Boufarguine M., Guinault A., Miquelard-Garnier G., Sollogoub C.: PLA/PHBV films with improved mechanical and gas barrier properties. Macromolecular Materials and Engineering, **298**, 1065–1073 (2013)
DOI: 10.1002/mame.201200285

[18] Gerard T., Budtova T.: Morphology and molten-state rheology of polylactide and polyhydroxyalkanoate blends. European Polymer Journal, **48**, 1110–1117 (2012).
DOI: 10.1016/j.eurpolymj.2012.03.015

[19] Nanda M. R., Misra M., Mohanty A. K.: The effects of process engineering on the performance of PLA and PHBV blends. Macromolecular Materials and Engineering, **296**, 719–728 (2011).
DOI: 10.1002/mame.201000417

[20] Zhao H., Cui Z., Wang X., Turng L-S., Peng X.: Processing and characterization of solid and microcellular poly(lactic acid)/polyhydroxybutyrate-valerate (PLA/PHBV) blends and PLA/PHBV/clay nanocomposites. Composites Part B: Engineering, **51**, 79–91 (2013).
DOI: 10.1016/j.compositesb.2013.02.034

[21] Hufenus R., Reifler F. A., Maniura-Weber K., Spierings A., Zinn M.: Biodegradable bicomponent fibers from renewable sources: Melt-spinning of poly(lactic acid) and poly[(3-hydroxybutyrate)-*co*-(3-hydroxyvalerate)]. Macromolecular Materials and Engineering, **297**, 75–84 (2012).
DOI: 10.1002/mame.201100063

[22] Kilian H. G., Zink B., Metzler R.: Aggregate model of liquids. Journal of Chemical Physics, **107**, 8697–8705 (1997).
DOI: 10.1063/1.475022

[23] Kilian H-G., Bronnikov S., Sukhanova T.: Transformations of the micro-domain structure of polyimide films during thermally induced chemical conversion: Characterization via thermodynamics of irreversible processes. Journal of Physical Chemistry: B, **107**, 13575–13582 (2003).
DOI: 10.1021/jp035074m

[24] Zuev V. V., Bronnikov S.: Statistical analysis of the phase separation of LDPE/PA-6 blends compatibilized with SEBS-*g*-MA and/or organoclays. Journal of Polymer Research, **17**, 731–735 (2010).
DOI: 10.1007/s10965-009-9363-y

[25] Zuev V. V., Bronnikov S.: Statistical analysis of morphology of low density polyethylene/polyamide 6 blends with addition of organoclay and maleic anhydride-grafted polystyrene-*b*-poly(ethylene-*co*-butene-1)-*b*-polystyrene copolymer as compatibilizers. Journal of Macromolecular Science Part B: Physics, **51**, 1558–1565 (2012).
DOI: 10.1080/00222348.2012.656008

[26] Zuev V. V., Steinhoff B., Bronnikov S., Kothe H., Alig I.: Flow-induced size distribution and anisotropy of the minor phase droplets in a polypropylene/poly (ethylene-octene) copolymer blend: Interplay between breakup and coalescence. Polymer, **53**, 755–760 (2012).
DOI: 10.1016/j.polymer.2011.12.046

[27] Chen X-H., Yu P., Kostromin S., Bronnikov S.: Minor-phase particles evolution in a polyethylene/ethylene–propylene copolymer (80/20) blend across mixing: Breakup and coalescence. Journal of Applied Polymer Science, **130**, 3421–3431 (2013).
DOI: 10.1002/app.39373

[28] Tang W., Wang H., Tang J., Yuan H.: Polyoxymethylene/thermoplastic polyurethane blends compatibilized with multifunctional chain extender. Journal of Applied Polymer Science, **127**, 3033–3039 (2013).
DOI: 10.1002/app.37538

[29] Imre B., Renner K., Pukánszky B.: Interactions, structure and properties in poly(lactic acid)/thermoplastic polymer blends. Express Polymer Letters, **8**, 2–14 (2014).
DOI: 10.3144/expresspolymlett.2014.2

[30] Noda I., Satkowski M. M., Dowrey A. E., Marcott C.: Polymer alloys of Nodax copolymers and poly(lactic acid). Macromolecular Bioscience, **4**, 269–275 (2004).
DOI: 10.1002/mabi.200300093

[31] Zhao Q., Wang S., Kong M., Geng W., Li R. K. Y., Song S., Kong D.: Phase morphology, physical properties, and biodegradation behavior of novel PLA/PHB-HHx blends. Journal of Biomedical Materials Research Part B: Applied Biomaterials, **100**, 23–31 (2012).
DOI: 10.1002/jbm.b.31915

[32] Pan P., Zhu B., Inoue Y.: Enthalpy relaxation and embrittlement of poly(L-lactide) during physical aging. Macromolecules, **40**, 9664–9671 (2007).
DOI: 10.1021/ma071737c

[33] Srubar III W. V., Wright Z. C., Tsui A., Michel A. T., Billington S. L., Frank C. W.: Characterizing the effects of ambient aging on the mechanical and physical properties of two commercially available bacterial thermoplastics. Polymer Degradation and Stability, **97**, 1922–1929 (2012).
DOI: 10.1016/j.polymdegradstab.2012.04.011